Jet energy scale and resolution in the CMS experiment in pp collisions at 8 TeV

2017 JINST 12 P02014

(http://iopscience.iop.org/1748-0221/12/02/P02014)

Jinst

Published by IOP Publishing for Sissa Medialab

Received: *July 13, 2016*
Revised: *January 22, 2017*
Accepted: *January 29, 2017*
Published: *February 22, 2017*

Jet energy scale and resolution in the CMS experiment in pp collisions at 8 TeV

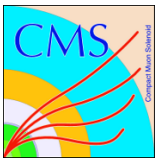

The CMS collaboration

E-mail: cms-publication-committee-chair@cern.ch

Abstract: Improved jet energy scale corrections, based on a data sample corresponding to an integrated luminosity of 19.7 fb^{-1} collected by the CMS experiment in proton-proton collisions at a center-of-mass energy of 8 TeV, are presented. The corrections as a function of pseudorapidity η and transverse momentum p_{T} are extracted from data and simulated events combining several channels and methods. They account successively for the effects of pileup, uniformity of the detector response, and residual data-simulation jet energy scale differences. Further corrections, depending on the jet flavor and distance parameter (jet size) R, are also presented. The jet energy resolution is measured in data and simulated events and is studied as a function of pileup, jet size, and jet flavor. Typical jet energy resolutions at the central rapidities are 15–20% at 30 GeV, about 10% at 100 GeV, and 5% at 1 TeV. The studies exploit events with dijet topology, as well as photon+jet, Z+jet and multijet events. Several new techniques are used to account for the various sources of jet energy scale corrections, and a full set of uncertainties, and their correlations, are provided.The final uncertainties on the jet energy scale are below 3% across the phase space considered by most analyses ($p_{\text{T}} > 30$ GeV and $|\eta| < 5.0$). In the barrel region ($|\eta| < 1.3$) an uncertainty below 1% for $p_{\text{T}} > 30$ GeV is reached, when excluding the jet flavor uncertainties, which are provided separately for different jet flavors. A new benchmark for jet energy scale determination at hadron colliders is achieved with 0.32% uncertainty for jets with p_{T} of the order of 165–330 GeV, and $|\eta| < 0.8$.

Keywords: Large detector-systems performance; Performance of High Energy Physics Detectors

ArXiv ePrint: 1607.03663

doi:10.1088/1748-0221/12/02/P02014

Contents

2017 JINST 12 P02014

1 Introduction

The state-of-the-art techniques used in the CMS experiment at the CERN LHC for jet energy scale (JES) and jet energy resolution (JER) calibration are presented, based on a data sample corresponding to an integrated luminosity of 19.7 fb^{-1} collected in proton-proton collisions at a center-of-mass energy of 8 TeV. Jets are the experimental signatures of energetic quarks and gluons produced in high-energy processes. Like all experimentally-reconstructed objects, jets need to be calibrated in order to have the correct energy scale: this is the aim of the jet energy corrections (JEC). The detailed understanding of both the energy scale and the transverse momentum resolution of the jets is of crucial importance for many physics analyses, and a leading component of their associated systematic uncertainties. Improvements made in understanding the JES in the recent years have resulted in very precise measurements of, e.g., the inclusive jet cross section [1–5], and the top quark mass [6–9]. The JES uncertainties presented here propagate to uncertainties of 2–4% in the jet cross sections in the central region, and of ±0.35 GeV in the top-quark mass determination.

The results in this paper are reported for jets reconstructed with the particle-flow (PF) method [10, 11] using the anti-k_{T} algorithm [12] with distance parameter $R = 0.5$. The jet energy corrections are calculated using a detailed Monte Carlo (MC) simulation of the detector, and are then adjusted for data using a combination of several channels and data-driven methods. The JEC successively correct for the offset energy coming from multiple proton-proton collisions in the same and adjacent beam crossings (pileup), the detector response to hadrons, and residual differences between data and MC simulation as a function of the jet pseudorapidity η and transverse momentum p_{T}. The jet p_{T} is corrected up to the so-called particle-level jets clustered from stable (decay length $c\tau > 1$ cm) and visible (excluding neutrinos) final-state particles.

Corrections depending on jet flavor (for quarks: u and d, s, c and b; and for gluons) and jet distance parameter R are also presented. The uncertainties affecting the JES determination are discussed, and a full set of uncertainties and their correlations are provided. Figure 1 shows the jet response at the various stages of JEC for jets (produced in quantum chromodynamics (QCD) hard-scattering processes) measured at central pseudorapidities ($|\eta| < 1.3$): for each bin in $p_{\mathrm{T,\,ptcl}}$, the jet response is defined as the average value of the ratio of measured jet p_{T} to particle-level jet $p_{\mathrm{T,\,ptcl}}$. The response is shown before any correction, after correcting for the effect of pileup, and after all stages of corrections, that will be detailed in the following. Distributions corresponding

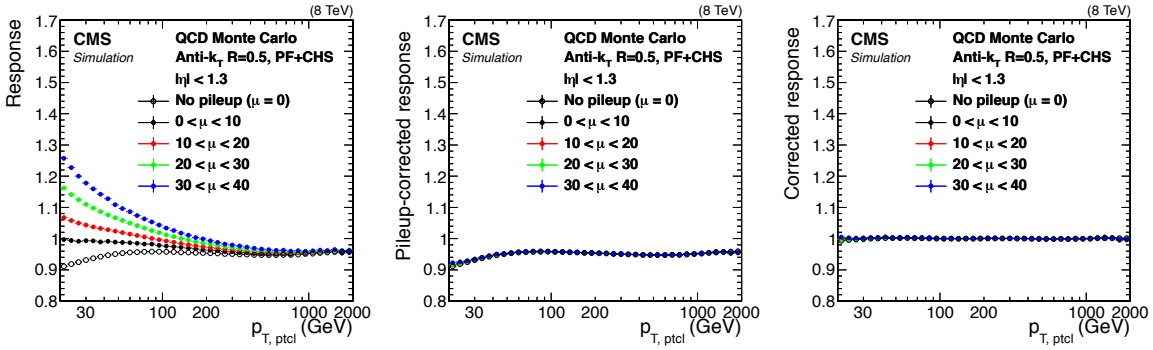

Figure 1. Average value of the ratio of measured jet p_T to particle-level jet $p_{T,\,ptcl}$ in QCD MC simulation, in bins of $p_{T,\,ptcl}$, at various stages of JEC: before any corrections (left), after pileup offset corrections (middle), after all JEC (right). Here μ is the average number of pileup interactions per bunch crossing.

to different average numbers of pileup interactions per bunch crossing (μ) are shown separately, to display the dependence of the response on the pileup.

The jet p_T resolution, measured after applying JEC, is extracted in data and simulated events. It is studied as a function of pileup, jet size R, and jet flavor. The effect of the presence of neutrinos in the jets is also studied. The typical JER is 15–20% at 30 GeV, about 10% at 100 GeV, and 5% at 1 TeV at central rapidities.

The general principles behind the methods of extraction of the JES, and the reasons why the JES obtained with the PF algorithm is different from unity, are discussed. The results and methods are compared to previous CMS studies done for 7 TeV proton-proton collisions [13]. Several new techniques are introduced in this paper to account for p_T-dependent pileup offset, out-of-time (OOT) pileup, initial- and final-state radiation (ISR+FSR), and b-quark jet (b-jet) flavor response. We also add the information from multijet balancing [14] and introduce a new technique that uses it as part of a global p_T-dependent fit which constrains the uncertainties by using their correlations between channels and methods.

Pileup collisions result in unwanted calorimetric energy depositions and extra tracks. The charged-hadron subtraction (CHS, section 4.2) reduces these effects by removing tracks identified as originating from pileup vertices. The results in this paper are reported for jets reconstructed with and without CHS.

The JEC are extracted for jets with $p_T > 10$ GeV and $|\eta| < 5.2$, with uncertainties less than or about 3% over the whole phase space. The minimum JES uncertainty of 0.32% for jets with $165 < p_T < 330$ GeV and $|\eta| < 0.8$, when excluding sample-dependent uncertainties due to jet-flavor response and time-dependent detector response variations, surpasses the precision of previous JES measurements at the Tevatron [15, 16] and the LHC [13, 17].

Outline of the paper and overview of the corrections

The CMS detector and reconstruction algorithms are briefly described in section 2. The data and MC samples used throughout this document, together with the different selection criteria, are detailed in section 3.

2017 JINST 12 P02014

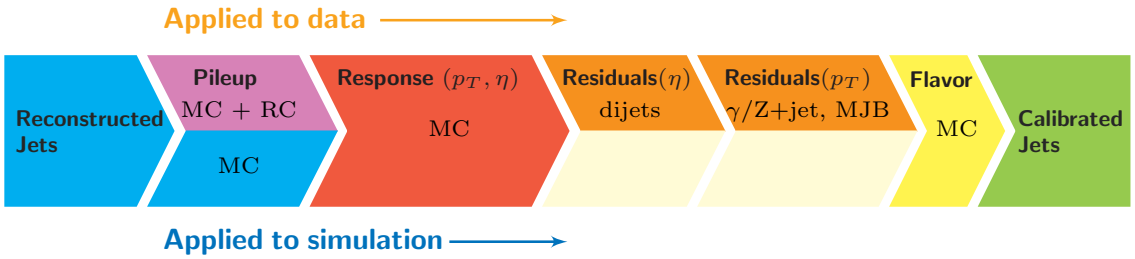

Figure 2. Consecutive stages of JEC, for data and MC simulation. All corrections marked with MC are derived from simulation studies, RC stands for random cone, and MJB refers to the analysis of multijet events.

The pileup offset corrections, discussed in section 4, are determined from the simulation of a sample of dijet events processed with and without pileup overlay. They are parameterized as a function of offset energy density ρ, jet area A, jet pseudorapidity η, and jet transverse momentum p_T. Corrections for residual differences between data and detector simulation as a function of η are determined using the random cone (RC, section 4.3) method in zero-bias events (section 3.2). The pileup offset corrections are determined both before and after CHS, which removes tracks identified as originating from pileup vertices.

The simulated jet response corrections are determined with a CMS detector simulation based on GEANT4 [18] combined with the PYTHIA 6.4 [19] tune Z2* [20], as discussed in section 5. The corrections are determined for various jet sizes. The default corrections are provided for the QCD dijet flavor mixture as a function of p_T and η. Uncertainties arising from the modeling of jet fragmentation are evaluated with HERWIG++ 2.3 [21] tune EE3C [22], and uncertainties from the detector simulation are evaluated with the CMS fast simulation [23].

The residual corrections for data are discussed in section 6. The η-dependent corrections are determined with dijet events, relative to a jet of similar p_T in the barrel reference region $|\eta| < 1.3$. These corrections include a p_T dependence of the JES relative to the JES of the barrel jet for $p_T > 62$ GeV and up to about 1 TeV, the limit of available dijet data. The absolute scale, together with its p_T dependence within $|\eta| < 1.3$ for $30 < p_T < 800$ GeV, is measured combining photon+jet, Z($\rightarrow \mu\mu$)+jet and Z($\rightarrow$ ee)+jet events. The p_T dependence at $p_T > 800$ GeV is constrained with multijet events. Detailed studies are performed to correct for biases in the data-based methods due to differences with respect to the MC simulation in ISR+FSR as well as in jet p_T resolution.

The optional jet-flavor corrections derived from MC simulation are discussed in section 7 together with the JEC flavor uncertainty estimates based on comparing PYTHIA 6.4 and HERWIG++ 2.3 predictions. These uncertainties are applicable to data vs. simulation comparisons regardless of whether or not the jet-flavor corrections are applied. The flavor corrections and their uncertainties for b-quark jets are checked in data with Z+b events. The consecutive steps of the JEC are illustrated in figure 2.

The jet p_T resolutions are determined with both dijet and photon+jet events, as discussed in section 8. The reference resolutions obtained from simulation are parameterized as a function of particle-level jet $p_{T,\,\mathrm{ptcl}}$ (defined in section 2) and average number μ of pileup interactions in bins of jet η. Corrections for differences between data and MC simulation are applied as η-binned scale factors.

2017 JINST 12 P02014

The JES uncertainties, discussed in section 9, are provided in the form of a limited set of sources that allow a detailed statistical analysis of uncertainty correlations. The final uncertainties are below 1% across much of the phase space covered by these corrections at $p_T > 10\,\text{GeV}$ and $|\eta| < 5.2$. This sets a new benchmark for jet energy scale at hadron colliders.

In section 10 we describe additional studies made by investigating the particle composition of reconstructed PF jets. These support the overall conclusions drawn from the determination of residual jet energy corrections to be applied on data.

2 The CMS detector and event reconstruction

The central feature of the CMS apparatus is a 3.8 T superconducting solenoid of 6 m internal diameter. Within the field volume are the silicon tracker, the crystal electromagnetic calorimeter (ECAL), and the brass and scintillator hadron calorimeter (HCAL). The muon system is installed outside the solenoid and embedded in the steel flux-return yoke. CMS uses a right-handed coordinate system, with the origin at the nominal interaction point, the z axis pointing along the direction of the counterclockwise beam, the y axis pointing up (perpendicular to the plane of the LHC ring), and the x axis chosen to make a right-handed coordinate system. The polar angle θ is measured from the positive z axis, and the azimuthal angle ϕ is measured in the x-y plane in radians.

The CMS tracker consists of 1 440 silicon pixel and 15 148 silicon strip detector modules, with full azimuthal coverage within $|\eta| < 2.5$. The ECAL consists of 75 848 lead tungstate crystals, which provide coverage in pseudorapidity $|\eta| < 1.479$ in the central barrel region and $1.479 < |\eta| < 3.000$ in the two forward endcap regions. The HCAL is a sampling calorimeter using alternating layers of brass or steel as absorber and plastic scintillator as active material, it provides a coverage of $|\eta| < 1.3$ in the central region and $1.3 < |\eta| < 3.0$ in the endcap regions. In the forward region ($3.0 < |\eta| < 5.0$), a different calorimeter technology is employed in the hadron forward (HF) detector, which uses the Cherenkov light signals collected by short and long quartz readout fibers to aid the separation of electromagnetic (EM) and hadronic signals. The muon system includes barrel drift tubes covering the pseudorapidity range $|\eta| < 1.2$, endcap cathode strip chambers ($0.9 < |\eta| < 2.5$), and resistive-plate chambers ($|\eta| < 1.6$). A detailed description of the CMS detector can be found in ref. [24].

Events in CMS are reconstructed using the PF technique [10, 11], which reconstructs and identifies single particles with an optimized combination of all subdetector information. To suppress noise in the calorimeters, only cells with energies above a given threshold are considered, this procedure is referred to as "zero suppression". The energy of photons is obtained directly from the ECAL measurement, corrected for zero-suppression effects. The energy of electrons is determined from a combination of the track momentum at the main interaction vertex, the corresponding ECAL cluster energy, and the energy sum of all bremsstrahlung photons associated with the track. The energy of muons is obtained from the corresponding track momentum. The energy of charged hadrons is determined from a combination of the track momentum and the corresponding ECAL and HCAL energies, corrected for zero-suppression effects, and calibrated for the nonlinear response of the calorimeters. Finally, the energy of neutral hadrons is obtained from the corresponding calibrated ECAL and HCAL energies. In the forward region, energy deposits collected by the HF are considered as electromagnetic or hadronic, depending on the respective energy collected by long and short fibers. The particles reconstructed with the PF algorithm are jointly referred to as PF candidates.

2017 JINST 12 P02014

Jets are reconstructed by clustering the PF candidates, and the missing transverse momentum $\vec{p}_{\mathrm{T}}^{\,\mathrm{miss}}$ is the negative vectorial sum of the transverse momenta of all PF candidates reconstructed in an event.

Interaction vertices are reconstructed using track information only, and the primary interaction vertex is defined as the vertex with the highest sum of the squared transverse momenta of the tracks associated with it.

The first level (L1) of the CMS trigger system, composed of custom hardware processors, uses information from the calorimeters and muon detectors to select the most interesting events in a fixed time interval of less than 4 μs. The high-level trigger (HLT) processor farm further decreases the event rate from around 100 kHz to less than 1 kHz before data storage.

2.1 Jet reconstruction

Jets considered in this paper are reconstructed with the anti-k_{T} clustering algorithm [12]. The nominal results are obtained for a jet distance parameter, $R = 0.5$, which was used in most CMS analyses of 7 and 8 TeV data. Both the JES and JER are also studied for different values of the R parameter, on simulated events.

The **simulated particle-level jets** are built by applying the clustering procedure to all stable (lifetime $c\tau > 1$ cm) particles excluding neutrinos. The lifetime of heavy hadrons (containing c and b quarks) is shorter than $c\tau = 1$ cm, so their decay products are the particles considered for jet clustering. The exclusion of neutrinos is a convention adopted by CMS, but it is not universally adopted by all experiments in high-energy physics. Indeed, neutrinos are often included at the particle level, but the response is measured from samples with negligible neutrino content, leading to practically no difference for inclusive JEC. The CMS convention allows us to define response in a way that is experimentally accessible and significantly reduces response differences between heavy-flavor (c, b) and light-quark (u, d, s) or gluon jets, caused by neutrinos produced in semileptonic decays of heavy-flavor hadrons. It should be noted that the neutrino fraction leads to an additional systematic uncertainty in the heavy hadrons fragmentation relative to the original b and c quarks that is not included in JEC systematics, but should be considered in, e.g., measurements of the inclusive b-jet cross section or of the top quark mass. The performance of the corrections for b jets is discussed in section 7.4. The variables referring to particle-level jets are labeled “ptcl" in this document.

We consider two types of reconstructed jets, depending on how the subdetector information is used: calorimeter jets and PF jets.

The **calorimeter (CALO) jets** are reconstructed from energy deposits in the calorimeter towers alone. A calorimeter tower consists of one or more HCAL cells and the geometrically corresponding ECAL crystals. In the barrel region of the calorimeters, the unweighted sum of one single HCAL cell and 5×5 ECAL crystals form a projective calorimeter tower. The association between HCAL cells and ECAL crystals is more complex in the endcap regions. A four-momentum is associated with each tower deposit above a certain threshold, assuming zero mass, and taking the direction of the tower position as seen from the interaction point.

The **PF jets** are reconstructed by clustering the four-momentum vectors of PF candidates. The PF jet momentum and spatial resolutions are greatly improved with respect to calorimeter jets, as the use of the tracking detectors and high granularity of the ECAL improves the energy resolution through the independent measurements of charged hadrons and photons inside a jet, which together

2017 JINST 12 P02014

constitute ≈85% of the average jet energy. In reconstructing the PF candidate four-momentum, photons are assumed massless and charged hadrons are assigned the charged pion mass.

Calorimeter jets result from a relatively simplistic yet robust approach and were widely used in the early CMS publications. With the improvement of the understanding of the detector and the commissioning of the reconstruction with data, the performance of the PF reconstruction has proven to be outstanding and reliable. The event description and reconstruction is more complete and consistent, and for these reasons, we focus here on the PF jets used in the majority of recent CMS analyses.

3 Event samples and selection criteria

3.1 Simulated samples

Simulated samples are generated for QCD dijet and multijet, Z+jet, and γ+jet processes. A sample with single-neutrino production is simulated as well, to reproduce empty events that only contain pileup and detector noise. The dijet, γ+jet and single-neutrino samples are generated with PYTHIA 6.4 [19], using the tune Z2* [20]. The Z+jet and multijet samples are generated with the MADGRAPH 4 [25] program matched with parton showers simulated by PYTHIA 6.4 tune Z2*. Additional samples for systematic uncertainty studies are available for QCD dijet and Z+jet processes, both generated with HERWIG++ 2.3 [21], tune EE3C [22]. The single-neutrino sample is compared to zero-bias data (section 4.3). The dijet sample is used to simulate the jet response (section 5) and also in comparison to data in the dijet balance analysis (section 6.1). The Z+jet and γ+jet simulated samples are used in comparisons of measured response with the corresponding selected samples of data (section 6.3). The multijet sample is used in the multijet balance analysis (section 6.3).

Additional samples are used for the analysis of events with a Z boson and a b jet (section 7.4): the MADGRAPH 4 program, together with PYTHIA 6.4 for the hadronization, is used to simulate top quark pair, W+jets and Drell-Yan+jets (DY+jets) production; and the POWHEG [26] program, together with PYTHIA 6.4 for the hadronization, is used for single top quark samples. A DY+jets sample produced with HERWIG++ 2.3 is also used for studies of systematic uncertainties.

All generated samples are processed through the CMS detector simulation, based on GEANT4 [18]. Minimum bias events, generated with PYTHIA 6.4 and tune Z2*, are overlayed to all above samples to simulate the pileup. As will be detailed in section 4, the MC simulation is reweighted to match the distribution of the average number of pileup interactions in data.

3.2 Data sets and event selection

The studies presented in this document use the data collected by the CMS experiment in proton-proton collisions at a center-of-mass energy of 8 TeV, during the year 2012, corresponding to an integrated luminosity of 19.7 fb^{-1}. In this section we describe the selection criteria used in the different analyses presented in this paper. Only data collected during stable-conditions collisions with a fully-functioning detector are considered. Apart from the zero-bias sample, all data samples are required to fulfill some basic event preselection criteria. The presence of at least one well-reconstructed primary vertex (PV) is required [27], with at least four tracks considered in the vertex fit, and with $|z(\text{PV})| < 24$ cm, where $z(\text{PV})$ represents the position of the PV along the beam axis. The radial position of the primary vertex, $r_{xy}(\text{PV})$, has to satisfy the condition $r_{xy}(\text{PV}) < 2$

2017 JINST 12 P02014

cm. Finally, the jets used in the analyses are required to satisfy basic identification criteria ("Jet ID") [28], which on simulation are found to retain more than 99% of genuine jets, while rejecting most of the misreconstructed jets arising from detector noise or cosmic muons.

Zero-bias sample. The zero-bias sample is collected using a random trigger in the presence of a beam crossing with filled bunches, active during the whole data-taking period with stable collisions conditions and a fully-functioning detector. As these events are not triggered by any specific energy deposit, they generally do not contain any contribution from hard-scattering processes. The main sources of energy deposits in zero-bias events are detector noise and pileup. The events in the dataset are weighted, according to the luminosity evolution during the running period, in order to be representative of the average pileup conditions of the datasets used in the analyses presented in this paper.

Dijet sample. The dijet sample, composed of events with at least two jets in the final state, is collected using dedicated HLTs, which accept the events depending on the value of the average p_T ($p_{T,ave} = (p_{T,\,1st\,jet} + p_{T,\,2nd\,jet})/2$) of the two highest-$p_T$ jets in the event, to ensure an unbiased data set. The HLT uses a PF reconstruction algorithm with simplified tracking, and the jet p_T is corrected for nonuniformity of the energy response as a function of the jet η and p_T. Several $p_{T,ave}$ thresholds are available, with different prescale factors. Depending on the value of the highest jet p_T in the event, only the least prescaled fully efficient HLT is used for the decision of keeping or rejecting the event for further analysis. Events selected with single-jet triggers are also used for the studies of jet composition shown in section 10.

The event selection requires at least one of the two leading jets to have $|\eta| < 1.3$ and the angular separation between the two leading jets in the (x, y) plane to be $|\Delta\phi_{1st\,jet,\,2nd\,jet}| > 2.7$. Events are rejected if there is any third jet with $p_{T,\,3rd\,jet} > 5\,GeV$ not fulfilling the condition $p_{T,\,3rdjet}/p_{T,ave} = \alpha < 0.2$. As will be explained in section 6.1, the results are studied as a function of the α cut from $\alpha < 0.4$ to $\alpha < 0.1$ in order to correct for biases from ISR+FSR.

The Z+jet sample. The Z($\to \mu\mu$)+jet and Z($\to$ ee)+jet samples are collected using single-lepton HLTs with various p_T thresholds. Events are required to contain either two opposite-sign muons or two opposite-sign electrons, fulfilling standard tight isolation and identification requirements [29, 30], with $|\eta| < 2.3$ and $p_T > 20\,GeV$. The dilepton ($\ell\ell$) system is required to have $p_{T,ll} > 30\,GeV$ and $|m_{ll} - m_Z| < 20\,GeV$, where m_Z is the mass of the Z boson. The leading jet in the event is required to have $|\eta| < 1.3$ and $p_T > 12\,GeV$, and to have a large angular separation in the (x, y) plane with respect to the dilepton system, $|\Delta\phi(Z, 1st\,jet)| > 2.8$. Events are rejected if there is any second jet with $p_{T,\,2nd\,jet} > 5\,GeV$ not fulfilling the condition $p_{T,2nd\,jet}/p_{T,Z} = \alpha < 0.3$. The value of the cut on $|\Delta\phi(Z, 1st\,jet)|$ is such that it does not bias the distribution of α for $\alpha < 0.3$. As will be explained in section 6.3, the requirement on α is tightened from the nominal value of 0.3 and the results are studied as a function of its value. In the Z($\to$ ee)+jet analysis an additional requirement is enforced that no electron in the event lie within $\Delta R = \sqrt{(\Delta\phi)^2 + (\Delta\eta)^2} = 0.5$ of a jet. The Z+jet selection is also used in section 7.4, with the additional requirement that the jet is tagged as coming from a b quark using the combined secondary vertex tagger [31], with a typical tagging efficiency of 70% and a misidentification probability for light-flavor jets of 1%.

2017 JINST 12 P02014

The γ+jet sample. The γ+jet sample is collected with single-photon HLTs with various p_T thresholds and different prescale factors. Depending on the value of the highest photon p_T in the event, only the least prescaled fully efficient HLT is used for the decision of keeping or rejecting the event for further analysis. Events are required to contain one, and only one, photon with $p_T > 40$ GeV and $|\eta| < 1.3$ that fulfills the standard tight cut-based photon identification and isolation criteria [32]. The leading jet in the event is required to have $|\eta| < 1.3$ and $p_T > 12$ GeV and to have a significant angular separation in the (x, y) plane with respect to the photon, $|\Delta\phi(\gamma, \text{1st jet})| > 2.8$. Events are rejected if there is any second jet with $p_{T,\text{ 2nd jet}} > 5$ GeV not fulfilling the condition $p_{T,\text{2nd jet}}/p_{T,\gamma} = \alpha < 0.3$. As will be explained in section 6.3, the requirement on α is tightened from the nominal value of 0.3 and the results are studied as a function of its value.

Multijet sample. The multijet sample is collected with single-jet HLTs with various p_T thresholds and different prescale factors. Depending on the value of the highest jet p_T in the event, only the least prescaled fully efficient HLT is used for the decision of keeping or rejecting the event for further analysis. The event selection is inspired by the analysis described in ref. [14]. Events containing isolated leptons or photons passing standard identification criteria are rejected. The events are required to have a $p_T > 250$ GeV jet in $|\eta| < 1.3$ balanced by a recoil system, composed of two or more low-p_T jets with $25 < p_T < 750$ GeV, which is within the range calibrated by the Z/γ+jet events, and satisfying the condition $p_{T,\text{ 2nd jet}}/p_{T,\text{recoil}} < 0.6$. The events are also required to have the recoil jets at least $\Delta\phi(\text{1st jet, recoil jet}) > 1$ radians away from the leading jet in the transverse plane, and to have the recoil system back-to-back with the leading jet with $|\Delta\phi(\text{1st jet, recoil syst.}) - \pi| < 0.3$. As will be explained in section 6.3, all jets with $|\eta| < 5$, $p_T > 10$ GeV are considered to be part of the recoil system; the analysis is also repeated after changing to $p_T > 20$ and 30 GeV the transverse momentum threshold for jets to be considered in the recoil.

4 Pileup offset corrections

The high instantaneous luminosity at the LHC results in multiple proton-proton collisions taking place within a single beam crossing. Such additional pp collisions occurring within the same bunch-crossing as the primary hard interaction produce additional tracks in the tracker and deposit energy in the calorimeters. This contribution is called in-time pileup (IT PU). Due to the finite signal decay time in the calorimeters, the pp collisions occurring in the previous and subsequent beam crossings also contribute to calorimetric energy in the same time window as the primary hard interaction. This contribution is called out-of-time pileup (OOT PU).

The additional contributions to the jet energy and momentum due to pileup are referred to as the “pileup offset", or “offset" in this document. This offset is studied to optimize the subtraction of pileup from the data, with the corrections leading to an improved detector resolution and a more accurate JES.

The observables used for monitoring and correcting pileup are described in section 4.1. The pileup subtraction then proceeds in steps. The OOT PU is mitigated by calorimeter signal processing (section 4.2), and the IT PU by identifying charged particles originating from pileup vertices and removing them with charged-hadron subtraction (section 4.2). The pileup jets are tagged with pileup jet identification (PUJetID) and removed (section 4.2). The remaining diffuse energy from neutral

2017 JINST 12 P02014

particles and OOT PU is estimated per event and then subtracted per jet using a calculation of the effective jet area with the extended hybrid jet area method (section 4.3). The dependence of the particle-level PU offset on jet η and p_T for this method is determined from simulation (section 4.3), and the data/simulation offset scale factor is determined from zero-bias data and neutrino gun simulation, with the random cone (RC) method (section 4.3). The uncertainties are discussed in section 4.4 and the results are summarized in section 4.5.

4.1 Pileup observables

The amount of pileup present in the event can be estimated by counting the number of good-quality primary vertices N_{PV} or by calculating the diffuse offset energy density ρ [33, 34] in the event. It can also be measured using luminosity monitors that estimate the average number of pileup interactions per crossing.

The offset energy density ρ is calculated using the k_T clustering algorithm [35–37] with distance parameter $D = 0.6$ and $|\eta| < 4.7$. For this calculation, a large number of nonphysical particles (ghosts) with infinitesimal momenta and random direction effectively mapping all the (η, ϕ) space, is added to the event. When the jet clustering is run on the event, the hard particles in the event are clustered together with such ghosts: a few jets will contain high-momentum particles from the hard-scattering interaction, but most of the jets will be entirely made of ghosts, for which the main real energy contributions come from detector noise and especially pileup. The offset energy density ρ is defined, in each event, as the median of jet momenta $p_{T,i}$ divided by their area A_i, $\rho = \text{median}(p_{T,i}/A_i)$ [38]. For this calculation, no selection on the jet momenta is applied. Using the median instead of the mean makes ρ effectively insensitive to hard jets in the event, and including zero-energy jets composed of only ghost particles reduces bias for low pileup energy densities. For Run 2, a simpler approach is used to calculate ρ, which is evaluated as the median of the energies calculated in a grid of $\eta - \phi$ cells, and does not make use of jet clustering anymore.

The number of good primary vertices N_{PV} includes vertices consistent with the luminous region (where the collisions happen) and with a number of degrees of freedom $N_{dof} \geq 4$, corresponding to a minimum of four tracks.

The average number of pileup interactions μ is obtained by multiplying the instantaneous luminosity with the effective minimum bias cross section of $\sigma_{MB} = 69.4$ mb for 8 TeV (68.0 mb for 7 TeV) [39]. Two detectors are exploited for the luminosity measurement: the hadron forward (HF) calorimeter and the silicon pixel detector. The counting of pixel clusters is used for the offline precision measurement, because of its time stability and very small dependence on pileup. The HF allows for online determination of instantaneous luminosity per bunch crossing. Its results, calibrated offline per luminosity section that corresponds to 23.3 seconds of data, are used for cross-checks [40].

The agreement between data and simulation on N_{PV} and ρ, after reweighting the simulation to match the distribution of the average number of pileup interactions (μ) in data, is shown in figure 3. The agreement for N_{PV} is excellent, while ρ exhibits a small, mostly linear, deviation that is due to different offset densities in data and simulation in the endcap and forward calorimeters.

Both N_{PV} and ρ are very nearly linearly dependent on μ over the tested range, as shown in figure 4. The pileup vertex reconstruction and identification efficiency is about 70% (while nearly 100% for hard-scattering events), and IT PU contributes about 0.5 GeV to ρ per interaction. The vertex z resolution is around 100–300 μm for minimum-bias vertices, improving to tens of microns

2017 JINST 12 P02014

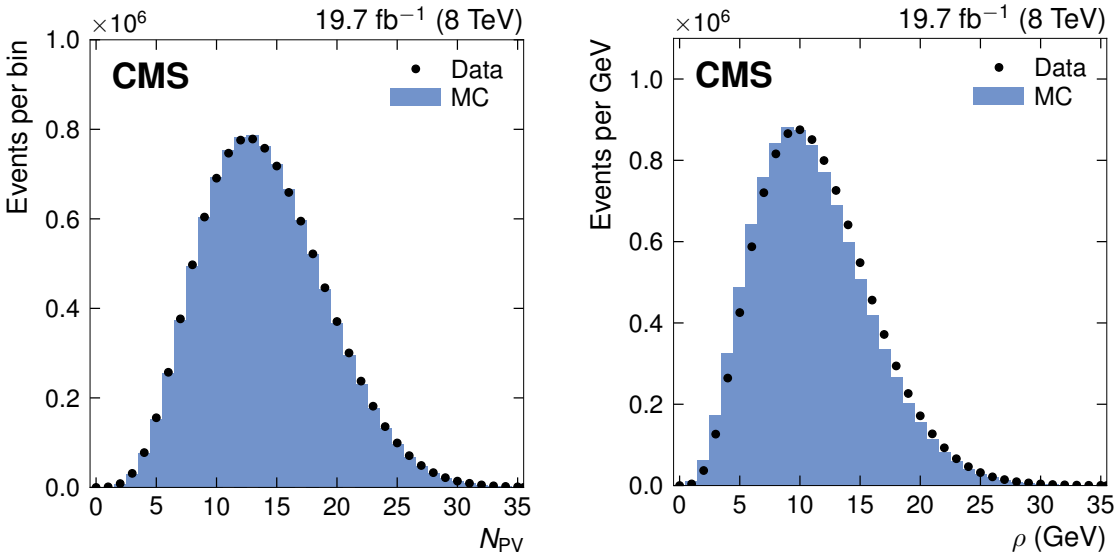

Figure 3. Comparison of data (circles) and PYTHIA 6.4 simulation (histograms) for the distributions of the number of reconstructed primary vertices N_{PV} (left), and of the offset energy density ρ (right).

for hard-scattering events. With a luminous region of root-mean-square (RMS) of about 4 cm in the z direction, the vertex reconstruction is expected to remain linear up to 100–200 vertices. The N_{PV} versus μ exhibits a small negative quadratic term due to infrequent merging of pileup vertices, while ρ versus μ exhibits a similarly small positive quadratic term owing to effects such as effective failed zero-suppression of overlapping calorimeter deposits. These quadratic terms account for less than 0.5 vertices in N_{PV} and 0.5 GeV in ρ at $\mu = 20$, respectively.

The correlation between IT PU and OOT PU is modeled by generating the number of interactions for each bunch crossing using a Poisson distribution with the same mean μ. This is a good approximation for 2012 (8 TeV) data, given that the RMS of the bunch-to-bunch variation of μ within a single luminosity section was only about 8%. The value of N_{PV} is insensitive to OOT PU, while ρ has a small (<5% of the total) OOT PU component with 50 ns bunch crossings. The N_{PV} variable is highly (≈94%) correlated with the number of IT PU interactions in the event, while ρ is also sensitive to the amount of energy deposited by each interaction, and thus less strongly (≈85%) correlated with the interaction multiplicity.

4.2 Pileup mitigation

Out-of-time pileup. The amount of OOT PU can be reduced by shortening the signal time-integration window and by increasing the separation between bunches.

In HCAL, 68% of the signal is contained within a 25 ns time window [41], resulting in about 5% leakage to a subsequent crossing with 50 ns bunch spacing and 50 ns time integration window. The signal decay time in ECAL is of the order of 100 ns, but the ECAL reconstruction involves three samples of 25 ns before the signal and five on the signal, to remove a varying pedestal. This removes OOT PU on average, but with performance depending on the position of the proton bunch within the bunch train, and requiring simulation of up to six preceding bunch crossings (−300 ns).

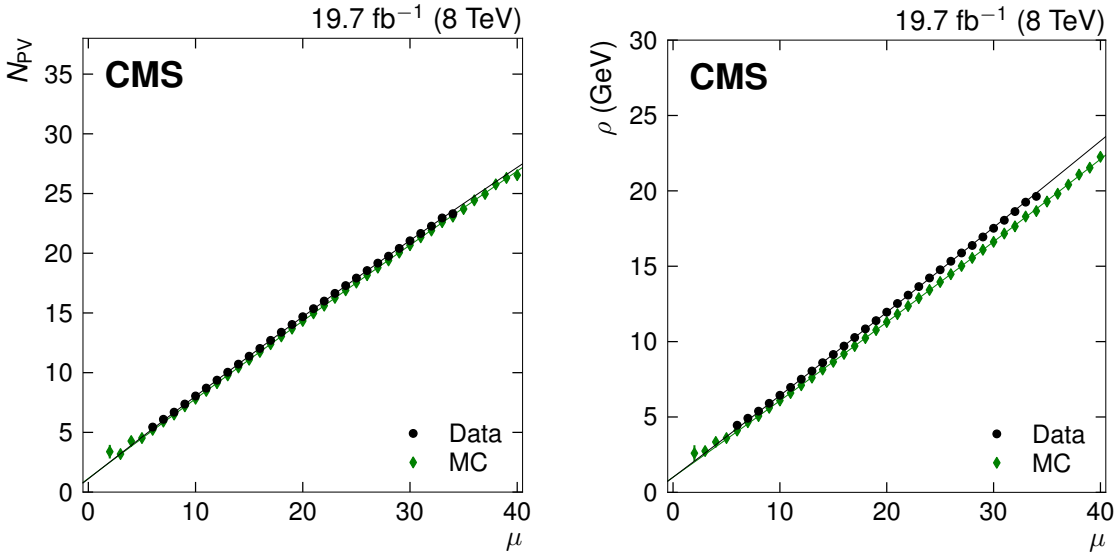

Figure 4. Mean of the number of good primary vertices per event, $\langle N_{PV} \rangle$ (left), and mean diffuse offset energy density, $\langle \rho \rangle$ (right), versus the average number of pileup interactions per bunch crossing, μ, for data (circles) and PYTHIA 6.4 simulation (diamonds).

The variation in the offset correction can be up to 10% in the endcaps when selecting bunches in the front of bunch trains, which represent a small fraction ($< 10\%$) of data. The correction is evaluated on the whole dataset and hence this effect averages out. In HF, the signal is only 10 ns wide, resulting in negligible OOT PU without any special treatment of the signal.

More advanced techniques are used in Run 2, exploiting the signal timing and pulse shape to fit in-time and out-of-time pulses simultaneously.

Charged-hadron subtraction. The IT PU from charged particles is reduced by identifying which vertex the charged PF candidates originate from, and removing those unambiguously associated with pileup vertices before clustering jets and $\vec{p}_{\mathrm{T}}^{\,\mathrm{miss}}$. This method is referred to as charged-hadron subtraction.

The leading primary vertex is chosen based on the largest sum of squares of the tracks transverse momenta ($\sum |p_{\mathrm{T}}^{\mathrm{track}}|^2$) associated with the vertex. Subleading PV's, classified as pileup vertices, are required to pass further quality criteria on the compatibility with the luminous region and on their minimum number of degrees of freedom

$$N_{\mathrm{dof}} = -3 + 2 \sum_{i=1}^{\mathrm{nTracks}} w_i, \qquad \text{and} \quad w_i \in [0, 1], \tag{4.1}$$

where w_i is the weight assigned to the corresponding track by the adaptive vertex fit [27], based on its compatibility with the vertex. The minimum requirement $N_{\mathrm{dof}} > 4$ corresponds to at least four tracks. Tracks are matched to vertices based on their chi-squared per degree of freedom (χ^2/N_{dof}). If $\chi^2/N_{\mathrm{dof}} < 20$ for a vertex, then the track is associated with this and only this vertex. If the track from a charged hadron is associated with a pileup PV, passing the above quality requirements, it is

2017 JINST 12 P02014

considered a pileup track, and removed in the CHS procedure. All other tracks, including those not associated with any PV, are kept.

The CHS can remove approximately 50% of IT PU within the tracker coverage, as illustrated later by the solid red component labeled "charged hadrons" in figures 6 and 7. The remaining unassociated charged hadrons are either not pointing to any reconstructed vertex, or are associated with a vertex that did not pass all the quality requirements, or have too large χ^2/N_{dof} for robust vertex association. The vertex reconstruction and identification inefficiency is about 30% for pileup vertices, and it is responsible for a large proportion of the unassociated tracks from pileup.

The charged hadrons from PU are typically soft and have an exponentially decreasing p_{T} distribution, with $\langle p_{\mathrm{T}} \rangle \approx 0.5\,\mathrm{GeV}$ [42]. Many of the unassociated hadrons in contrast have much higher p_{T} and are often coming from the leading primary vertex, but have too high χ^2/N_{dof} for robust vertex association. This is particularly common for tracks that are of high p_{T} and therefore very straight and have merged pixel hits within dense jet cores. For jets of several hundred GeV the tracking efficiency within the jet core can fall as low as 60%, with a correspondingly large increase of the fraction of unassociated tracks. Future improvements of CHS aimed at removing a higher proportion of pileup tracks, e.g., with more efficient track-vertex association, must therefore maintain a very low misreconstruction rate for tracks from high-p_{T} jets, or also consider the p_{T} and local environment of the tracks, as done with the pileup per particle ID (PUPPI) method [43].

The PU offset subtraction has been derived with and without CHS, and the later stages of JEC are practically identical after the application of the corresponding offset corrections. Application of CHS improves the jet p_{T} resolution, however, as discussed in section 8.

Pileup jet identification. In addition to diffuse energy, PU interactions often generate soft jets with p_{T} of a few GeV. Overlaying multiple PU interactions in a single beam-crossing leads to nonnegligible probability of two or more of these soft jets overlapping, resulting in hard jets of tens of GeV in p_{T}, far above the average PU p_{T} density. These overlaps are referred to as pileup jets, which are particularly problematic for physics analyses as they can pass typical jet p_{T} requirements, e.g., $p_{\mathrm{T}} > 30\,\mathrm{GeV}$. The pileup jets lack the relatively hard core typically found in hard-scattering jets, and can be identified by using a multivariate analysis (MVA) of the jet shape variables and the fraction of charged particles contributed by pileup vertices. This MVA tool is called PUJetID, can be run on jets with or without CHS, and it is documented in ref. [44]. For jets in the region $|\eta| < 2.5$ and $p_T > 30\,\mathrm{GeV}$, the PUJetID efficiency for hard-scattering jets is around 99%, at a pileup-rejection of 90 – 95%.

Removing pileup jets can improve the performance of physics analyses, but applying PUJetID has no direct impact on the JEC. PUJetID is currently not used in the JEC measurements to avoid biases arising from the occasional removal of soft jets from the hard-scattering vertex, which affects the ISR+FSR correction. Instead, CHS is used, which indirectly removes most of the jets tagged by PUJetID by significantly lowering their p_{T}.

4.3 Hybrid jet area method

The jet area method uses the effective area of the jets multiplied by the average energy density in the event to calculate the offset energy to be subtracted from the jets. This method was introduced in ref. [33] and was first used on data in ref. [13] with slight modifications to account for the oversubtraction of the underlying event (UE) and for the η-dependence of the offset. This slightly

2017 JINST 12 P02014

modified version is referred to as the hybrid jet area method, where the "hybrid" in the name derives from the fact that this method combines an η-dependent average offset $O(\eta)$ correction versus N_{PV}, as already used at the Tevatron [16], with the original η-independent jet area method using only offset p_{T} density ρ and jet area A_j. This is effectively done by replacing $(N_{\mathrm{PV}} - 1)O(\eta)$ in the Tevatron method with $(\rho - \rho_{\mathrm{UE}})(\beta(\eta)A_j)$, where each of the terms N_{PV} and ρ, -1 and $-\rho_{\mathrm{UE}}$, and $O(\eta)$ and $\beta(\eta)\langle A_j\rangle$ have the same basic meaning, which will be detailed in the following.

In this paper we further extend the hybrid method by adding a logarithmic jet p_{T} dependence. The previous separate UE correction is absorbed in the new η-dependent constant term. The full correction formula used as a multiplicative factor for the uncorrected jet transverse momentum $p_{\mathrm{T,uncorr}}$ at CMS is

$$C_{\mathrm{hybrid}}(p_{\mathrm{T,\,uncorr}}, \eta, A_j, \rho) = 1 - \frac{\left[\rho_0(\eta) + \rho\beta(\eta)\,(1 + \gamma(\eta)\log(p_{\mathrm{T,\,uncorr}}))\right] A_j}{p_{\mathrm{T,\,uncorr}}}. \tag{4.2}$$

The input parameters are $p_{\mathrm{T,\,uncorr}}$, jet pseudorapidity η, jet area A_j, and the per-event p_{T} offset density ρ. In this formula the parameters $\rho_0(\eta)$, $\beta(\eta)$, and $\gamma(\eta)$ introduce the required shaping of the offset versus η. There is no explicit correction for the UE density ρ_{UE} as in ref. [13], but that term is effectively absorbed into $\rho_0(\eta)$. Because $\rho \to \rho_{\mathrm{UE}}$ and $C_{\mathrm{hybrid}} \to 1$ when $\mu \to 0$, we have $\rho_0(\eta) = -\rho_{\mathrm{UE}}\beta(\eta)$ at $p_{\mathrm{T,uncorr}} \to 1$ GeV in the ideal situation. The multiplicative factor, $\beta(\eta)$, corrects for the nonuniformity of the IT and OOT PU offsets versus η, and the residual correction factor, $\gamma(\eta)$, adds their logarithmic jet p_{T} dependence.

The parameters $\rho_0(\eta)$, $\beta(\eta)$, and $\gamma(\eta)$ are determined from the simulated particle-level offset, and the offset scale factor for the $\rho_0(\eta)$ and $\beta(\eta)$ in data is determined using the random cone method in zero-bias data, as discussed in the following. The $\rho_0(\eta)$ parameter effectively contains the ρ_{UE} for the QCD multijet sample, while $\beta(\eta)$ and $\gamma(\eta)$ parameterize the PYTHIA 6.4 MinBias overlay, which matches data well. The RC method consists of reconstructing many jets in each event, clustering particles in randomly placed cones, effectively mapping all the (η, ϕ) space. The average p_{T} of these jets is a measurement, in each event, of the average energy density that gets clustered in a jet. When the method is applied in events with no contribution from hard scattering, as it is the case for zero-bias events, the main contributions to the jet energies come from noise and pileup. Assuming the noise energy contribution to be negligible with respect to the pileup one, the average p_{T} of the jets as measured from the RC method indicates the average energy offset due to pileup, for the considered jet algorithm and jet distance parameter.

Simulated particle-level offset. In simulation, the most direct way to calculate the particle-level offset in jet p_{T} caused by pileup is to reconstruct the same events with and without pileup overlay and match the reconstructed jets between these samples. This is done on a QCD multijet sample generated with PYTHIA 6.4, tune Z2*. Some care needs to be taken to reproduce the same signal fluctuations as before the overlaying pileup, to avoid random smearing of jet p_{T} between these two samples. All measurements are binned in μ to decouple pileup reweighting from offset measurement, and to effectively incorporate the correct average amount of OOT PU in the offset correction (OOT and IT PU are correlated through the shared Poisson mean μ). The μ bins are then mapped to the average measured value of $\langle\rho\rangle$ for parameterizing the correction. Similarly, the p_{T} dependence of the offset is measured in bins of particle jet p_{T} ($p_{\mathrm{T,\,ptcl}}$) to decouple the offset

2017 JINST 12 P02014

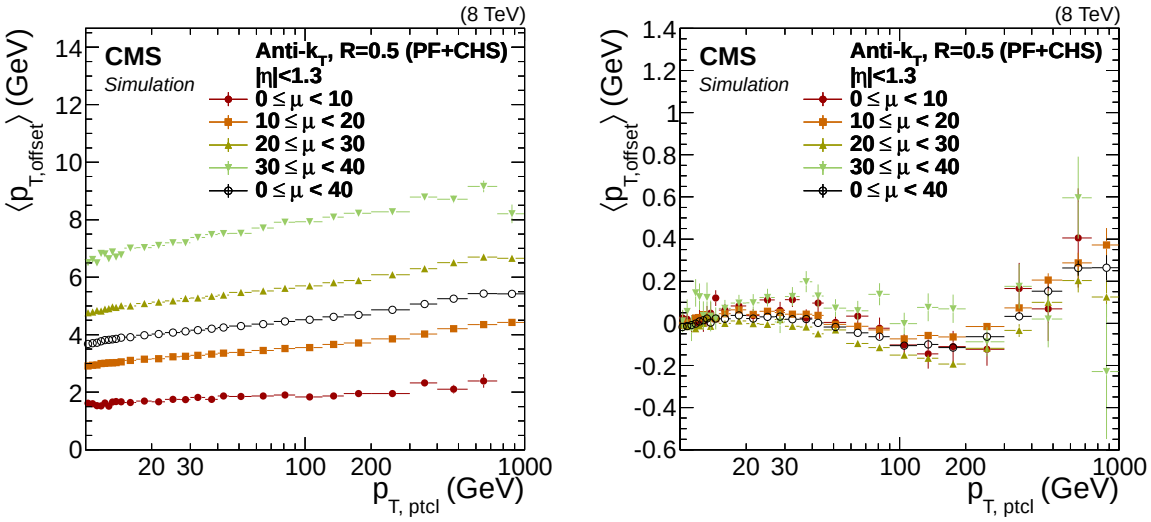

Figure 5. Simulated particle-level offset $\langle p_{\mathrm{T,offset\ ptcl}}\rangle$ defined in eq. (4.3) (left), and residual offset after correcting for pileup with eq. (4.2) (right) for $|\eta| < 1.3$, versus particle jet p_{T}, for different values of average number of pileup interactions per bunch crossing $\langle\mu\rangle$.

from the p_{T} spectrum and JER, before mapping to the average uncorrected measured $\langle p_{\mathrm{T,uncorr}}\rangle$ for parameterization.

We define the particle-level offset $\langle p_{\mathrm{T,offset\ ptcl}}\rangle$ as the average difference in p_{T} between matched jets in simulated samples with and without pileup overlay:

$$\langle p_{\mathrm{T,offset\ ptcl}}\rangle(\langle\rho\rangle, [\eta], \langle p_{\mathrm{T,uncorr}}\rangle) = \langle p_{\mathrm{T,with\ PU}} - p_{\mathrm{T,without\ PU}}\rangle \left[\mu_{\mathrm{PU}}, \eta, p_{\mathrm{T,\ ptcl}}\right]. \tag{4.3}$$

The square brackets [ ] denote the binning variables, while the angle brackets ⟨ ⟩ denote the averages within those bins for the variables that are used to parameterize the corrections. This subtle distinction is made explicit here due to its importance for various observational biases, and due to the fact that the binning and parameterization variables are not the same. To have an unambiguous particle-level reference, both reconstructed jets are required to match the same particle jet within a distance less than $\Delta R < R/2$, where R is the jet distance parameter. The matching efficiency for jets in the without-PU sample to jets in the with-PU sample for $\langle\mu\rangle = 20$ is better than 80% (98%) for jets of $p_{\mathrm{T}} > 10$ (30) GeV. In the with-PU sample there is also a large fraction of unmatched jets with $p_{\mathrm{T}} < 60$ GeV that are due to pileup.

The simulated particle-level offset $\langle p_{\mathrm{T,offset\ ptcl}}\rangle$ is parameterized as a function of offset density ρ and jet η, $p_{\mathrm{T,uncorr}}$ and area A_j to obtain the $\rho_0(\eta)$, $\beta(\eta)$ and $\gamma(\eta)$ used in eq. (4.2), where $C_{\mathrm{hybrid}} = 1 - \langle p_{\mathrm{T,offset\ ptcl}}\rangle / p_{\mathrm{T,uncorr.}}$. The particle-level simulated offset versus particle jet p_{T} is shown in figure 5 (left) for $|\eta| < 1.3$. The relative slope in offset is parameterized by a logarithmic p_{T} dependence and is reasonably independent of the level of pileup in the event, while the offset versus ρ is assumed linear. The resultant level of pileup after applying the corrections is presented in figure 5 (right), showing the effect of the subtraction. The results are consistent with the absence of additional pileup energy within about 0.2 GeV for the full sample. For $\mu > 30$, small residual offset is visible due to a small unparameterized quadratic dependence of offset on ρ.

2017 JINST 12 P02014

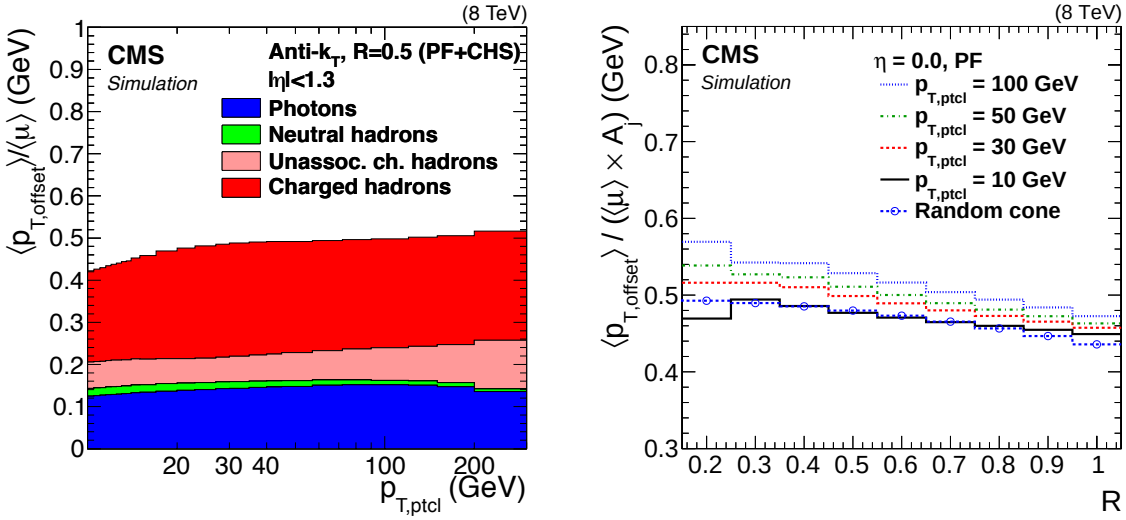

Figure 6. Simulated particle-level offset versus p_T separately for each type of PF candidate (left). Average p_T offset density versus jet distance parameter R for various $p_{T,ptcl}$ compared to a random-cone offset density versus cone radius (right). The jet or cone area A_j corresponds to πR^2.

Figure 6 (left) shows the p_T dependence of the offset for each PF candidate type. The $\langle p_{T,offset} \rangle$ is divided by the average number of pileup interactions, hence showing the average offset per additional interaction. While the reconstruction thresholds for charged hadrons and photons are of the order of a few hundred MeV, the effective detector reconstruction thresholds for neutral hadrons (mostly K^0_L, K^0_S, and neutrons) are of the order of 3 GeV. This is far above the typical $\langle p_{T,offset} \rangle \approx 5$ GeV for a pileup particle, making the neutral hadron contribution barely visible in figure 6 (left). The observed p_T dependence comes from an interplay of several effects for overlapping particles, such as failed zero-suppression in calorimeter energy, nonlinearity of PF hadron corrections, fake tracks arising from hit combinations, and misreconstructed tracks arising from pixel hit merging and tracker dynamic inefficiency at high μ. The rate of overlaps is highest in the jet core, which results in the simulated offset correction depending on the jet size. Figure 6 (right) shows the average offset density within the jet versus jet distance parameter R and jet p_T. The simulated particle-level offset converges to an RC offset measurement at low p_T, as well as for large jet size parameters. The shallow slope in RC offset versus distance parameter is due to vector summation of PF candidate momenta, which reduces the offset p_T relative to the offset energy by $\cos(\Delta R)$ at the cone edges.

Offset scale factor. The offset data/simulation scale factor is estimated from zero-bias data and simulation using the RC method [13]. Because zero-bias data contain no energy deposition from hard interactions, and the noise contribution is small, the average transverse momentum $\langle p_{T,cone} \rangle(\eta)$ of PF candidates in a randomly placed cone centered at (η, ϕ) can be identified with the average offset due to pileup, $\langle p_{T,offset} \rangle^{RC}(\eta)$:

$$\langle p_{T,offset} \rangle^{RC}(\eta, \langle \rho \rangle) = \langle p_{T,cone} \rangle[\eta, \mu]. \tag{4.4}$$

As in the case of the simulated particle-level offset, the parameterization variables $(\eta, \langle \rho \rangle)$ and the binning variables $[\eta, \mu]$ are explicitly marked in order to signal their impact on the observational biases.

2017 JINST 12 P02014

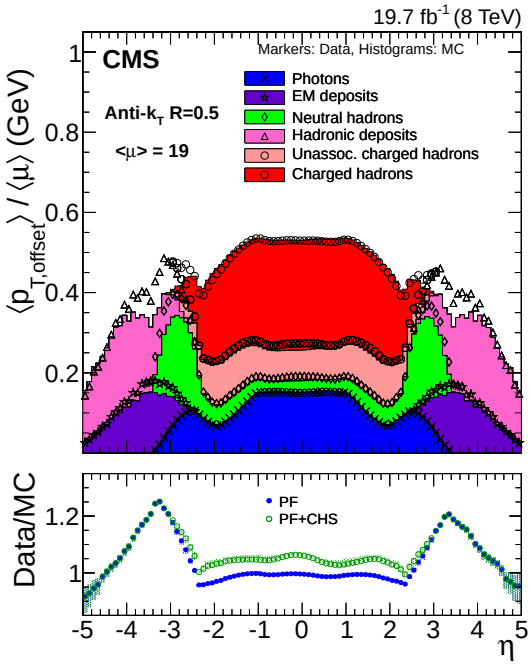

Figure 7. Random-cone offset measured in data (markers) and MC simulation (histograms) normalized by the average number of pileup interactions $\langle\mu\rangle$, separated by the type of PF candidate. The fraction labeled 'charged hadrons' is removed by CHS. The ratio of data over simulation, representing the scale factor applied for pileup offset in data, is also shown for PF and PF+CHS.

For deriving the offset scale factor, the RC measurement is fitted with a quadratic function of ρ, $\langle p_{\mathrm{T,offset}}\rangle^{\mathrm{RC}} = p_0 + p_1\rho + p_2\rho^2$. The constant and quadratic terms are small, but are required for a good χ^2/N_{dof} of the fit. The constant term has usually a small positive value, because the mean $\langle p_{\mathrm{T,cone}}\rangle$ can still have a small nonzero value when the median ρ is already zero. This low-PU behavior of ρ is discussed in ref. [45]. The offset scale factor for parameters $\rho_0(\eta)$ and $\beta(\eta)$ in eq. (4.2) is defined as

$$\frac{\langle p_{\mathrm{T,offset}}\rangle^{\mathrm{RC}}_{\mathrm{data}}(\eta, \langle\rho\rangle_{\mathrm{data}})}{\langle p_{\mathrm{T,offset}}\rangle^{\mathrm{RC}}_{\mathrm{MC}}(\eta, \langle\rho\rangle_{\mathrm{MC}})}. \tag{4.5}$$

Using different $\langle\rho\rangle$ working points for data and simulation is necessary due to the slight difference of about 4% in $\langle\rho\rangle$ between data and simulation, seen in figure 3 (right).

The offsets in data and simulation are shown in figure 7 (top), separated by PF candidate type. The offset scale factor for PF and PF+CHS is shown in figure 7 (bottom). The offset scale factor at $|\eta| < 2.4$ is less than 5%, but increases up to 20% outside of the tracking coverage near the inner edge of HF at $\eta \approx 3.2$. The triangular shape is caused by smearing sharp detector effects over a cone area within $\Delta\eta < 0.5$. The uncertainty from varying the $\langle\rho\rangle$ working point within the 68% confidence interval of the ρ distribution is less than 2% up to $|\eta| < 4.7$.

4.4 Pileup offset correction uncertainties

The pileup offset correction uncertainties come from two main sources: uncertainty in the offset scale factor used for the η dependence in data, and uncertainty in the offset jet p_{T} dependence that is

2017 JINST 12 P02014

derived from simulation only. The former uncertainty is evaluated by varying the $\langle\rho\rangle$ working point used for deriving the offset scale factor within one standard deviation of the ρ distribution, while the latter is evaluated using the difference between the simulated particle-level offset and the RC offset. Of these, the jet p_T dependence is the dominant uncertainty across most of the phase space.

Any residual pileup offset is absorbed on average, within the constraints of their respective parameterizations, by the relative η and absolute p_T corrections derived from dijet, Z+jet, γ+jet and multijet data. Therefore the dominant p_T-dependence uncertainty is propagated through the fit procedure used in the data-based methods to account for this reduction and shaping of pileup offset correction uncertainties. This results in a set of five uncertainty sources:

- *PileUpEnvelope* is taken as 30% of the difference between simulated particle-level offset and RC offset. This is the pileup uncertainty we would have if the later calibrations did not reduce the uncertainty. It is not directly included in the JEC uncertainties, but is propagated through the relative η and absolute p_T corrections to give the uncertainties *PileUpPtEta*, *PileUpPtRef* (for $\langle\mu\rangle \approx 20$ data) and *PileUpMuZero* (for $\langle\mu\rangle = 0$ data), described below.

- *PileUpPtEta* (Eta=BB,EC1,EC2,HF) results from the propagation of the *PileUpEnvelope* uncertainty through the η-dependent correction evaluation from dijet balance. This uncertainty accounts for the residual difference between the *PileUpEnvelope* with shape $(p_0 + p_1 \log(p_T))/p_T$ and the η-dependent correction fit in the range of dijet data at $60 < p_T < 2000/\cosh(\eta)$ GeV with shape $p_0 + p_1 \log(p_T)$.

- *PileUpPtRef* results from the propagation of the *PileUpEnvelope* uncertainty through the evaluation of the absolute-scale p_T dependence from Z/γ+jet and multijet data. This uncertainty accounts for the residual difference between the *PileUpEnvelope* and the absolute-scale fit in the range of Z/γ+jet and multijet data at $30 < p_T < 1000/\cosh(\eta)$ GeV.

- *PileUpDataMC* accounts for uncertainty in the offset scale factor for data, based on variation of the $\langle\rho\rangle$ working point within one standard deviation of the ρ distribution.

- *PileUpMuZero* is evaluated from the nominal result of the fit for η- and p_T-dependent data-based corrections, and accounts for the bias that results from deriving them at $\langle\mu\rangle \approx 20$ instead of $\langle\mu\rangle \approx 0$. This uncertainty is to be used for zero-pileup data ($\langle\mu\rangle \approx 0$, e.g., in the 2.76 TeV data collected in 2013) and replaces *PileUpPtEta*, *PileUpPtRef* and *PileUpDataMC*.

The pileup offset correction uncertainties are summarized in figure 8. The dominant uncertainty is from the residual jet p_T dependency remaining after the application of the data-based methods. It is at the level of 1% for $p_T = 30$ GeV, and rapidly decreases to the 10^{-3} level in the range constrained by the data-based methods. There is a small increase in uncertainty again at high p_T outside the range of data-based methods, where the constrained parameterizations used for data-based residuals result in a small seesaw effect. The uncertainty for $\langle\mu\rangle = 0$ data is in many cases similar or even larger than for $\langle\mu\rangle = 20$, owing to the absorption of the residual offset into relative η and absolute p_T corrections at $p_T > 30$ GeV.

2017 JINST 12 P02014

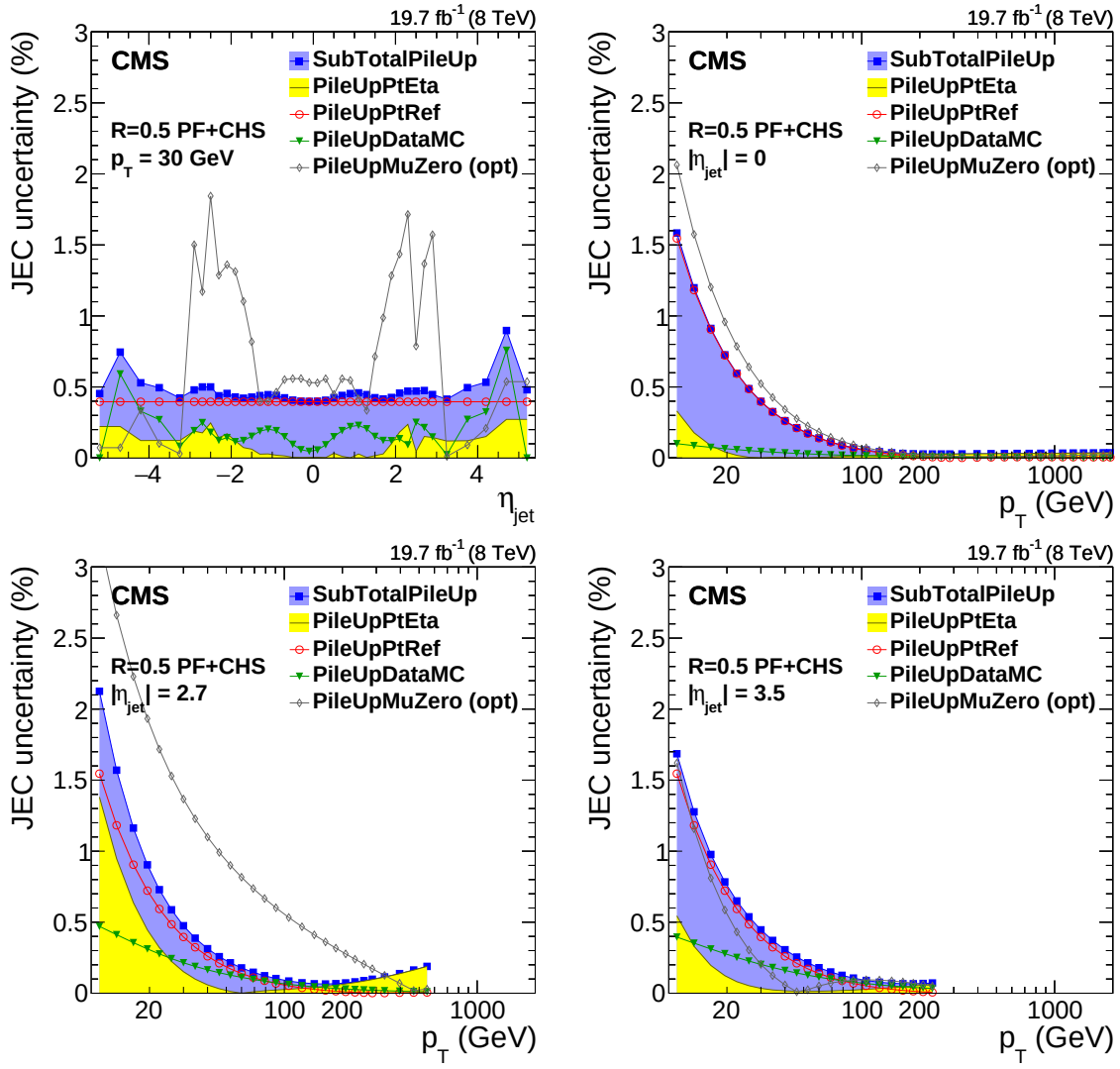

Figure 8. Pileup offset correction uncertainties for the average 2012 (8 TeV) conditions for PF jets with CHS and $R = 0.5$ as a function of η_{jet} for fixed $p_{\text{T}} = 30\,\text{GeV}$ (top left) and as a function of jet p_{T} (top right, and bottom panels). The plots are limited to a jet energy $E = p_{\text{T}} \cosh\eta = 4000\,\text{GeV}$ so as to show only uncertainties for reasonable p_{T} in the considered data-taking period. *PileUpMuZero* is an optional alternative uncertainty for zero-pileup ($\langle\mu\rangle \approx 0$) events, and it is therefore not included in the quadratic sum *SubTotalPileUp*. It accounts for the pileup uncertainty absorbed in the residual response corrections at $\langle\mu\rangle \approx 20$, which is particularly prominent at $1.5 < |\eta| < 3$.

4.5 Summary of pileup offset corrections

The pileup offset corrections for the anti-k_{T} algorithm ($R = 0.5$) with and without charged-hadron subtraction are summarized in figure 9 for typical 2012 (8 TeV) conditions of $\langle\mu\rangle \approx 20$, compared to corrections for 7 TeV data taken in 2010 and 2011. The average pileup per interaction for $R = 0.5$ is about 0.5 GeV, adding up to a total of about 10 GeV per jet. This results in a typical offset correction of about 0.75 for a $p_{\text{T,corr}} = 30\,\text{GeV}$ ($p_{\text{T,uncorr}} = 40\,\text{GeV}$) jet. The CHS removes approximately half of this offset before jet clustering by matching tracks to pileup vertices, reducing the residual offset

2017 JINST 12 P02014

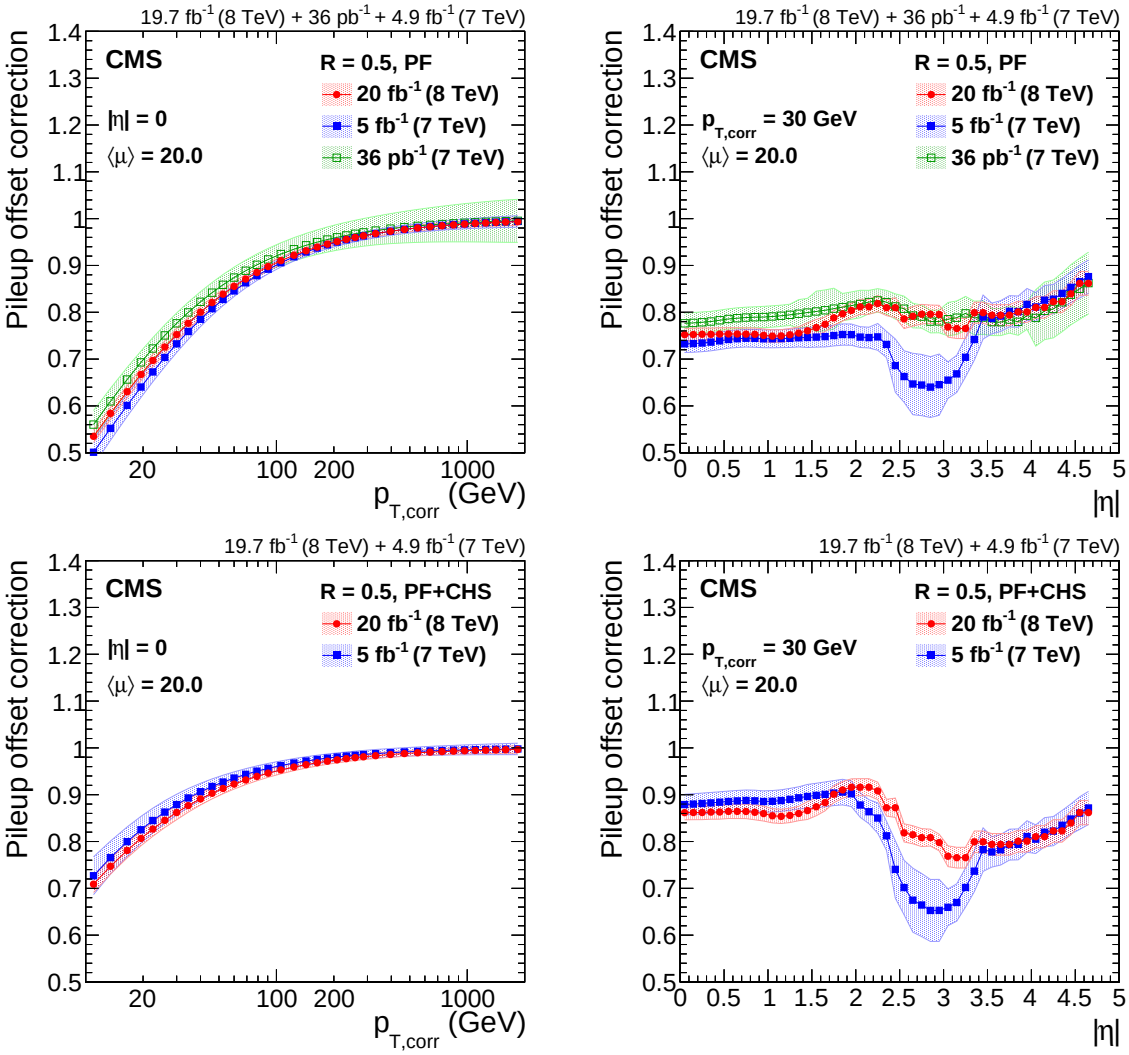

Figure 9. Pileup offset correction C_{hybrid} including data/MC scale factors, with systematic uncertainty band, for the average 2012 (8 TeV) conditions of $\langle\mu\rangle = 20$ for PF jets without CHS and $R = 0.5$ at $|\eta| = 0$ versus $p_{\text{T,corr}}$ (top left), and at $p_{\text{T,corr}} = 30\,\text{GeV}$ versus $|\eta|$ (top right), compared to corrections for 2010 [13] and 2011 [46] data at 7 TeV after extrapolation to similar pileup conditions. The same results are also shown for PF jets with CHS and $R = 0.5$ at $|\eta| = 0$ versus p_{T} (bottom left), and at $p_{\text{T,corr}} = 30\,\text{GeV}$ versus $|\eta|$ (bottom right), compared to corrections for 2011 data at 7 TeV [46].

correction to about 0.85 at $p_{\text{T,corr}} = 30\,\text{GeV}$ ($p_{\text{T,uncorr}} = 35\,\text{GeV}$). Roughly one third of the remaining pileup is from PF charged hadrons that have not been matched to good pileup vertices, and much of the rest is from PF photons. The CHS algorithm was only fully commissioned at 7 TeV in 2011, and the 2010 (7 TeV) version of the offset corrections did not yet take into account the remaining unmatched pileup tracks. Therefore only results without CHS are shown for 7 TeV in 2010.

The pileup offset corrections have been relatively stable over time at 7 TeV in 2010 and 2011, when scaled to similar pileup conditions. This is in part due to the good linearity of the offset corrections for PF and continuous development on the detector side to reduce OOT PU in the calorimeters, and in part due to the adaptability of the jet area method to the prevailing pileup offset.

The largest differences are visible in the $2.5 < |\eta| < 3.0$ region, where OOT PU increased at 7 TeV in 2011, but was again brought down in ECAL at 8 TeV in 2012 using more advanced reconstruction algorithms. The OOT PU is also partially responsible for the 2011–2012 differences in the endcaps within tracker coverage of $1.5 < |\eta| < 2.5$, and for differences between 2010 and 2011–2012 in the barrel at $|\eta| < 1.5$. In addition, the JEC were improved at 7 TeV in 2011 to take into account the difference between the offset outside jets (RC offset) and inside jets (particle-level offset). This increased the offset correction inside the tracker coverage (failed zero-suppression), and lowered it outside (calorimeter response nonlinearity), compared to the 2010 (7 TeV) corrections.

The pileup uncertainties have been steadily reduced despite rapidly increasing pileup. This can be credited to improvements in the correction methods, more events at high pileup to determine the trends versus pileup, and a reduction of double counting. The 2012 (8 TeV) corrections explicitly take into account the additional constraints from data-based methods, which reduce the offset uncertainty in the endcaps by up to 50% for PF+CHS at $p_{\mathrm{T,corr}} = 30\,\mathrm{GeV}$ compared to 7 TeV in 2011. The dominant systematic uncertainty is from the p_{T} dependence of the pileup offset, which is only indirectly constrained by data.

5 Simulated response corrections

The simulated response corrections are derived and applied on jets that have been corrected for pileup offset. The CMS detector simulation contains a detailed model of the detector geometry, data-based alignment and calibration of the detector elements, and emulation of the readout electronics. It is based upon the GEANT4 package [18] that simulates the evolution of the electromagnetic (EM) and hadronic showers and their interactions with the detector material. In addition, the PYTHIA 6.4 tune Z2* event generator is used to simulate the fragmentation of the initial quarks and gluons. Together these two components provide an accurate and detailed description of the jet response, which is used for the bulk of the JEC. Data-based methods (section 6) are needed only for small residual corrections on top of the simulated response and the simulated offset corrections discussed in section 4.

The benefit of relying heavily on simulation to derive the jet response is that we are not sensitive to many of the biases inherent in the data-based methods and can cover corners of phase space that are not easily accessible in data. This includes samples of jets with very low ($p_{\mathrm{T}} < 30\,\mathrm{GeV}$) and very high ($p_{\mathrm{T}} > 1\,\mathrm{TeV}$) momenta, heavy-flavor jets, and samples with particularly low ($\mu < 5$) and high ($\mu > 40$) pileup. Describing jet response in terms of variables accessible in simulation also facilitates the understanding of data-based methods, as we can better model the correlation between various samples and corrections. For the following discussion, jets are assumed to be corrected for the pileup offset as described in section 4.

Sample definitions

We derive the simulated response from a QCD multijet sample of 10 million events generated with PYTHIA 6.4 tune Z2*. To ensure event generation with efficient coverage of the full kinematic phase space at the LHC with small statistical uncertainty, the events are generated with a flat p_{T} spectrum and reweighted by $\hat{p}_{\mathrm{T}}^{-4.5}$, where $\hat{p}_{\mathrm{T}}$ is the transverse momentum of the generated $2 \to 2$ hard process, which allows the recovery of the original p_{T} spectrum in PYTHIA 6.4 and the production of unbiased results for $p_{\mathrm{T,\,jet}} > 30\,\mathrm{GeV}$. The generated and simulated events are overlaid with pileup generated

2017 JINST 12 P02014

by PYTHIA 6.4 tune Z2*, with events reweighted such that the pileup distribution matches that found in data.

To estimate pileup offset in jets, we simulate the same generated events also without additional pileup overlay, as was discussed in section 4. To estimate the jet response dependence on the fragmentation model and jet flavor, a complementary sample is produced with HERWIG++ 2.3 tune EE3C. To estimate the jet response dependence on the detector calibration, we also produce additional samples with the CMS fast simulation.

Definition of simulated particle response

A particle-level jet is matched to the closest reconstructed jet if it is within half of the jet distance parameter R. For a distance parameter of $R = 0.5$ this corresponds to 0.25. The method ensures a high matching efficiency (reaching 100% around $p_T = 30\,\text{GeV}$) and provides a unique match for the anti-k_T jets. In the present paper, the simulated particle response R_{ptcl} is defined as the ratio of arithmetic means of matched reconstructed and particle-level jets transverse momenta,

$$R_{\text{ptcl}}(\langle p_T \rangle, \eta) = \frac{\langle p_T \rangle}{\langle p_{T,\,\text{ptcl}} \rangle}[p_{T,\,\text{ptcl}}, \eta], \tag{5.1}$$

in bins of particle-level p_T ($p_{T,\,\text{ptcl}}$) and reconstructed η (where p_T is the transverse momentum of the reconstructed jet). As in the previous sections, the square brackets [ ] denote the binning variables, and the angle brackets $\langle\ \rangle$ indicate the averages within those bins for the variables that are used to parameterize the response.

5.1 Corrections versus η and p_T

Simulated anti-k_T jets, with a distance parameter $R = 0.5$, are used to study the detector response as a function of the jet p_T. The simulated particle response is shown in figure 10 (left) as a function of the reconstructed jet η. The simulated particle response after JEC is shown in figure 10 (right) as a function of the particle-level jet $p_{T,\,\text{ptcl}}$ in various η regions. The results show that the response is corrected to within 0.5% with respect to the particle-level jet, for p_T from about 20 GeV to 2 TeV.

5.2 Dependence on the jet size

The dependence of the jet response on the jet distance parameter R has been checked in the range $R = 0.3$–1.0. The response is similar after accounting for the increasing PU offset due to the larger jet area ($A_{\text{jet}} \approx \pi R^2$). Smaller effects come primarily from two sources:

- The UE energy within the jet has lower response than the energy from the hard scattering, lowering the response at low p_T for jets with large R.
- A larger distance parameter averages the jet response over a larger area, smearing sharp features in the detector response versus η.

Figure 11 (left) shows the comparison of the JEC factor for various jet sizes at $p_T = 30\,\text{GeV}$. As expected from the larger fraction of UE energy, the corrections rise slightly for larger distance parameters. The very small distance parameter $R = 0.3$ is an exception to this rule, because the detector granularity smears some energy out of the cone. These differences mostly disappear

2017 JINST 12 P02014

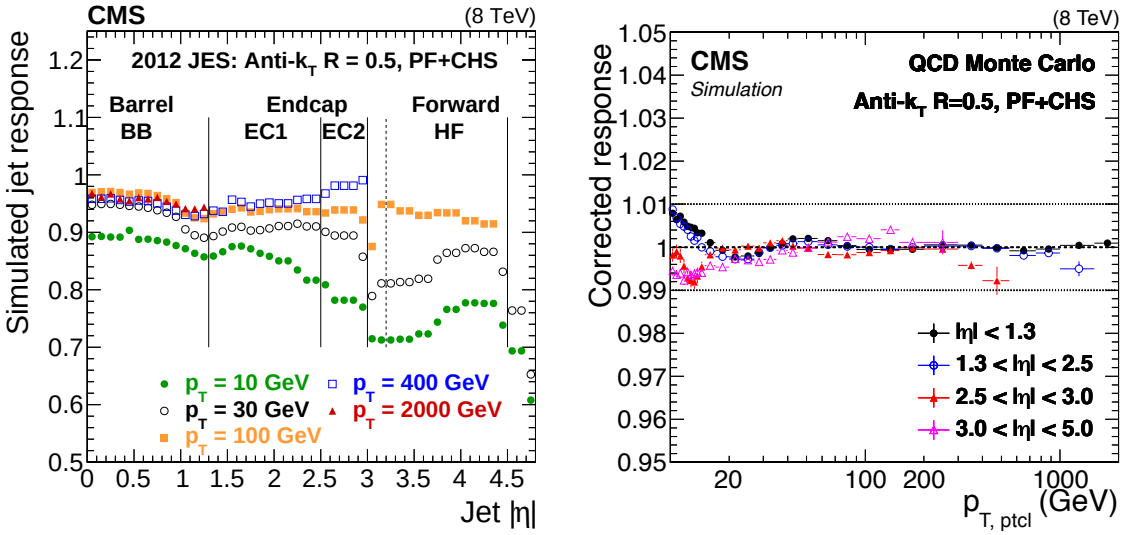

Figure 10. Simulated jet response R_{ptcl} versus $|\eta|$ for $R = 0.5$ (left). Simulated jet response R_{ptcl}, after JEC have been applied, versus $p_{\text{T, ptcl}}$ for $R = 0.5$ in various η regions, and with statistical uncertainties (right).

at higher p_{T} for $R \geq 0.4$, with the smaller jet sizes showing slightly sharper detector features. Simulated jet responses after the application of the JEC are shown in figure 11 (right) as a function of jet p_{T} for a range of distance parameters from 0.3 to 1. The response is consistent with unity within 1% for $p_{\text{T}} \gtrsim 30\,\text{GeV}$. During Run 1 of the LHC, the supported jet size parameters in pp collisions were $R = 0.5$ and $R = 0.7$. The full jet energy corrections and uncertainties were derived and provided centrally only for these two jet size parameters.

5.3 Detector simulation uncertainties

We evaluate several systematic uncertainties using simulation, with the uncertainties further constrained using data-based methods, as discussed later. We discuss here the uncertainties arising from the propagation of detector calibration uncertainties to the jet response. The effects of jet fragmentation and flavor response are discussed in section 7.3. Because the jet response is later constrained using measurements based on data, these systematics are explicitly set to zero at certain reference points, discussed in section 6. They are then used to extrapolate the systematics from these reference points to regions of the phase space not directly calibrated with data.

Single-pion response. The jet response is sensitive to the underlying detector calibrations. The CMS calorimeters have been calibrated in test beam studies, and the single-pion response (SPR) has subsequently been checked on proton-proton data with charged pions [47], confirming good modeling of the barrel response in simulation to within ±3%. Because the PF reconstruction relies heavily on tracking for low-p_{T} jets, the sensitivity to the detector calibration is strongly reduced compared to the calorimeter-only reconstruction. To show this effect, the ratio of the response when varying the SPR with respect to the nominal response is shown in figure 12, for jets reconstructed with the PF algorithm and for jets reconstructed with only calorimetric energy deposits, both using the anti-k_{T} algorithm. For this study, the SPR has been propagated to the JEC using the CMS fast simulation.

2017 JINST 12 P02014

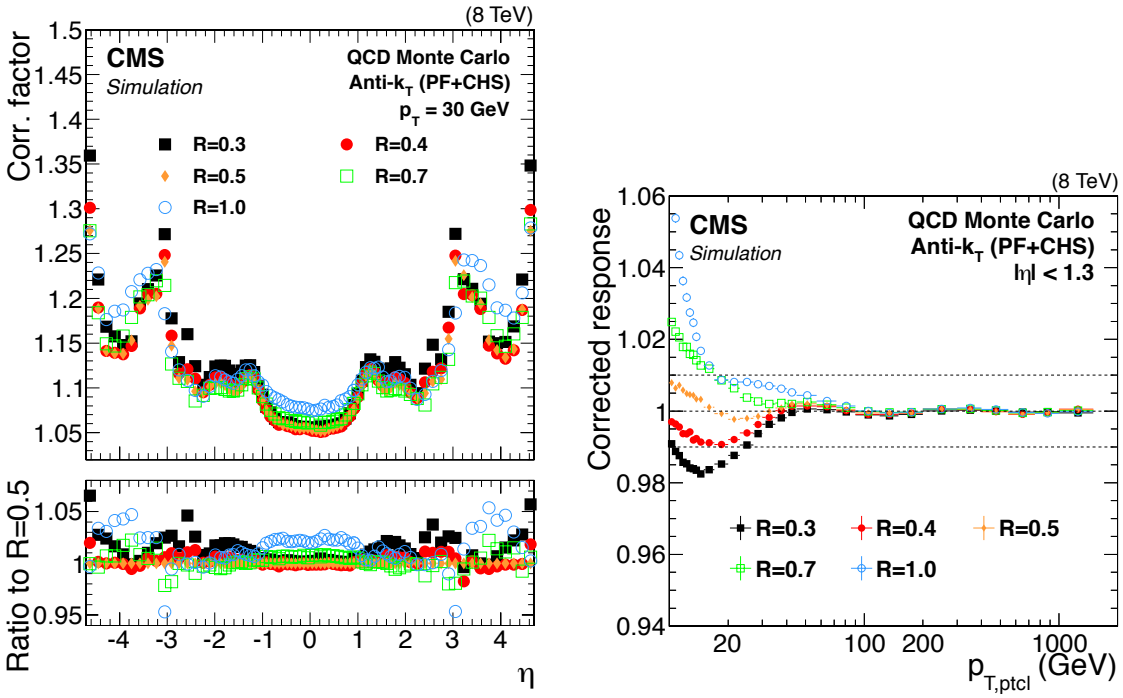

Figure 11. Jet energy correction factors for a jet with $p_T = 30$ GeV, as a function of η and for various jet sizes R (left). Simulated jet energy response R_{ptcl} after JEC for $|\eta| < 1.3$ as a function of the particle-level jet p_T for various jet sizes R (right).

At low p_T, PF is directly sensitive to SPR only through neutral hadrons, which on average contribute 15% of the jet energy at particle level, leading to a sensitivity of about 0.5% for a simultaneous change of ±3% in both ECAL and HCAL SPR. At high p_T the PF performance approaches that of the calorimetric reconstruction, because the tracking efficiency drops in the dense jet core and the leading tracks become too straight for a reliable p_T measurement. Since 25% of the jet energy is deposited as photons (section 10), the JEC sensitivity to a ±3% change in SPR is at most 2.3%. The sensitivity to changes in SPR has been also studied separately for a 3% change in the response of the ECAL and HCAL, as shown in figure 13. The results are qualitatively similar to an overall change in SPR, but show larger sensitivity to the SPR in HCAL at high p_T. This is because hadronic showers become deeper for high-p_T particles, and deposit a larger fraction of their energy in the HCAL.

5.4 Jet energy corrections propagation to missing transverse momentum

The jet energy corrections are propagated to $\vec{p}_T^{\,miss}$ by using the so-called type-I correction:

$$\vec{p}^{\,miss}_{T,typeI} = \vec{p}^{\,miss}_{T,uncorr} + \sum_i \vec{p}^{\,i}_{T,uncorr} - \sum_i \vec{p}^{\,i}_{T,corr} - \sum_i \vec{O}^{\,i}_{RC}, \tag{5.2}$$

where $\vec{p}^{\,miss}_{T,uncorr}$ is the uncorrected $\vec{p}_T^{\,miss}$, $\vec{p}_{T,uncorr}$ is the uncorrected jet p_T, $\vec{p}_{T,corr}$ is the fully corrected jet p_T, and $\vec{O}^{\,i}_{RC}$ is the average offset due to pileup, as obtained with the RC method (see section 4.3). The sum runs over all jets with $p_{T,corr} > 10$ GeV in the event. Including the average RC offset underneath jets in the missing transverse momentum vector sum ensures that the pileup

2017 JINST 12 P02014

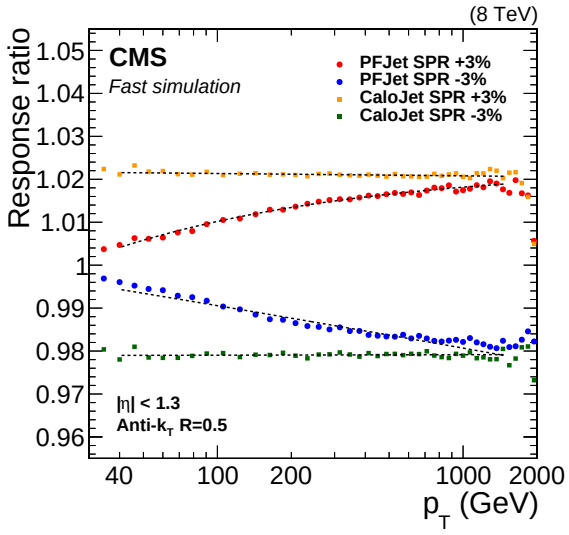

Figure 12. Changes in PF jet and calorimeter jet response resulting from ±3% variations of single-pion response in parameterized fast simulation in HCAL+ECAL.

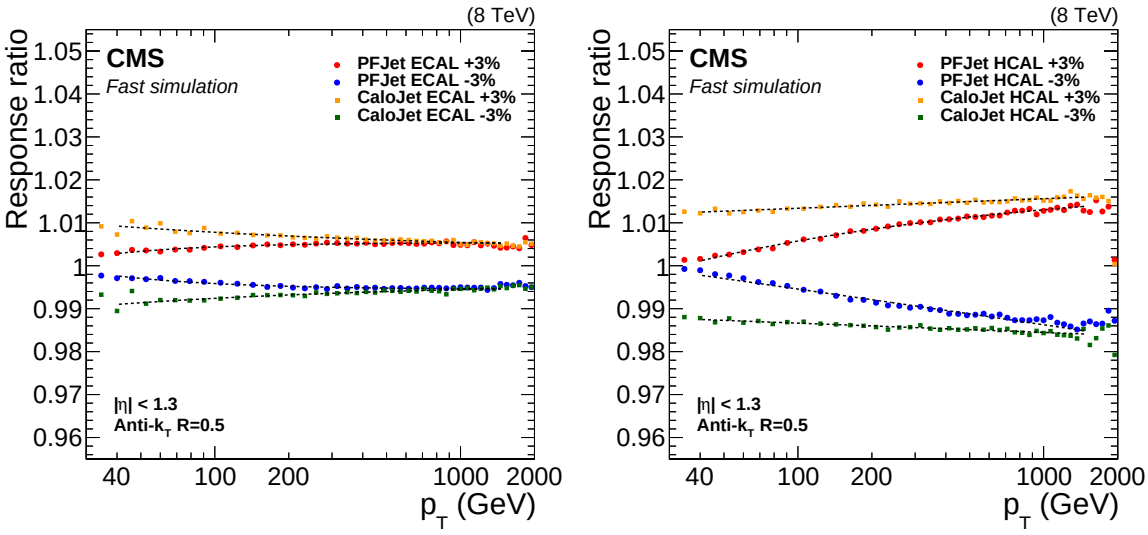

Figure 13. Changes in PF jet and calorimeter jet response resulting from ±3% variations of single-pion response in parameterized fast simulation in ECAL (left), and HCAL (right).

offset remains isotropic and does not bias $\vec{p}_{\mathrm{T}}^{\,\mathrm{miss}}$. The type-I correction is recommended for physics analyses and is used in most CMS results, as well as for deriving residual JEC for data.

5.5 Summary of simulated response corrections

The simulated particle response corrections are summarized in figure 14 for data collected at 8 TeV and compared to corrections for 7 TeV data taken in 2010 and 2011. At low p_{T}, the JEC rise toward 1.15 due to the 15% neutral hadron energy that largely falls below calorimeter thresholds. The response is quite flat at $p_{\mathrm{T}} > 50$ GeV, where the competing effects of increasing calorimeter

2017 JINST 12 P02014

response and falling tracking efficiency within the jet core compensate each other. In the barrel and endcap regions, the corrections rise with $|\eta|$, due to the increasing amount of material located in front of the calorimeters, which leads to effects such as an increased rate of nuclear interactions in the tracker. The corrections are higher around $|\eta| = 1.3$ and 3.0 due to the degradation of the response in the transition regions.

Significant improvements in the simulation occurred after the first year of running at 7 TeV in 2010, when in situ collision data became available for tuning the detector simulation. After that, the simulated particle response corrections have been stable in 2011–2012 despite continuous development of the reconstruction software, and the changes have remained within the steadily-reducing systematic uncertainties. The differences introduced by the change in $\sqrt{s}$ are practically negligible.

6 Residual corrections for data

The residual data/simulation scale factors for JEC are determined after correcting jets for pileup and simulated particle response. For consistency, the variations of the jet momenta due to corrections for pileup and simulated response are propagated to the $\vec{p}_{\mathrm{T}}^{\,\mathrm{miss}}$ definition *à la* eq. (5.2). The residual corrections for data are first determined with a sample of dijet events with low statistical uncertainty, where the response of jets over a wide range of p_{T} is corrected relative to the one of jets with $|\eta| < 1.3$, and then with a combination of $\mathrm{Z}(\rightarrow \mu\mu)$+jet, $\mathrm{Z}(\rightarrow \mathrm{ee})$+jet, γ+jet, and multijet events for jets with $|\eta| < 1.3$ from a p_{T} of around 30 GeV to 1 TeV. The basic idea, in all the considered topologies, is to exploit the transverse momentum balance, at hard-scattering level, between the jet to be calibrated and a reference object: a jet energy scale different from unity generates imbalance at the reconstructed level.

The jet energy response is studied using the p_{T} balance and MPF (missing transverse momentum projection fraction) methods [13]. While in the p_{T}-balance method the jet response is evaluated by comparing the reconstructed jet momentum ($p_{\mathrm{T,\,jet}}$) directly to the momentum of the reference object ($p_{\mathrm{T,ref}}$), the MPF method considers the response of the whole hadronic activity in the event, recoiling versus the reference object. This leads to the following definition of response for the two methods:

$$R_{\mathrm{jet},p_{\mathrm{T}}} = \frac{p_{\mathrm{T,\,jet}}}{p_{\mathrm{T,ref}}}, \tag{6.1}$$

$$R_{\mathrm{jet,MPF}} = 1 + \frac{\vec{p}_{\mathrm{T}}^{\,\mathrm{miss}} \cdot \vec{p}_{\mathrm{T,ref}}}{(p_{\mathrm{T,ref}})^2}. \tag{6.2}$$

The difference and complementarity of the two response determinations will be studied in the following sections.

Part of the transverse momentum imbalance between the jet to be calibrated and the reference object can also come from the presence of additional jets in the event; this effect depends on the studied topology and is not correlated with the jet energy response. For this reason, all the corrections are studied as a function of the additional jet activity in the event, quantified by the variable α. This is defined as the ratio of the most energetic jet that does not originate from the event topology under study, divided by the typical momentum scale of the event. In other words $\alpha = p_{\mathrm{T,\,3rd\,jet}}/p_{\mathrm{T,ave}}$ for dijet events and $\alpha = p_{\mathrm{T,\,2nd\,jet}}/p_{\mathrm{T},\gamma/\mathrm{Z}}$ for Z+jet and γ+jet events. The corrections are then extrapolated to the value they would have for $\alpha = 0$ in order to address only genuine jet energy response effects.

2017 JINST 12 P02014

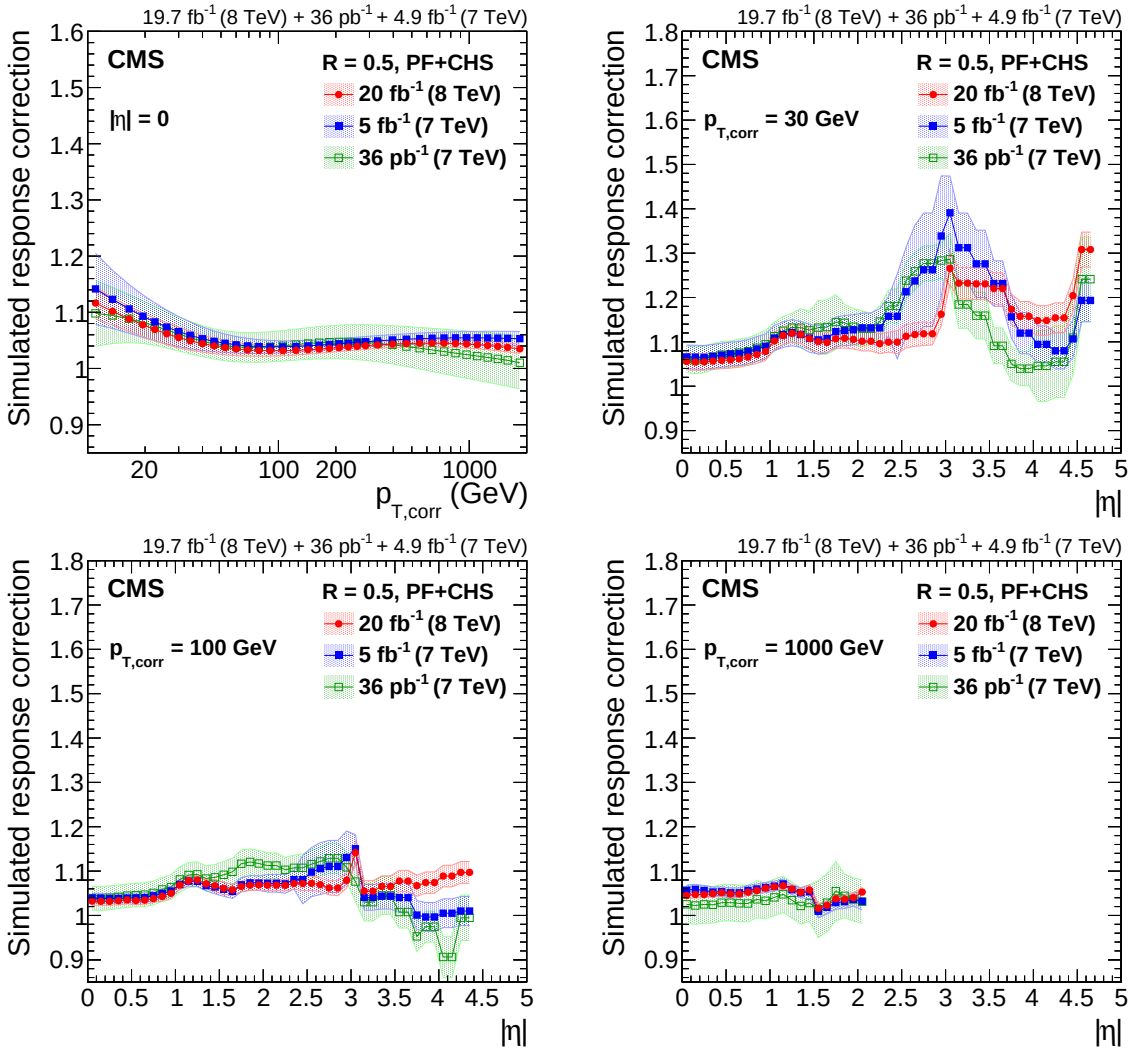

Figure 14. Response correction factors with their systematic uncertainty band from simulation for the 2012 data collected at 8 TeV for PF jets with CHS and $R = 0.5$, compared to corrections at 7 TeV corresponding to 36 pb^{-1} of data taken in 2010 [13] and 5 fb^{-1} taken in 2011 [46]. The comparison is shown at $|\eta| = 0$ versus $p_{\mathrm{T,corr}}$ (top left), and as a function of $|\eta|$ at $p_{\mathrm{T,corr}} = 30$ GeV (top right), $p_{\mathrm{T,corr}} = 100$ GeV (bottom left) and $p_{\mathrm{T,corr}} = 1000$ GeV (bottom right). The plots are limited to a jet energy $E = p_{\mathrm{T}} \cosh \eta = 3500$ GeV so as to show only the correction factors for reasonable p_{T} in the considered data-taking periods.

6.1 Relative η-dependent corrections

Residual η-dependent corrections to the jet response are obtained using dijet events, where the “tag" jet has $|\eta| < 1.3$, and the “probe" jet pseudorapidity is unconstrained. In this way, the response for all jets is corrected relative to the response for central jets ($|\eta| < 1.3$). These residual corrections are derived from jets already corrected with the simulation-based corrections and account for any residual difference between data and simulation, as a function of both η and p_{T}.

For dijet events, where the reference object (barrel jet) has poor resolution, the biases from JER are minimized by binning in average jet p_{T} instead of $p_{\mathrm{T,tag}}$: $p_{\mathrm{T,ave}} = 0.5(p_{\mathrm{T,tag}} + p_{\mathrm{T,probe}})$.

This symmetric p_T binning also cancels out to first order the relative biases from ISR+FSR. In general, $\langle y/x \rangle \neq \langle y \rangle / \langle x \rangle$, unless x is constant, which is generally the case only for a sufficiently narrow bin in x. To avoid biases in the ratio variables, the denominator must therefore also use $p_{T,ave}$. This leads to the following definitions for p_T balance and MPF in dijet events:

$$R_{rel}^{p_T} = \frac{1 + \langle \mathcal{A} \rangle}{1 - \langle \mathcal{A} \rangle}, \quad \text{where} \tag{6.3}$$

$$\mathcal{A} = \frac{p_{T,\,probe} - p_{T,\,tag}}{2p_{T,\,ave}}, \quad \text{and} \tag{6.4}$$

$$R_{rel}^{MPF} = \frac{1 + \langle \mathcal{B} \rangle}{1 - \langle \mathcal{B} \rangle}, \quad \text{where} \tag{6.5}$$

$$\mathcal{B} = \frac{\vec{p}_T^{\,miss} \cdot (\vec{p}_{T,\,tag}/p_{T,\,tag})}{2p_{T,\,ave}}. \tag{6.6}$$

With sufficiently fine binning in $p_{T,\,ave}$, and by extrapolating the additional jet activity, not coming from the leading jet, to zero with $\alpha = p_{T,\,3rd\,jet}/p_{T,\,ave}$, both variables $R_{rel}^{p_T}$ and R_{rel}^{MPF} reduce to $R_{rel} = \langle p_{T,\,probe} \rangle / \langle p_{T,\,tag} \rangle$. Under the assumption that $\langle p_{T,\,probe,\,ptcl} \rangle = \langle p_{T,\,tag,\,ptcl} \rangle$, which is true after correcting for the various small second-order biases from JER and ISR+FSR, this is equivalent to the ratio of the jet responses for the tag and probe jets such that $R_{rel} = R_{jet,\,probe}/R_{jet,\,tag}$. The residual η-dependent corrections are based on results obtained with the MPF method, the p_T balance results are used as a crosscheck.

As shown in figure 15, the relative η- and p_T-dependent correction $R_{rel,MC}/R_{rel,data}$ varies between 0.99 and 1.01 in the barrel at $|\eta| < 1.3$, between 0.99 and 1.06 at $1.3 < |\eta| < 2.9$, and increases to 1.15 in HF. Some p_T dependence is observed in the endcaps relative to the barrel, with the residual corrections approaching unity at high p_T, where nonlinearities in calorimeter response are reduced. In the following we will review the corrections for ISR+FSR, JER, and jet p_T dependence, as well as the associated uncertainties for the η-dependent corrections.

Initial- and final-state radiation correction. For central-forward jet pairs there is a higher probability for the ISR to be radiated opposite to the central jet, and the FSR activity may differ slightly for the jets at different η, which leads to some residual dependence of the measured value of the p_T-balance or MPF response, R_{rel}, on additional jet activity α. We evaluate this dependence in bins of η, for the linearly extrapolated $\alpha \to 0$ and $\alpha < 0.2$ respectively, and compute the following data/simulation double ratio:

$$k_{FSR}(\alpha = 0.2) = \left(\frac{R_{rel}^{data}(\alpha \to 0)}{R_{rel}^{MC}(\alpha \to 0)} \right) \Big/ \left(\frac{R_{rel}^{data}(\alpha < 0.2)}{R_{rel}^{MC}(\alpha < 0.2)} \right). \tag{6.7}$$

The correction factor k_{FSR} (we use the subscript FSR instead of ISR+FSR for brevity) is determined separately for the MPF and p_T-balance methods and for PYTHIA 6.4 and HERWIG++ 2.3, as shown in figure 16, and is then parameterized versus $|\eta|$ with the same functional form as in ref. [13]. The differences between PYTHIA 6.4 and HERWIG++ 2.3 for the p_T-balance method are up to 6% at $|\eta| < 5.2$ prior to the application of ISR+FSR corrections, as seen in figure 16 (left). Both agree well after the ISR+FSR correction, as shown in figure 16 (right), but the MPF method is much less sensitive to ISR and FSR biases than the p_T-balance method, because the entire hadronic recoil is used for the MPF balance.

2017 JINST 12 P02014

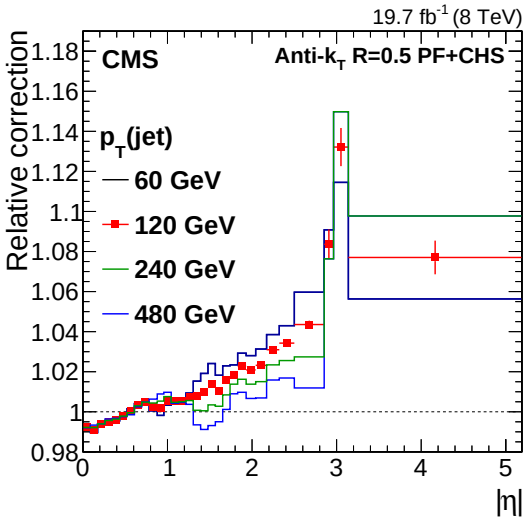

Figure 15. Relative energy scale correction for p_T = 60, 120, 240 and 480 GeV as a function of $|\eta|$. The residual corrections increase toward high rapidity and low p_T, where effects from nonlinear calorimeter response become more important. The curves are limited to a jet energy $E = p_T \cosh\eta = 4000$ GeV (corresponding to $\eta \approx 2.8$ for a jet with $p_T = 480$ GeV) so as to show only the correction factors for reasonable p_T in the considered data-taking period. The statistical uncertainty associated with a constant fit versus p_T is shown for $p_T = 120$ GeV (markers).

Resolution correction. The MPF and p_T-balance methods are both sensitive to the relative differences in JER between the jets. This bias is expected to cancel out for the data/MC ratio of R_{rel} when the jets in the simulation are smeared to match the measured resolution in data using the relation:

$$p_{T,smeared} = p_T \text{Gaussian}\left(\mu = 1, \sigma = \sqrt{k^2 - 1}\,\sigma_{MC}\right), \tag{6.8}$$

where k is the data/MC scale factor for JER determined in section 8 and σ_{MC} is the JER in the MC simulation. The factor k varies between 1.05 and 1.40 depending on η. The jet p_T is multiplied by a random number drawn from a Gaussian distribution with mean $\mu = 1$ and width σ, such that the smeared jet has the same resolution $k\sigma_{MC}$ as the jets in data. The smearing is applied on a jet-by-jet basis to all jets in the event, such that the resolution correction is propagated to the p_T-balance and MPF methods in a consistent way.

Relative correction: p_T dependence. The η-dependent corrections are studied in bins of average jet p_T, where a slight p_T dependence is observed. For this reason, the η-dependent corrections are parameterized with a log-linear p_T-dependence, according to the formula $p_0 + p_1 \log(p_T)$. The correction factor as a function of η, as obtained from the p_T-dependent fit is shown in figure 17 (left), compared to the result from a constant fit. Here, the central value is obtained from evaluating the p_T-dependent correction at the p_T value for which the constant fit and the logarithmic fit agree, $\bar{p}_T$. The blue band is obtained by varying the p_T at which the logarithmic fit is evaluated between 0.5 times and 2 times $\bar{p}_T$. The $\bar{p}_T$ is typically close to the mean p_T of the dijet samples, and is shown in figure 17 (right). The p_T-dependent fit is used as the central result over the whole η range, with the exception of the HF ($|\eta| > 3$). For this region, to mitigate the effect of statistical fluctuations

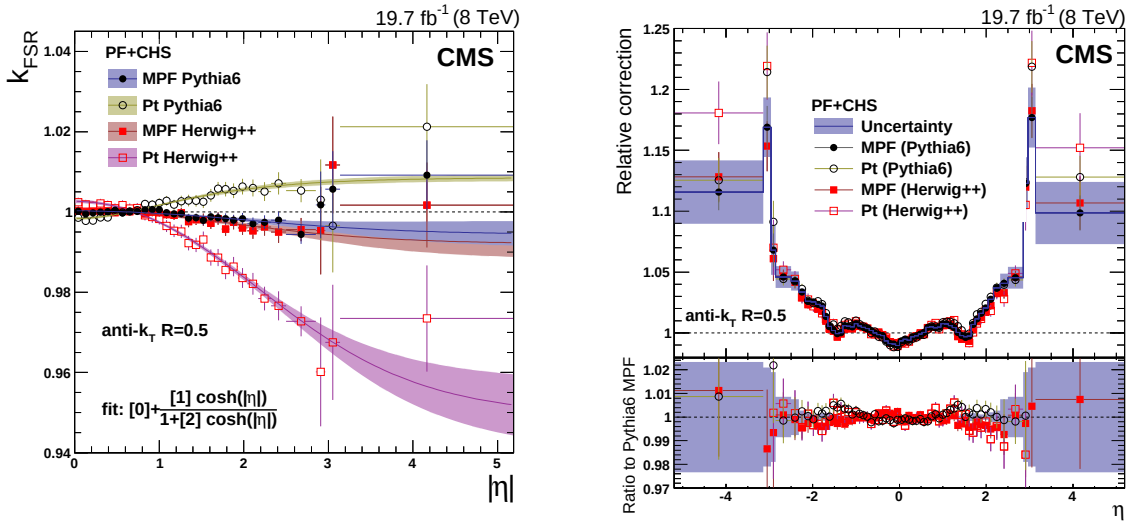

Figure 16. The $k_{\mathrm{FSR}}(\alpha = 0.2)$ correction factor (defined in eq. (6.7)) plotted vs. $|\eta|$ (left). This ratio is used for ISR+FSR corrections that are applied to dijet events with $\alpha < 0.2$, for the MPF and p_{T}-balance methods, and for PYTHIA 6.4 tune Z2* and HERWIG++ 2.3 tune EE3C. The points are fitted with $f(\eta) = p_0 + p_1 \cosh(\eta)/(1 + p_2 \cosh(\eta))$ as in ref. [13]. Relative η corrections obtained with the MPF and balance methods and the PYTHIA 6.4 tune Z2* and HERWIG++ 2.3 tune EE3C MC generators (right). The results are shown after corrections for ISR+FSR, and compared to the central values, obtained with the MPF method and PYTHIA 6.4 tune Z2* simulated events.

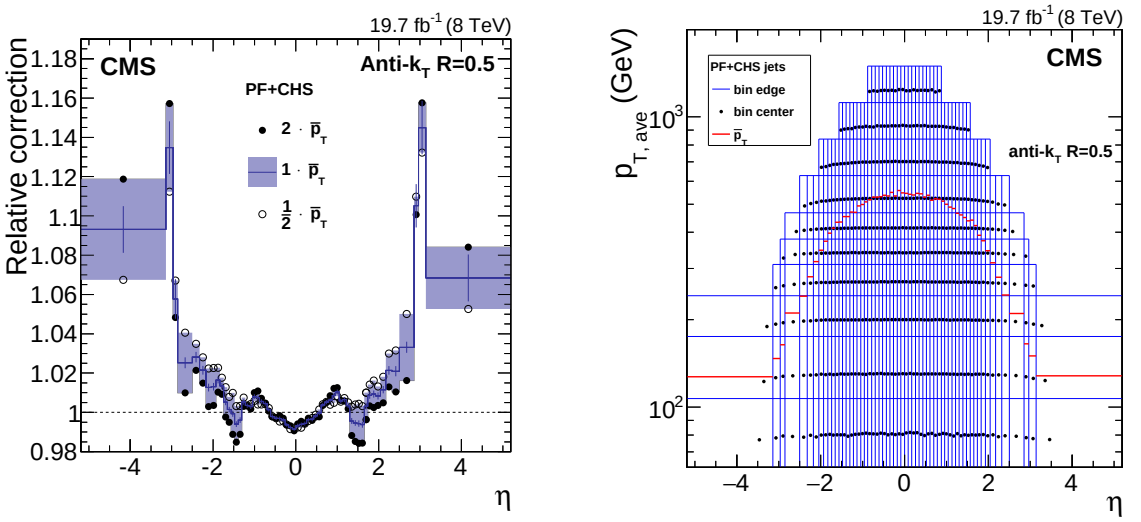

Figure 17. Relative η correction factor at the crossover $\bar{p}_{\mathrm{T}}$ (defined as the value of p_{T} where the log-linear and constant fits versus $p_{\mathrm{T,ave}}$ agree) value, and at half and twice the $\bar{p}_{\mathrm{T}}$ values (left). The statistical uncertainty in the constant fit at each value of $\bar{p}_{\mathrm{T}}$ is also shown. Distribution of the p_{T} and η bins used in the dijet balance measurement, with a point at the average p_{T} and η for each bin (right). The horizontal red lines indicate the crossover $\bar{p}_{\mathrm{T}}$ value for each bin.

(visible e.g. in figure 17 (left)), the correction is taken from the constant fit and symmetrized over positive and negative η values.

2017 JINST 12 P02014

6.2 Relative correction uncertainties

The largest uncertainties in the relative corrections arise from the following sources:

- **ISR+FSR**, ≤0.2%. The *RelativeFSR* uncertainty in k_{FSR} is estimated by using HERWIG++ 2.3 as "data" and comparing how well the different methods reproduce the ratio of particle-level simulated responses. This uncertainty increases smoothly with increasing $|\eta|$, up to 0.2% in HF.

- **Jet p_{T} resolution**, ≤1.4%. The *RelativeJER* systematic uncertainty on the JER correction is estimated by varying the data/MC scale factor k in eq. (6.8) within the uncertainties determined in section 8, which are between 2% and 20%, depending on η. This uncertainty mainly affects the η bins in the HF, where JER is poorly constrained from data.

- **Relative correction p_{T} dependence**, ≤1.4%. Half of the difference between the log-linear and constant fits observed in figure 17 is taken as a *RelativePt* systematic uncertainty to account for uncertainties coming from the choice of the log-linear shape for the fit. This is the dominant uncertainty in the barrel and endcaps.

- **Statistical uncertainty**, ≤0.9%. The number of events available in data for the η-dependent corrections is limited in the endcap and HF regions due to the large prescales applied to the dijet triggers during data taking. To estimate the impact of this on physics analyses, the corrections are symmetrized and determined in wide bins of $|\eta|$. The remaining statistical uncertainty of up to 2.5% is assigned as *RelativeStat* systematic uncertainty.

- **Time dependence**, ≤1.0%. The *TimeEta* systematic uncertainty is estimated as the RMS of the η-dependent correction factors for a set of about ten data-taking periods, chosen arbitrarily in order to have comparable integrated luminosities. The variation is assumed to come from residual scale shifts remaining after the radiation damage corrections have been applied to the ECAL and HCAL, and increases toward high rapidities, which suffer larger radiation damage.

Uncertainty correlations versus η. The *RelativeJER*, *RelativePt*, and *RelativeStat* systematic uncertainties are assumed to be correlated versus η within the barrel (*BB:* $|\eta| < 1.3$), the region of the endcap that is within tracker coverage (*EC1:* $1.3 < |\eta| < 2.5$), the region of the endcap which is outside the tracker coverage (*EC2:* $2.5 < |\eta| < 3$), and within the hadron forward calorimeter (*HF:* $3 < |\eta| < 5.2$), but not between these regions. The *RelativeStat* uncertainty is significant only in the more forward regions, and is only provided for the two latter regions (EC2 and HF, which are considered uncorrelated). All other systematic uncertainties relevant for η-dependent corrections (*RelativeFSR, TimeEta*) are considered to be fully correlated versus η. Each correlated region is treated with a separate systematic source, and these are provided separately to the users.

The systematic uncertainties in the relative η-dependent corrections are summarized in figure 18, for low (30 GeV) and medium (100 GeV) p_{T} versus η, and for the outer endcap ($\eta = 2.7$) versus p_{T}. The time-dependent uncertainties are optional for analyses that are performed on the full 2012 data and are shown separately versus η at $p_{\mathrm{T}} = 30$ GeV. Among the time-dependent systematic uncertainties only the *TimeEta* is relevant. The uncertainties are small at high p_{T} and for central rapidities within the tracker coverage. They increase to 2.1% at high rapidity mainly

2017 JINST 12 P02014

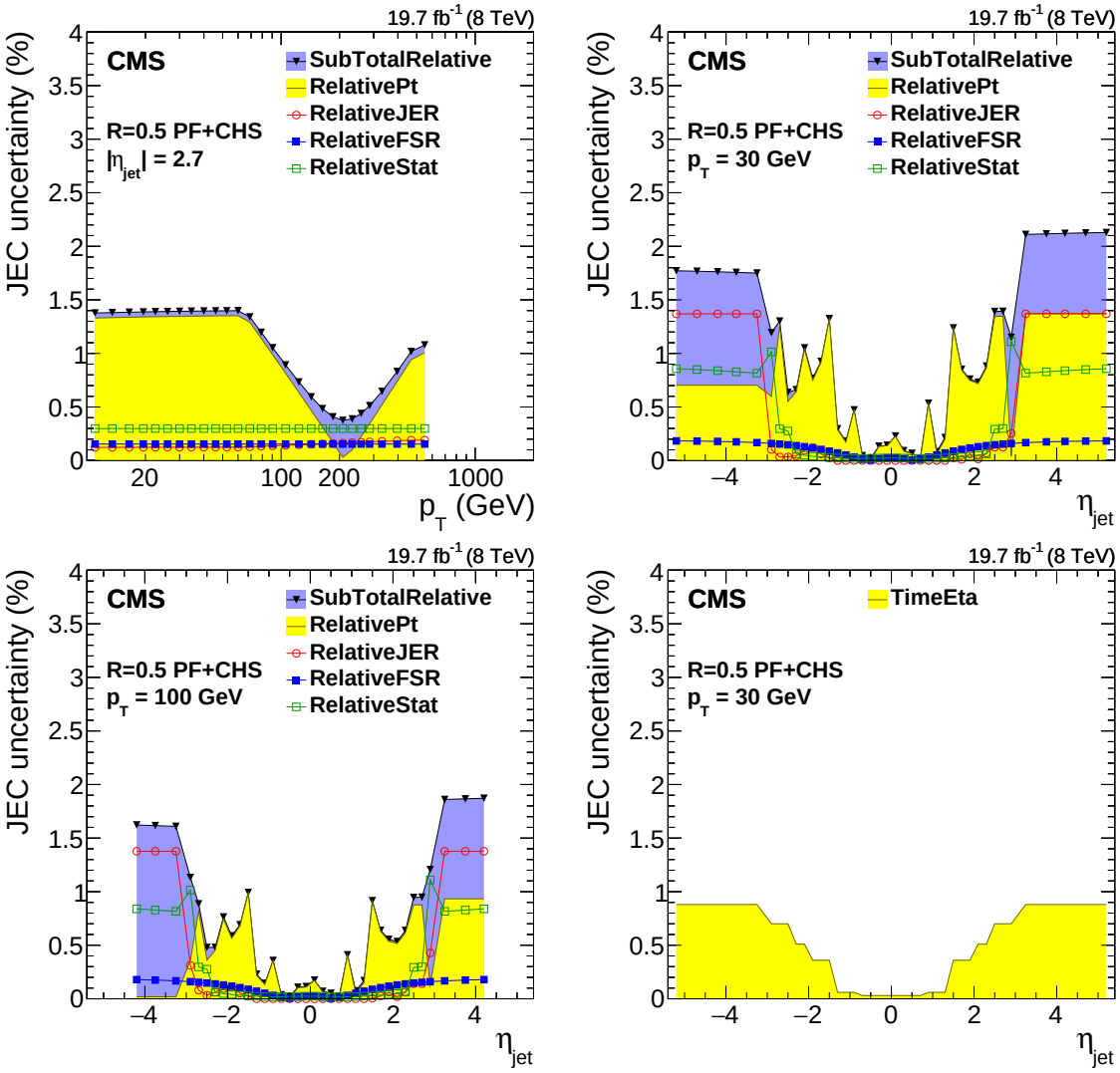

Figure 18. Systematic uncertainties for the relative η-dependent corrections as a function of jet p_T (top left) and as a function of jet η for jets with $p_T = 30\,\text{GeV}$ (top right) and for jets with $p_T = 100\,\text{GeV}$ (bottom left). Time-dependent uncertainties as a function of jet η for jets with $p_T = 30\,\text{GeV}$ (bottom right). The plots are limited to a jet energy $E = p_T \cosh\eta = 4000\,\text{GeV}$ so as to show only uncertainties for reasonable p_T in the considered data-taking period. *SubTotalRelative* is the quadratic sum of *RelativePt*, *RelativeJER*, *RelativeFSR* and *RelativeStat*.

due to the limited number of events available in the data for deriving the JEC, JER and ISR+FSR corrections. The dominant *PileUpPt* uncertainty is inherently asymmetric and has the largest visible differences in the HF region, where the asymmetric log-linear fit is compared to a symmetrized constant fit used for central value in HF. The uncertainty versus p_T changes sign around 100 GeV for the negative η side while it remains same-sign for the positive η.

6.3 Absolute corrections

The absolute JES at $|\eta| < 1.3$ is determined with Z($\to \mu\mu$)+jet, Z($\to$ ee)+jet and γ+jet events for jet p_T between 30 and 800 GeV by comparing the reconstructed p_T of the jet to that of a precisely measured object (the Z boson, or the photon). The response for jets with $p_T > 800$ GeV is constrained using multijet events, where a high-p_T jet in the barrel region is balanced by a recoil system, composed of two or more lower-p_T jets.

For all these analyses, the corrections are derived by comparing the jet energy response (with different methods) in data and simulation, using events in the central region, where jets are already corrected with the simulation-based corrections and η-dependent residual corrections. As detailed below, the response is observed to be slightly lower in data than in simulation. In addition, the ratio of data over the MC prediction of the response shows a p_T dependence. The two effects are factorized and addressed in successive steps. First, a rough estimate of the p_T independent correction is derived from the analysis of Z($\to \mu\mu$)+jet events. Second, the response and its p_T dependence are determined precisely from a global fit (described in section 6.4), with the individual response values obtained from the different channels (Z($\to \mu\mu$)+jet, Z($\to$ ee)+jet, γ+jet, multijet) as input.

Methods. The absolute jet response is measured relative to a photon or Z boson momentum scale, using the p_T-balance (R_{jet,p_T}) and MPF ($R_{\text{jet,MPF}}$) methods [13], as defined in eqs. (6.1) and (6.2), with $p_{T,\text{ ref}} = p_{T,\gamma/Z}$. The measurements are affected by biases from ISR+FSR, underlying event (UE) and out-of-cone (OOC) showering. To correct for the FSR+ISR bias, we define a k_{FSR} correction as follows:

$$k_{\text{FSR}}(\alpha) = \frac{R_{\text{jet}}(\alpha \to 0)}{R_{\text{jet}}(\alpha)}, \quad \alpha = \frac{p_{T,\text{2nd jet}}}{p_{T,\gamma/Z}}, \tag{6.9}$$

where the jet response R_{jet} is measured with the MPF or the p_T-balance method, with separate corrections for each. As shown in figure 19, the value of $k_{\text{FSR}}(\alpha)$ is linearly dependent on α for $0.05 < \alpha < 0.3$. Because the average p_T of the Z boson decreases with α, the particle-level jet response obtained from simulation also shows a dependence on α. Figure 19 demonstrates that the MPF method is significantly less sensitive to ISR+FSR and the modeling of these processes, than the p_T-balance method: the slope $\Delta R_{\text{jet}}/\Delta\alpha$ is about -0.3 for the p_T-balance method and $+0.06$ for the MPF method. For the data/MC ratio these slopes are further reduced by an order of magnitude, confirming a good modeling of the OOC and UE effects. It can be shown that the ratio of MPF and p_T-balance slopes versus α is

$$\frac{\mathrm{d}R_{\text{jet,MPF}}/\mathrm{d}\alpha}{\mathrm{d}R_{\text{jet},p_T}/\mathrm{d}\alpha} = 1 - \frac{R_{\text{FSR+ISR jets}}}{R_{\text{jet}}}. \tag{6.10}$$

The difference in jet response between the leading jet and the ISR+FSR jets is typically less than 20%, as seen in figure 14, but the sign can be either positive or negative. The slope of k_{FSR} has some dependence on the jet flavor (gluons radiate more than quarks) and it depends, e.g., on the parton shower model used in the MC simulation. As shown in section 6.4, determining k_{FSR} in narrow bins of $p_{T,\text{ref}}$ is needed in order to study the p_T dependence of the JES.

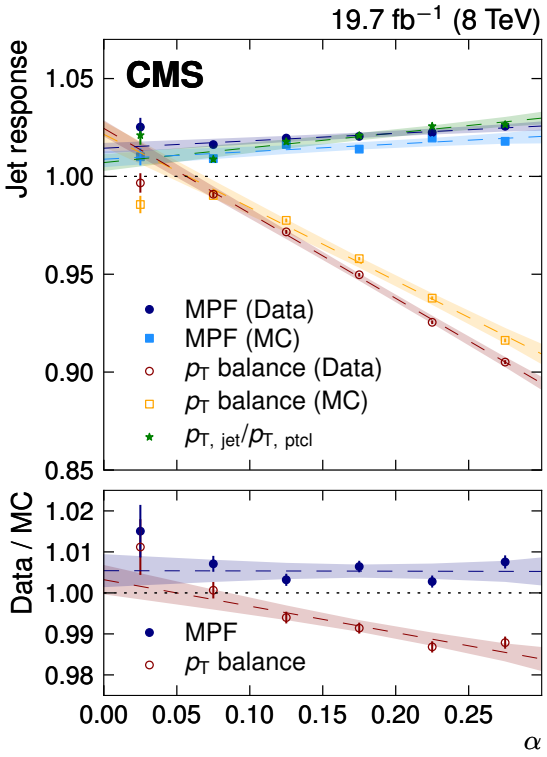

Figure 19. Jet response obtained with the p_T-balance and MPF methods in Z+jet events (points), for both data and simulation (MadGraph 4+pythia 6.4 tune Z2*), plotted as a function of $\alpha = p_{T,2nd\ jet}/p_{T,Z}$ (top). The response in data is scaled by a factor of 1.02, constant as a function of p_T. A fit to a first-order polynomial (dashed lines) is shown, together with the statistical uncertainty from the fit (shaded bands). Only events with $p_{T,Z} > 30$ GeV and $|\eta_{jet}| < 1.3$ are considered. The ratio of the jet response from the p_T-balance and MPF methods in data and simulation shown in the bottom panel. The simulated jet response $p_{T,jet}/p_{T,\,ptcl}$ is higher than unity because the jets are corrected with JEC from QCD dijet events with lower jet response than Z+jet events due to higher gluon fraction and larger underlying event.

The remaining effects of UE and OOC affect MPF and p_T balance slightly differently. It can be shown that, having corrected for ISR+FSR, the balancing and MPF responses can be written as

$$R_{jet,p_T} = R_{jet}\left(1 - \frac{p^{OOC}_{T,\,ptcl}}{p_{T,\,ptcl}} + \frac{p^{UE}_{T,\,ptcl}}{p_{T,\,ptcl}}\right), \tag{6.11}$$

$$R_{jet,MPF} = R_{jet}\left[1 - \left(1 - \frac{R_{OOC}}{R_{jet}}\right)\frac{p^{OOC}_{T,\,ptcl}}{p_{T,\,ptcl}} + \left(1 - \frac{R_{UE}}{R_{jet}}\right)\frac{p^{UE}_{T,\,ptcl}}{p_{T,\,ptcl}}\right], \tag{6.12}$$

where $p^{OOC}_{T,\,ptcl}$, $p^{UE}_{T,\,ptcl}$ are OOC and UE transverse momenta projected to the reference object axis, and R_{OOC}, R_{UE} are their effective responses. Compared to the p_T balance, the residual biases for MPF are multiplied by a factor that is typically about 10% or less, and can be safely ignored. The corrections for OOC and UE compensate each other, but for jet radii $R \geq 0.5$ the OOC effect is smaller than the one coming from the UE at low p_T. We can therefore estimate an upper limit on these biases by assuming an UE energy density of about 1 GeV per unit of jet area, which gives

2017 JINST 12 P02014

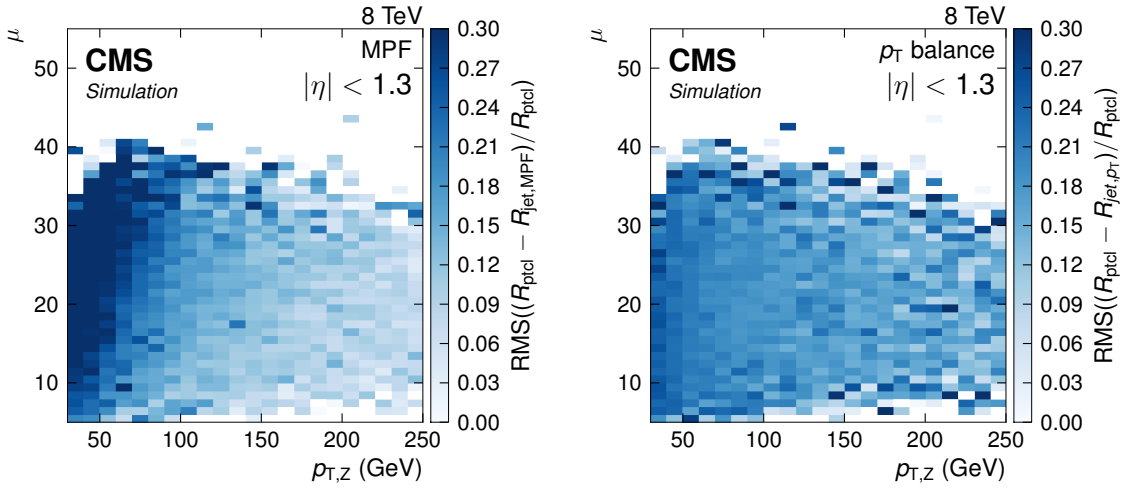

Figure 20. Relative resolution (blue scale) in the plane of mean number of pileup events (μ) and Z boson transverse momentum ($p_{T,Z}$) for the MPF balance (left) and p_T-balance methods (right).

a correction of at most ≈2.6% for $p_{T,\,ptcl} = 30\,\text{GeV}$ and jet distance parameter $R = 0.5$. This is compatible with the magnitude and sign of the observed difference of less than 2% between MPF and p_T balance at the $\alpha \to 0$ limit in figure 19.

Although the MPF and p_T-balance methods are biased in different ways, both can be corrected for ISR+FSR and are complementary to each other. The remaining biases from OOC and UE (both magnitude and response, see eqs. (6.11) and (6.12)) affect the p_T balance and MPF methods differently, and therefore fitting both simultaneously reduces the overall systematic uncertainty in the global fit. The relative statistical power (quantified by the relative resolution of the measured response, compared to the particle-level response) of p_T balance and MPF depends on the jet p_T and the level of PU, as seen in figure 20. The MPF method is sensitive to smearing in $\vec{p}_T^{\,\text{miss}}$ caused by PU, while the p_T balance is sensitive to the smearing in the momentum balance caused by ISR+FSR. The former effect dominates at low p_T, while the latter dominates at high p_T, such that both methods have similar sensitivity at $p_T \approx 100\,\text{GeV}$ for $\langle\mu\rangle = 20$.

Z+jet and γ+jet balance. The event selection is described in section 3.2. The JES is determined relative to precisely measured muons, electrons, and photons, with a tracker scale uncertainty of 0.2% for muons at $|\eta| < 2.4$ [29], an ECAL scale uncertainty of 0.5% for electrons at $|\eta| < 2.4$ [48], and 0.2% for photons at $|\eta| < 1.3$ [32].

The peak of the invariant-mass distribution of $Z \to \mu\mu$(ee) events is used to validate the muon (electron) energy scale between data and simulation. These are found to agree within 0.2% (0.5%). Additional checks ensure that the $\vec{p}_T^{\,\text{miss}}$ used in the MPF method is not biased by minimum-ionizing particle deposits of muons in the calorimeters, or by residual leakage of electron and photon energy into ECAL or HCAL not clustered in the reconstructed electron or photon. As the photon energy scale includes corrections for these unclustered contributions, special care is taken in order to avoid double counting of the leakage energy from fully calibrated PF photon superclusters to $\vec{p}_T^{\,\text{miss}}$ (such double counting will be referred to as electromagnetic footprint effect).

2017 JINST 12 P02014

Events are binned in photon or Z boson p_T to avoid resolution bias from the relatively poorly measured jets. The asymmetric ISR and FSR is accounted for by extrapolating to zero the additional jet activity (using the α variable, defined in eq. (6.9)). The response for $Z(\rightarrow \mu\mu)$+jet events is about 2% lower in data than in simulation, in agreement with what is observed for the jet response in the 7-TeV data. In figures 21 to 23, the jet response in data is first corrected by this factor, independent of the jet p_T. This correction is reabsorbed in the global fit, that constraints simultaneously the overall normalisation and the p_T-dependence of the ratio of data over simulation responses, to obtain the final correction.

The initial results are obtained after correcting jets and $\vec{p}_T^{\,miss}$ for pileup, jet energy response as extracted from simulation studies, and after applying the residual η-dependent corrections based on the dijet balance and the data/MC scale factor of 1.02 from $Z(\rightarrow \mu\mu)$+jet events. The MPF and p_T-balance methods have different sensitivities to ISR and FSR, which further reduces the uncertainty on the correction. Jet response measurements obtained from these two methods are shown in figure 21 for the nominal working point $\alpha < 0.3$. The results are presented for the three event samples ($Z(\rightarrow \mu\mu)$+jet, $Z(\rightarrow ee)$+jet and γ+jet) and are shown for data and simulation. The ratio of data to simulation is shown in figure 22. These results are displayed before extrapolating the additional jet radiation to zero and correcting for the p_T dependence of the JES: these effects will be taken into account in the global fit described in section 6.4. The agreement between the measured response in different samples is reasonable for data and MC simulation separately, and most remaining differences cancel out in the data/MC ratio. The differences between $Z(\rightarrow ee)$+jet and $Z(\rightarrow \mu\mu)$+jet/γ+jet events in the MPF method are due to a double counting of leakage from PF electrons and photons to $\vec{p}_T^{\,miss}$ (EM footprint effect on $\vec{p}_T^{\,miss}$), which is absent for muons and corrected for photons, but not for electrons. The differences between the MPF and the p_T-balance methods arise from ISR+FSR effects, and largely disappear in the data/MC ratio when k_{FSR} corrections are applied. Residual biases from ISR and FSR, as well as effects from lepton/photon scales and EM footprint in $\vec{p}_T^{\,miss}$, are dealt with in the global fit described in section 6.4.

Multijet balance. The extrapolation of the JEC to high p_T is constrained using data with the multijet balance (MJB) method introduced in ref. [14], with events where a high-p_T barrel jet is balanced by a recoil system, composed of two or more lower-p_T jets. In addition to the traditional balancing variable, $MJB = p_{T,lead}/p_{T,recoil}$, the response is also studied using an MPF method, where $MPF = 1 + (\vec{p}_T^{\,miss} \cdot \vec{p}_{T,recoil})/|\vec{p}_{T,recoil}|^2$. The jets used in the analysis are corrected for all the previous stages, including residual η-dependent corrections from dijets, but excluding the final absolute correction versus p_T. The response in data is scaled by a rough factor of 1.02, constant as a function of p_T, extracted from the study of $Z(\rightarrow \mu\mu)$+jet events. The $\vec{p}_T^{\,miss}$ is corrected for all jets with $|\eta| < 5$ and $p_T > 10$ GeV in the MPF method, but only jets with $p_T > 30$ GeV are used for the event selection and for constructing the $p_{T,recoil}$. The $p_T > 30$ GeV threshold ensures that the event selection is not biased by pileup jets, and that the recoil is composed of jets directly calibrated with data-based methods.

To interpret the results for JES we define an effective average $p_{T,\text{eff ptcl}}$ of the jets in the recoil, such that

$$R_{jet}(p_{T,\text{eff ptcl}})\vec{p}_{T,\text{recoil ptcl}} = \sum_{i \in \text{recoil jets}} R_{jet}(p_{T,i\text{ ptcl}})\vec{p}_{T,i\text{ ptcl}}, \tag{6.13}$$

where $R_{jet}(p_T)$ is the response of a jet of transverse momentum p_T.

2017 JINST 12 P02014

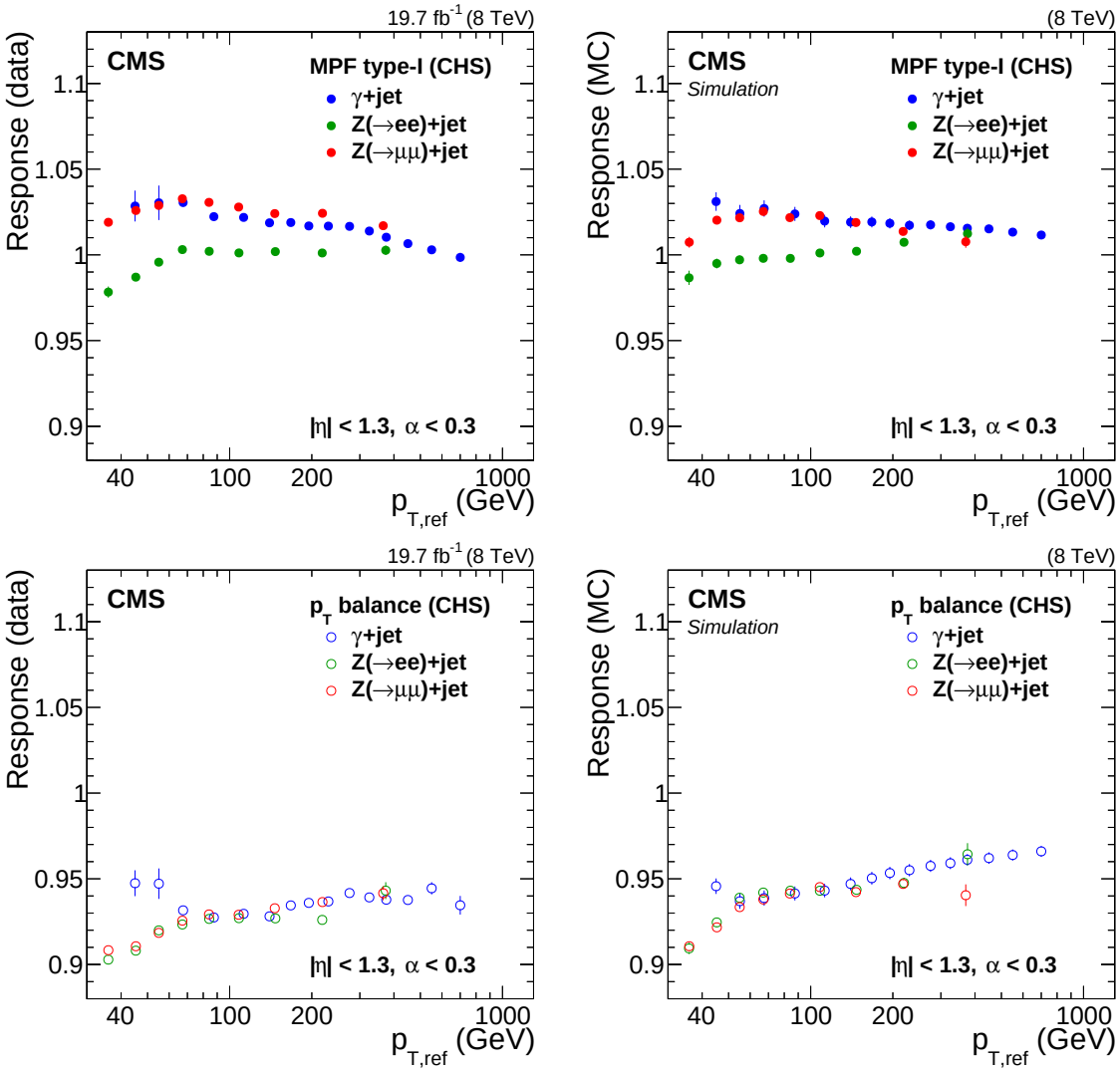

Figure 21. Comparison of jet response measurements from Z($\rightarrow \mu\mu$)+jet, Z($\rightarrow$ ee)+jet, and γ+jet samples as a function of Z boson or photon p_{T}. The jet response from the MPF method (top) and the p_{T}-balance method (bottom) is shown as a function of Z and γ p_{T} for data (left) and simulation (right). The Z($\rightarrow$ ee)+jet sample has not been corrected for the electron EM footprint in $\vec{p}_{\mathrm{T}}^{\,\mathrm{miss}}$, explaining the low MPF response in both data and simulation. The footprint effect is absent for muons and corrected for photons.

This is solved for $p_{\mathrm{T,eff\,ptcl}}$ in the log-linear approximation, $\mathrm{R_{jet}}(p_{\mathrm{T}}) = p_0 + p_1 \log(p_{\mathrm{T}})$, giving

$$p_{\mathrm{T,eff\,ptcl}} = p_{\mathrm{T,recoil\,ptcl}} \exp\left(\sum_i F_i \log(f_i)\right), \quad \text{where} \tag{6.14}$$

$$f_i = \frac{p_{\mathrm{T},i\,\mathrm{ptcl}}}{p_{\mathrm{T,recoil\,ptcl}}}, \quad \text{and} \quad F_i = f_i \cos(\Delta\phi_i). \tag{6.15}$$

The $\Delta\phi_i$ is the angle between the jet four-vector and the recoil, and by construction $\sum_i F_i = 1$. Labeling further

$$C_{\mathrm{recoil}} = p_{\mathrm{T,eff\,ptcl}}/p_{\mathrm{T,recoil\,ptcl}}, \tag{6.16}$$

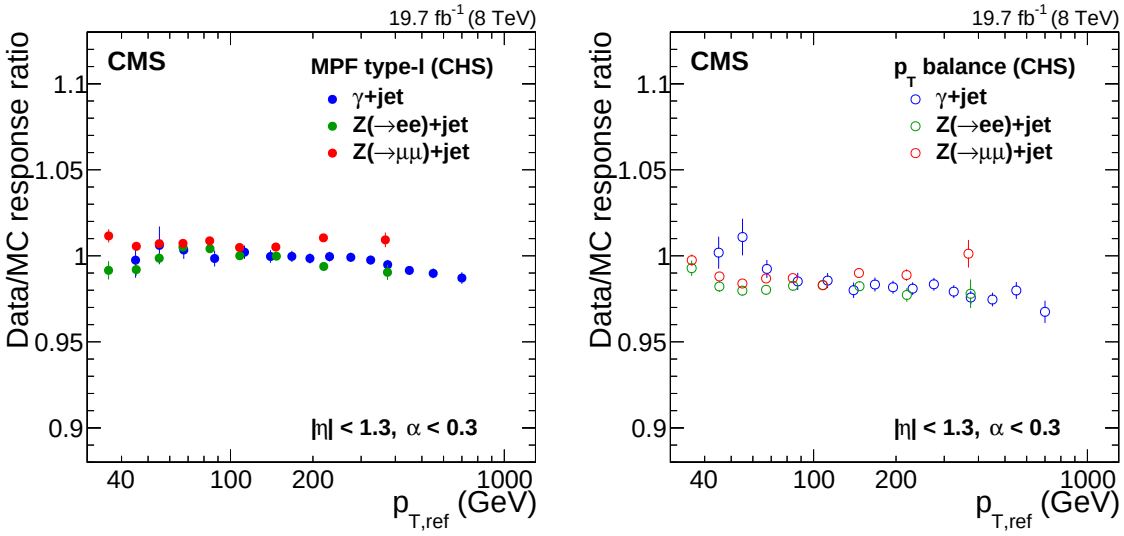

Figure 22. Ratio of the jet response measurement obtained from data and simulation with the MPF method (left) and p_T-balance method (right). Results are shown for the Z($\rightarrow \mu\mu$)+jet, Z($\rightarrow$ ee)+jet, and γ+jet samples. The Z($\rightarrow$ ee)+jet sample has not been corrected for the electron EM footprint in $\vec{p}_T^{\,\text{miss}}$, but the effect cancels out in the ratio of data over simulation.

we can write

$$\text{MJB} = \frac{R_{\text{jet}}(p_{T,\text{lead ptcl}})\,p_{T,\text{lead ptcl}}}{R_{\text{jet}}(p_{T,\text{eff ptcl}})\,p_{T,\text{recoil ptcl}}} \approx \frac{R_{\text{jet}}(p_T)}{R_{\text{jet}}(C_{\text{recoil}}p_T)}, \tag{6.17}$$

where the last approximation uses $p_{T,\text{lead ptcl}} \approx p_{T,\text{recoil ptcl}} \equiv p_T$. The $p_{T,\text{eff}}$ represents the effective average jet p_T in the recoil system (see eq. (6.13)), and the high-p_T jets are calibrated relative to $p_{T,\text{eff}}$. In the actual calculation, C_{recoil} is evaluated from reconstructed jets p_T (corrected with MC-based corrections and data-driven corrections for pileup effects and η dependence of the response), which is equivalent to the particle-level C_{recoil} to sufficient precision. C_{recoil}, shown in figure 23 (left), is therefore a measure of the lever arm of the multijet balance method in measuring p_T dependence of JES. Because the MPF method indirectly uses jets also below $p_T = 30$ GeV, its lever arm C_{recoil} is calculated from all jets of $p_T > 10$ GeV, while that of MJB is calculated only from jets of $p_T > 30$ GeV. The MPF method is stable with respect to the jet p_T threshold, while the MJB drops below MPF at low p_T when the p_T threshold is lowered to 10–20 GeV.

As the leading jet is calibrated using the recoil system as a reference object, the scale obtained for high-p_T jets using this method is relative to the average scale for the lower p_T jets, which are subject to systematic uncertainties particularly from jet-flavor response, pileup offset and η-dependent corrections. Systematic uncertainties arising from JEC, JER uncertainties, and PU modeling are propagated to the multijet analysis. As shown in figure 23 (right), the leading high-p_T jet is well balanced against the recoil within the JEC uncertainties, and the multijet balance method constrains the response of jets with a p_T as high as 1.3 TeV. The global fit takes as input the measured MJB, MPF and C_{recoil}, using the formulation of eq. (6.17).

2017 JINST 12 P02014

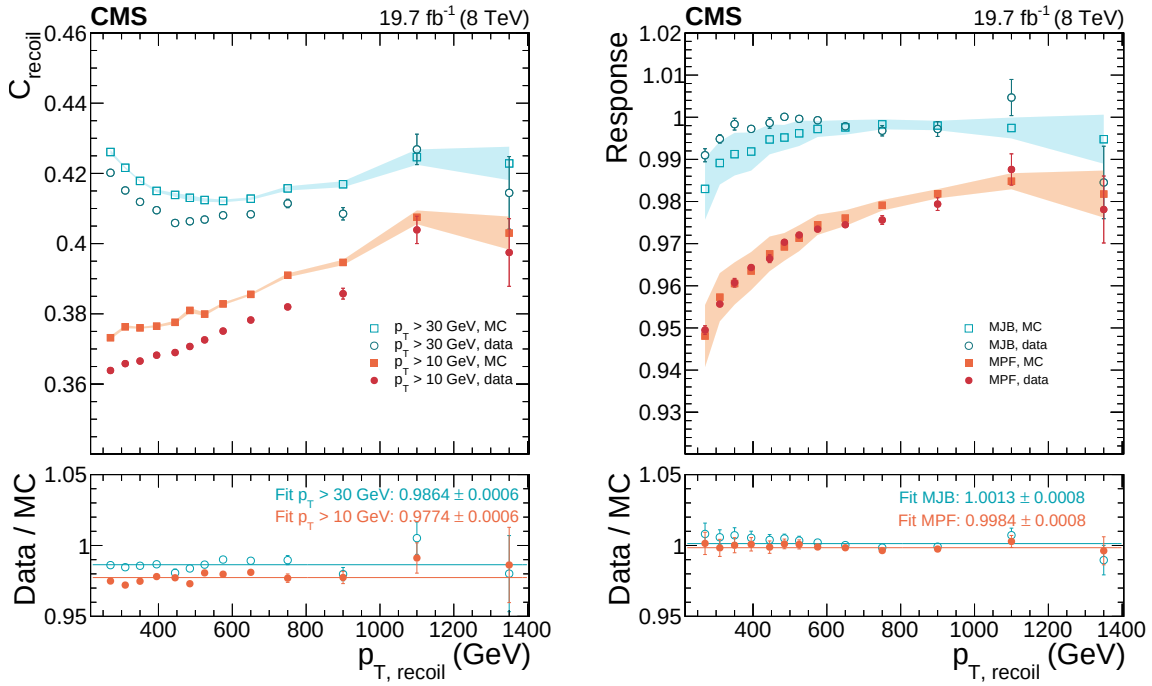

Figure 23. C_{recoil} ratio of the effective jet p_{T} of jets in the recoil over the total recoil p_{T}, (eq. (6.16)), calculated with recoil jets of $p_{\text{T}} > 30\,\text{GeV}$ (for MJB) and $p_{\text{T}} > 10\,\text{GeV}$ (for MPF) in data and MC simulation (left). Multijet balance response calculated with the MJB and MPF methods for data and MC simulation (right). The filled bands show the statistical uncertainty on MC for the left plot and the total (statistical and systematic) uncertainty on MC for the right plot. The error bars show the statistical uncertainty on data.

6.4 Global fit of absolute corrections

The absolute jet p_{T} scale is fitted simultaneously to the muon and electron (for $30 < p_{\text{T},Z} < 400\,\text{GeV}$), photon ($40 < p_{\text{T},\gamma} < 800\,\text{GeV}$), and multijet ($220 < p_{\text{T,recoil}} < 1300\,\text{GeV}$) data sets. The muon, photon, and electron scales are allowed to vary within their *a priori* uncertainties of 0.2%, 0.2%, and 0.5%, respectively. The results used as input to the global fit ($\alpha < 0.3$) with initial k_{FSR} corrections $\alpha < 0.3 \to 0$ are shown in figure 24 (left), overlaid with the final determination of JES and its uncertainties. The global fit is implemented as a χ^2 minimization. The fit results depend on some parameters that are known within given uncertainties, these are treated as nuisance parameters in the fit and added quadratically to the χ^2 expression. The nuisance parameters are related to the following effects:

- **Lepton/photon scale** uncertainties (0.2% for $\mu^{\pm}$, 0.2% for γ, and 0.5% for $\text{e}^{\pm}$, assumed to be uncorrelated, and independent of p_{T}).

- **ISR+FSR** uncertainty on the k_{FSR} correction fit used in the MPF and p_{T}-balance methods. The fit is performed in each sample using a three-parameter log-polynomial p_{T} dependence: its results, with their uncertainties, are used as input to the global fit and are shown as the shaded band labeled 'In' in figure 25.

2017 JINST 12 P02014

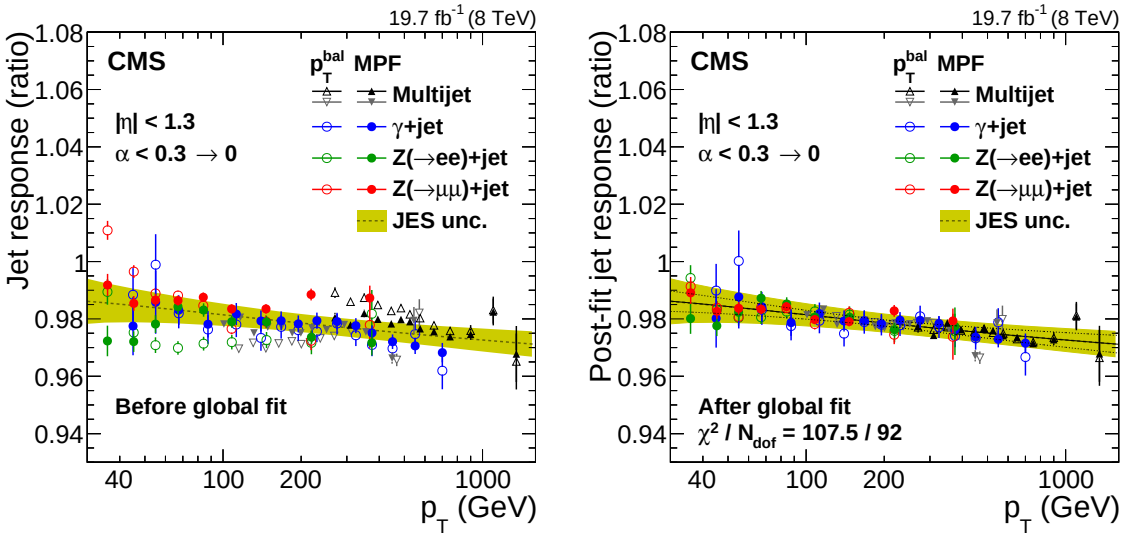

Figure 24. Comparison of the data-to-simulation ratio of the jet response measurements from Z($\rightarrow \mu\mu$)+jet, Z($\rightarrow$ ee)+jet, γ+jet, and multijet samples after applying the corrections for JES and ISR+FSR (left) and after applying, in addition, the nuisance parameter values found by the global fit (right). The uncertainty in the ratio, excluding jet-flavor and time-dependent effects, is shown by the shaded region. The solid line shows the global fit central value and the dotted curves the statistical uncertainty of the fit. As the multijet analysis connects the energy scale of jets in two different p_T ranges (eq. (6.17)), it can be used to constrain the high-p_T region given the low-p_T one (black triangles) or vice versa (grey triangles).

- **EM footprint** uncertainty for photons and electrons in the MPF method (0.2% for photons with footprint correction, and 0.5% for electrons without footprint correction, independently of each other, and independent of p_T).
- **Pileup** uncertainty coming from the difference in the offset calculated inside versus outside of the jet distance parameter.
- **Multijet** uncertainties from JES, JER, and pileup, separately for MPF and MJB.

The total number of nuisance parameters is three for the lepton/photon scales, $2 \times 3 \times 3 = 18$ for ISR+FSR, two for EM footprint, one for pileup, and $2 \times 3 = 6$ for multijet balance, for a total of 30 sources.

The global fit has two parameters of interest, one for fitting the absolute scale and one for fitting the p_T dependence under the assumption that the shape of the response variation is consistent with the one caused by a constant shift in single-pion response in HCAL, shown in figure 13 (right), and referred to as $f_{\text{HCAL}}(p_T)$ in the following. This assumption is supported by the time stability of charged-pion E/p in HCAL barrel. The function used to fit the p_T dependence is of the form $a + b(f_{\text{HCAL}}(p_T) - f_{\text{HCAL}}(p_{T,0}))$, hence introducing a reference momentum $p_{T,0}$ and fitting the shape relative to it. The value of $p_{T,0} = 208$ GeV is chosen to minimize the correlation between a and b.

The result of the p_T-dependent fit is shown in figure 24 (right). The data points are shifted by the nuisance parameter values found by the global fit in order to demonstrate the good consistency between the data sets. The nuisance parameters are normally distributed, with no outliers beyond

2017 JINST 12 P02014

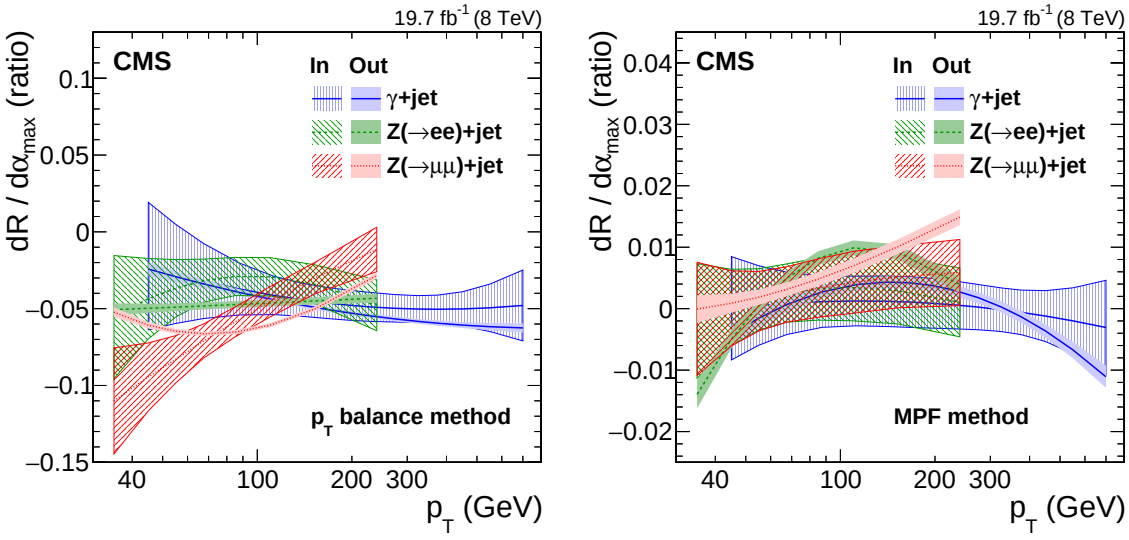

Figure 25. Central value of the data-to-simulation ratio of $\mathrm{d}R/\mathrm{d}\alpha_{\max}$, and its 68% probability region, as a function of jet p_{T}, for the p_{T}-balance (left) and MPF (right) methods. The $\mathrm{d}R/\mathrm{d}\alpha_{\max}$ is the derivative of the jet response evaluated in events with $\alpha < \alpha_{\max}$. The y-axis scale for the MPF method is zoomed by ×4 compared to the p_{T}-balance method, demonstrating the much smaller initial ISR+FSR uncertainty for this method. The shadowed regions show the input distributions to the global fit, while the full color regions show the post-fit distributions. The uncertainties on $\mathrm{d}R/\mathrm{d}\alpha_{\max}$ before the global fit are labeled 'In', and the uncertainties constrained by the global fit are labeled 'Out'.

the 2σ limit. The reduced goodness-of-fit, $\chi^2/\mathrm{N_{dof}}$, is $107.5/92 \approx 1$ for all degrees of freedom and for data points and nuisance parameters combined, indicating appropriate coverage by the systematic and statistical uncertainties. The statistical uncertainty band of the global fit, which is shown by the dotted curves, can be separated into two independent components, one describing the uncertainty in absolute scale, the other describing the uncertainty in p_{T} dependence coming from HCAL response. Other JES systematic uncertainties are calculated with respect to the factorization point $p_{\mathrm{T}} = 208\,\mathrm{GeV}$ that also has the smallest fit uncertainty.

The initial ISR+FSR corrections are constrained by the global fit, and their uncertainties before and after the fit are shown in figure 25 by the solid bands labeled 'In' and 'Out', respectively. The ISR+FSR correction for $\alpha < 0.3$ varies from about 1.5% for p_{T} balance ($k_{\mathrm{FSR}} \approx -5\%$) to less than 0.3% for MPF ($|k_{\mathrm{FSR}}| < 1\%$). This is consistent with the expectation that MPF is only sensitive to FSR and ISR to second order through differences in the response between the leading jet and the rest of the hadronic recoil, which are expected to be less than 20%. The ISR+FSR corrections as constrained by the fit are within the uncertainty of the input values, with the exception of the p_{T}-balance method for $\mathrm{Z}(\rightarrow \mu\mu)$+jet events, which stays within twice the input uncertainty and whose initial tension with respect to the $\mathrm{Z}(\rightarrow \mathrm{ee})$+jet channel is reduced by the fit.

6.5 Absolute correction uncertainties

Scale uncertainty. The dominant uncertainties for the scale factor arise from the following sources:

2017 JINST 12 P02014

- **Absolute scale**, 0.11%. The uncertainty in the fitted absolute scale is driven by the muon scale of 0.2%, obtained from the position of the Z boson mass peak, and by the photon scale uncertainty of 0.2%, achieved via a precise regression correction [32].

- **HCAL scale**, ≤0.6%. The uncertainty in the fitted HCAL scale is driven by the statistical uncertainty of the Z+jet sample at low p_T and by the γ+jet sample at high p_T. This uncertainty is labeled *SinglePionHCAL*.

- **Statistical uncertainty**, ≤0.1%. The statistical uncertainty covers the small residual difference between the global fit uncertainty calculated with the full covariance matrix and the uncertainty calculated from its diagonal elements (absolute scale and HCAL scale, above) only. Only positive contributions are included.

- **MPF bias**, 0.28%. The bias on the MPF method is composed of two subsources:

  - *Neutrino production*, 0.2%. This uncertainty is estimated from the 0.1% excess of both electron and muon energies in the PF jet compositions (shown in figure 46), which is assumed to be associated with a neutrino excess from decays of heavy-flavor hadrons, of similar order of magnitude. The estimate is compatible with uncertainties in the fraction of heavy-flavors from gluon splitting.

  - *ISR outside detector acceptance*, 0.2%. The extrapolation to zero additional jet activity cannot correct for ISR activity outside detector acceptance, which biases both MPF and p_T balance by the same amount. Phase space constraints limit ISR jet p_T outside the detector to $p_T \leq 30\,\text{GeV}$, which together with the results on the MPF and p_T-balance response in simulation after the JEC set an upper limit of 0.2% on this source.

Single-particle response and fragmentation systematics. We consider additional shape uncertainties from single-pion response and jet fragmentation using simulation. These studies were reported in section 5. The JEC at $p_T = 208\,\text{GeV}$ is known to high accuracy from the global fit so the simulation-based shape uncertainties are assumed to be zero at this reference p_T, but increase further away from the reference point. The single-particle response uncertainty of 3% is implemented using independent variations of $\pm\sqrt{2}3\%$ in responses in the ECAL and HCAL separately. The variation in the HCAL is included in the global fit and constrained to $-3.50 \pm 1.35\%$. The fragmentation uncertainty is taken directly as the PYTHIA 6.4/HERWIG++ 2.3 response difference.

Time dependence

The JES p_T dependence is believed to originate mostly from a reduction in the HCAL energy scale due to various effects, including uncorrected radiation damage in the front layers of the barrel calorimeter. To estimate the stability of the HCAL scale with time, the ratio of the calorimeter energy to track momentum $E_{\text{HCAL}}/p_{\text{track}}$ of isolated barrel hadrons was plotted as a function of time for pions that did not interact in the EM calorimeter. The 2012 (8 TeV) data sample is divided in four subsequent run periods, with slightly different conditions and trigger requirements: run A (with an integrated luminosity of $0.88\,\text{fb}^{-1}$), B (with $4.41\,\text{fb}^{-1}$), C (with $7.05\,\text{fb}^{-1}$) and D (with $7.37\,\text{fb}^{-1}$). The $E_{\text{HCAL}}/p_{\text{track}}$ shows variation of up to 4.5% between run A and run D for $p = 10\,\text{GeV}$ hadrons.

2017 JINST 12 P02014

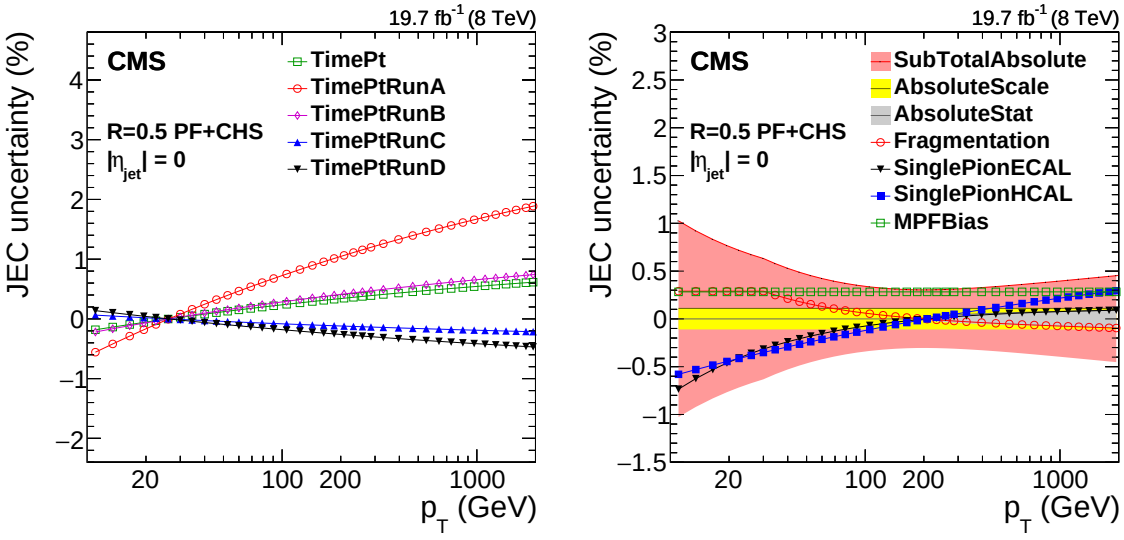

Figure 26. Absolute scale time-dependent uncertainty as a function of jet p_T for various data-taking periods (left). Systematic uncertainties for the absolute jet scale as a function of p_T (right). *SubTotalAbsolute* is the quadratic sum of *AbsoluteScale*, *AbsoluteStat*, *Fragmentation*, *SinglePionECAL*, *SinglePionHCAL* and *MPFBias*.

The HCAL scale variations relative to the full 2012 (8 TeV) data set were taken as uncertainties for each data-taking run (*TimePtRunA*, *TimePtRunB*, *TimePtRunC* and *TimePtRunD* for runs A, B, C and D, respectively), and then propagated to the jet response, as shown in figure 26 (left). The integrated-luminosity-weighted RMS of these run variations is taken as the time-dependent uncertainty in the absolute scale versus p_T, *TimePt*. In a similar fashion, the time-dependent uncertainty in the relative η-dependent corrections is estimated as the RMS of the correction factors obtained for short data-taking time periods, each weighted by the corresponding integrated luminosity. Neither uncertainty needs to be applied to analyses performed using the complete 2012 (8 TeV) dataset with unprescaled triggers, for which the time-dependent effects average out.

The *SinglePionECAL*, *Fragmentation*, and *MPFBias* uncertainties are summarized in figure 26 (right), together with the *AbsoluteScale*, *SinglePionHCAL*, and *AbsoluteStat* uncertainties, which are effectively the constant, p_T-dependent, and residual components of the statistical uncertainty in the global fit, respectively.

6.6 Summary of residual corrections

The data-based residual corrections for the relative JES versus η have been derived with dijet events using the MPF method, and for the absolute JES versus p_T with a global fit combining results from Z($\rightarrow \mu\mu$)+jet, Z($\rightarrow$ ee)+jet, γ+jet and multijet analyses with both MPF and p_T-balance methods. The residual corrections are summarized in figure 27, and are compared to the results for 7 TeV proton-proton collision data in 2010 and 2011. The residual response corrections are less than 3% in the barrel, less than 10% in the endcaps, and about 10% in the forward detector, with the exception of the narrow endcap-forward boundary region at $3.0 < |\eta| < 3.2$.

The uncertainty in JEC p_T dependence, which comes from detector simulation and from fragmentation modeling, is estimated to be less than 1% for $30 < p_T < 2000$ GeV. This uncertainty

2017 JINST 12 P02014

is evaluated after the global fit with Z+jet and γ+jet data in the range of about $30 < p_T < 700$ GeV, and multijet data extending to over 1 TeV. The uncertainty in JEC η dependence derives mainly from ISR+FSR modeling, the effect of JER, and the uncertainty in fitting any additional p_T dependence, with a total uncertainty rising from less than about 0.5% at $|\eta| < 2.5$ up to 2.5% at $|\eta| > 3$.

The residual corrections have been quite stable since 2011, when improvements to simulation and reconstruction algorithms were implemented after the first year of data-taking in 2010, after a hardware intervention in the HF readout helped reducing the rate of anomalous signals in the readout photomultiplier tubes. The most significant changes are seen at high p_T in the barrel, where we attribute the increase in residual corrections to a drop in the HCAL scale in data. The changes between 7 TeV in 2011 and 8 TeV in 2012 in the endcaps are at least partly attributable to the p_T dependence of the η-dependent corrections implemented at 8 TeV in 2012 for $p_T > 60$ GeV, and the changes in HF are due to statistical fluctuations.

7 Jet flavor corrections

7.1 Jet flavor definitions

The QCD dijet sample is enriched in gluon jets, while the Z+jet and γ+jet samples are enriched in quark jets, which is important for latest stages of JEC estimation. We define jet flavor in terms of the parton flavor ('physics definition'), where the particle jet is matched to the nearest generator-level parton, considering only partons belonging to the hard scattering matrix element process, within $\Delta R < 0.25$. According to this physics definition, jets resulting from hard gluon radiation without a matching parton have an undefined flavor. This convention is well-defined for both PYTHIA 6.4 and HERWIG++ 2.3. According to this definition, jets containing heavy-quark hadrons produced through gluon splitting (e.g., $g \to b\bar{b}$) are still classified as gluons.

The definition typically used for b-tagging purposes uses parton shower flavor ('algorithmic definition') that reclassifies jets with heavy-quark hadrons from gluon splitting as b- or c-quark jets. However, because this algorithm uses information from the final stage of the parton shower, it currently cannot identify gluon jets in HERWIG++ 2.3, which forces $g \to q\bar{q}$ splitting for all gluons. The algorithmic definition also has a tendency to reclassify jets with light quarks from gluon splitting as quark jets, and quark jets with early hard gluon radiation as gluon jets, mixing quark and gluon fractions.

We show the jet-flavor fractions for both definitions in figure 28 for QCD dijet, Z+jet, and γ+jet samples. The flavor fractions in the γ+jet sample are very similar to those of Z+jet in the $p_T > 200$ GeV range, except for a somewhat larger fraction of directly produced charm jets.

7.2 Simulated flavor corrections

The differences in response ($p_T/p_{T,\,ptcl}$) for different jet flavors arise mainly from variations in jet fragmentation energy and variations in particle composition of the jet. Softer jet fragmentation results in more particles outside the detector acceptance. With respect to particle composition, the neutral hadron fraction of the jet, f_{nh}, is seen to affect the response most. Jets from u and d quarks have the highest response, while those from gluons have the lowest, as a result of gluons fragmenting into the largest number of soft particles. The response values for heavy-flavor jets from c and b

2017 JINST 12 P02014

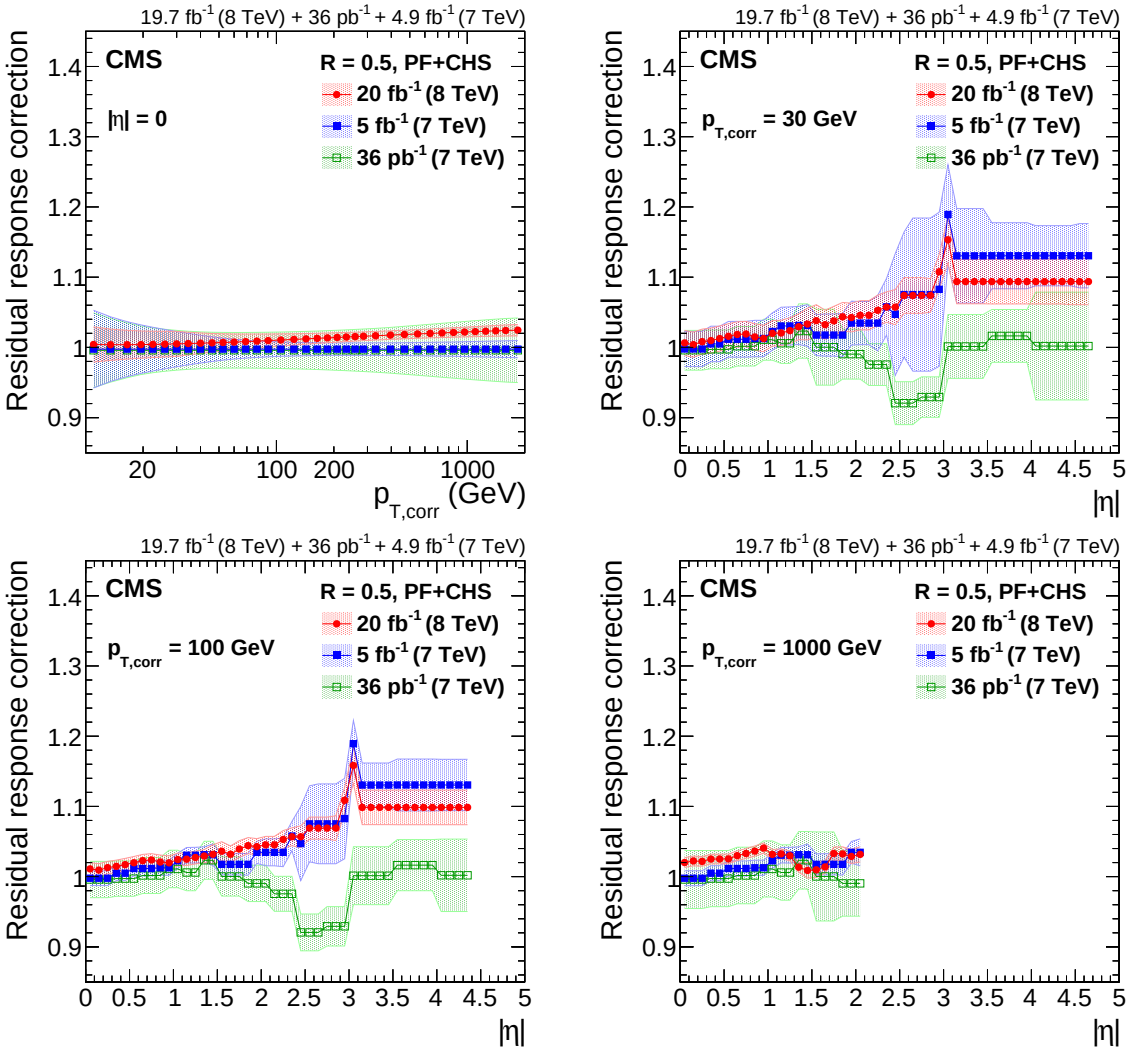

Figure 27. Residual data/simulation response correction factors for the 2012 data collected at 8 TeV for PF jets with CHS and $R = 0.5$, compared to corrections at 7 TeV corresponding to 36 pb^{-1} of data taken in 2010 [13] and 5 fb^{-1} taken in 2011 [46]. The comparison is shown at $|\eta| = 0$ versus $p_{\text{T,corr}}$ (top left), and as a function of $|\eta|$ for $p_{\text{T,corr}} = 30$ GeV (top right), $p_{\text{T,corr}} = 100$ GeV (bottom left), and $p_{\text{T,corr}} = 1000$ GeV (bottom right). The plots are limited to a jet energy $E = p_{\text{T}} \cosh \eta = 3500$ GeV so as to show only correction factors for reasonable p_{T} in the considered data-taking period.

quarks are in between those for u/d and g jets due to additional soft particles from heavy-flavor hadron decays compared to u and d jets. As a reminder, the CMS definition of jet energy response R excludes neutrinos, which would otherwise lower b and c jet response significantly. The jets from strange quarks also have relatively low response due to the high probability of producing long-lived strange neutral hadrons (mainly K^0_L) with significant p_{T}. This effect is specific to PF jets, which have a larger difference between charged and neutral hadron responses than calorimeter jets.

These effects are quantitatively demonstrated for jet response in figure 29 (left) for Z+jet events with $50 < p_{\text{T,Z}} < 70$ GeV, $|\eta_{\text{jet}}| < 1.3$, and $p_{\text{T,jet2}} < 0.3 p^{Z}_{\text{T}}$, where the jets are fully calibrated with the corrections relevant for simulated jets, as discussed in the previous sections. The biggest differ-

2017 JINST 12 P02014

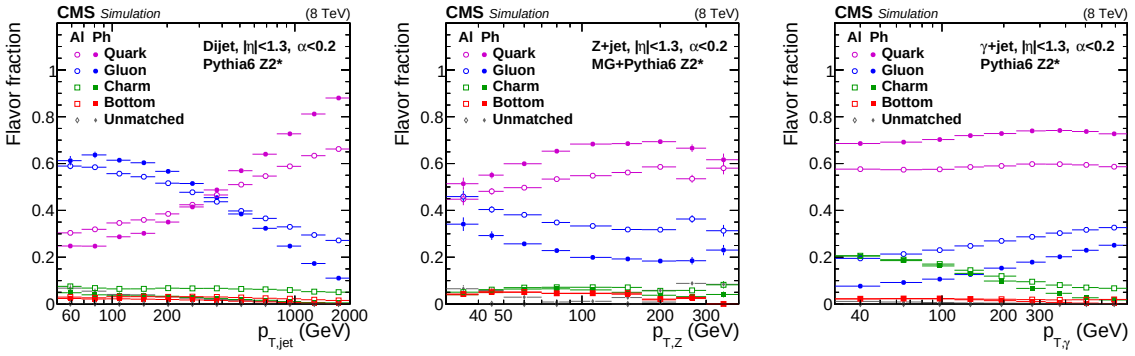

Figure 28. Jet-flavor fractions in the physics (Ph) and algorithmic (Al) flavor definitions for QCD dijet (left), Z+jet (middle), and γ+jet (right) samples. As explained in section 6, the variable $\alpha = p_{\mathrm{T,\,3rd\,jet}}/p_{\mathrm{T,ave}}$ for dijet events and $\alpha = p_{\mathrm{T,\,2nd\,jet}}/p_{\mathrm{T},\gamma/\mathrm{Z}}$ for Z+jet and γ+jet events.

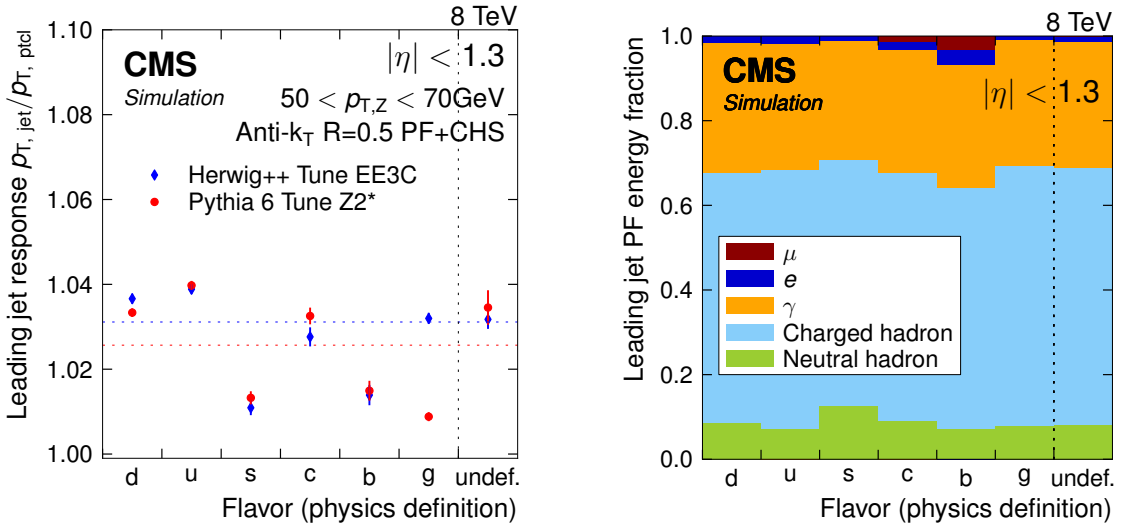

Figure 29. Comparison of jet response (left) and simulated composition (right) for different flavors of leading jets in Z+jet events with $50 < p_{\mathrm{T}}^{Z} < 70\,\mathrm{GeV}$, $|\eta_{\mathrm{jet}}| < 1.3$, and $\alpha = 0.3$ (defined in eq. (6.9)). The response values are compared for PYTHIA 6.4 and HERWIG++ 2.3, the composition is from PYTHIA 6.4.

ences between PYTHIA 6.4 and HERWIG++ 2.3 are observed for the gluon jets. The response is higher than unity for all flavors, since Z+jet events have lower contributions from the underlying event than dijet events, leading to a small bias from the hybrid jet area method, defined in section 4.3. Moreover, as shown in figure 28, Z+jet events have a smaller gluon fraction (25% for $p_{\mathrm{T}} = 60\,\mathrm{GeV}$) with respect to dijet (65% for $p_{\mathrm{T}} = 60\,\mathrm{GeV}$) events, and the different response of gluons and light-quark jets, visible in figure 30 (right), raises the average response for Z+jet events. Figure 29 (right) demonstrates the simulated jet composition for different jet flavors. The s-quark jets have higher neutral hadron fractions due to $\mathrm{K}_{\mathrm{L}}^{0}$ production, while the neutrino production in c and b jets is evident through the associated muons and electrons. The softer fragmentation of gluon jets has relatively little impact on the particle composition, but results in low effective response for the neutral hadrons R_{nh}.

2017 JINST 12 P02014

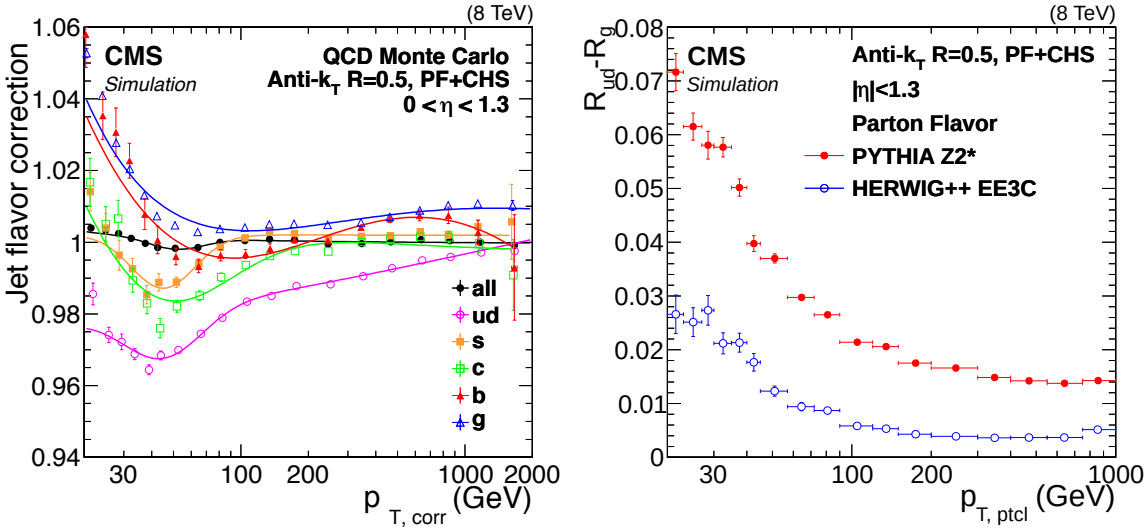

Figure 30. Residual jet-flavor correction factor as a function of jet $p_{T,\ corr}$ from PYTHIA 6.4 tune Z2*, derived on top of inclusive JEC and defined relative to the QCD flavor mixture (left). The neutrinos are excluded from particle jets, which brings c- and b-jet response in between that of light quarks and gluons. The lines show the parameterizations used for residual jet-flavor corrections. Difference in light-quark and gluon jet response as a function of jet $p_{T,\ corr}$, as predicted by PYTHIA 6.4 and HERWIG++ 2.3 (right).

Figure 30 (left) shows the inverse of the response for different flavors versus p_T, relative to the one for the QCD flavor mixture. The relative behavior of the differences has a weak dependence on p_T, but the absolute differences become smaller at high p_T. This can be explained by the asymptotic rise of the neutral hadron response towards unity at high p_T and detector acceptance effects becoming less significant for high-p_T jets.

While PYTHIA 6.4 and HERWIG++ 2.3 agree well on quark flavor response, there are significant differences in the gluon response modeling. A useful metric for the JES sensitivity to flavor response modeling is the difference in light-quark (uds) and gluon jet response, shown in figure 30 (right). The flavor sensitivity of the CMS PF algorithm is much reduced with respect to the CALO jets reconstruction, as was demonstrated in ref. [13].

7.3 Flavor uncertainties

We investigate the jet fragmentation and flavor response differences by comparing PYTHIA 6.4 tune Z2* and HERWIG++ 2.3 tune EE3C in balanced QCD dijet events. These two tunes have been shown to cover differences between data and simulation in many studies of jet structure and fragmentation, in particular for the variables used for quark and gluon tagging [49]. The jet flavors are tagged with the matching parton flavor, based on the physics definition. As shown in figure 31, we observe the largest response differences for the gluon jets, while the light-quark and heavy-flavor jets are in good agreement in both MCs.

The parameterized response differences as a function of η and p_T, combined with the flavor fractions in figure 28, are propagated through the fitting procedure used for data-based residual corrections to evaluate the systematic uncertainties from jet flavor. Jets in the barrel reference region $|\eta| < 1.3$ have flavor uncertainty only when the flavor mixture differs from the Z/γ+jet

2017 JINST 12 P02014

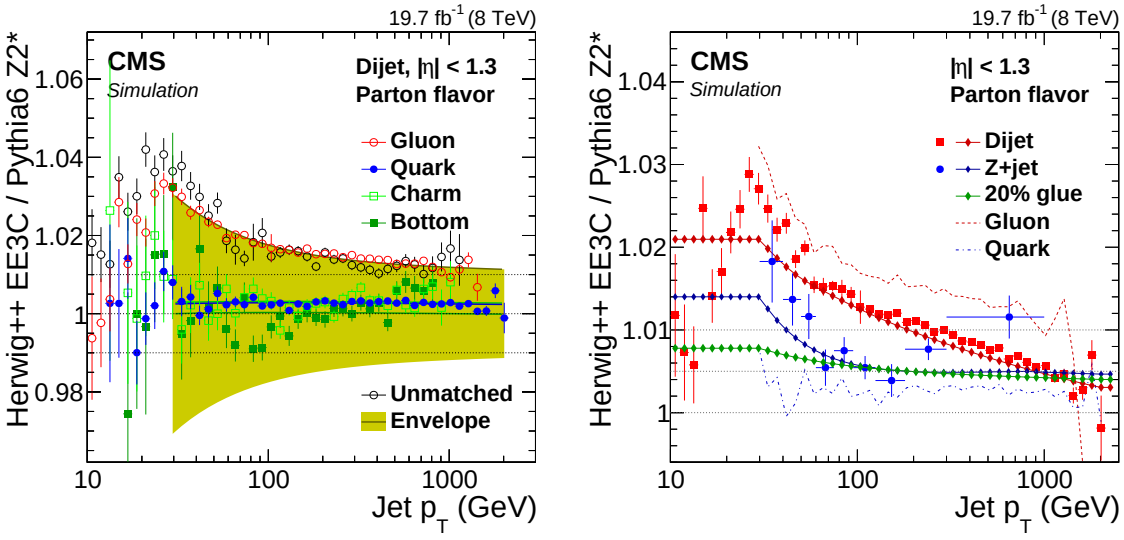

Figure 31. Left: ratio of jet responses in PYTHIA 6.4 (tune Z2*) and HERWIG++ 2.3 (tune EE3C) versus jet p_T, for pure jet flavors selected using the physics definition, where the shaded envelope highlights the largest differences observed for the gluon jets. Right: PYTHIA 6.4/HERWIG++ 2.3 response differences as a function of jet p_T for QCD dijet and Z/γ+jet flavor mixtures calculated from the parameterized flavor response differences (diamonds) and compared to the full simulation for dijet (squares) and Z+jet (circles) samples. The "20% glue" corresponds to the effective Z/γ+jet flavor mixture at $p_T = 200$ GeV, which has 20% of gluons. The ratio of the responses is also shown for pure gluon (dashed curve) and quark (dot-dashed curve) jets.

flavor mixture used in the data-based methods, which is roughly 20% gluons at $p_T = 200$ GeV. The η-dependent corrections influence the jet-flavor systematics through both the tag and the probe jet. The flavor mixture of the central tag jet is different from that in Z/γ+jet calibration samples, which leads to a flavor uncertainty for dijets within the reference region in the barrel. This barrel uncertainty for the dijet measurement is then propagated to the more forward regions through the dijet-based η-dependent corrections, with additional flavor uncertainties relative to the dijet flavor mixture for other samples.

The total flavor uncertainty ΔR_{flavor} for any given flavor mixture is estimated based on pure flavor response R_f (in PYTHIA 6.4 Z2* and HERWIG++ 2.3) and flavor fractions F_f in PYTHIA 6.4 Z2*:

$$\Delta R_{\text{flavor}}(p_T, \eta) = \hat{R}_{\text{mix}}(p_T, \eta) - R_{\text{ref}}(p_T, \eta), \tag{7.1}$$

where

$$\hat{R}_{\text{mix}}(p_T, \eta) = \sum_f (R_{f,\text{HERWIG++}}(p_T, \eta) - R_{f,\text{PYTHIA6}}(p_T, \eta)) F_{f,\text{mix}}(p_T, \eta), \tag{7.2}$$

$$R_{\text{ref}}(p_T, \eta) = \hat{R}_{\text{Z+jet}}(200\,\text{GeV}, 0) + \left(\hat{R}_{\text{dijet}}(p_T, \eta) - \hat{R}_{\text{dijet}}(p_T, 0)\right). \tag{7.3}$$

The symbol $\hat{R}$ indicates the linear combination of response differences for a given flavor mixture, and R_{ref} is relative to the Z/γ+jet flavor mixture used in the data-based methods. The various flavor uncertainties are compared in figure 32. This calculation returns by design zero flavor uncertainty for the Z/γ+jet flavor mixture at $p_T = 200$ GeV and $\eta = 0$ (about 20% gluons), which is where the

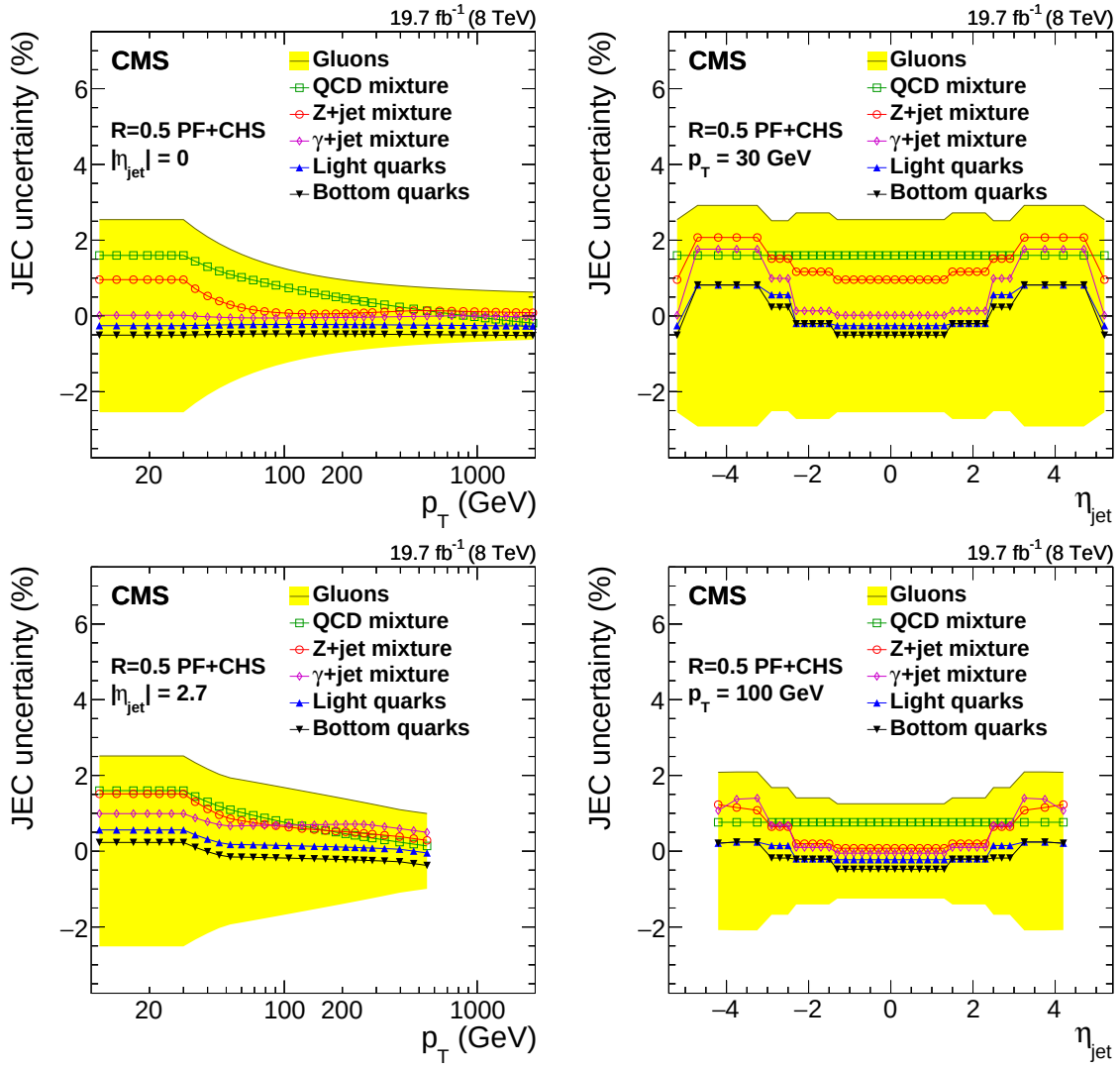

Figure 32. Systematic uncertainties in jet energy corrections for various flavor mixtures (QCD dijets, Z+jet and γ+jet) and pure flavors (gluons, light quarks and bottom quarks) as a function of jet p_{T} (left, for fixed $|\eta_{\mathrm{jet}}| = 0$, top, and $|\eta_{\mathrm{jet}}| = 2.7$, bottom) and η_{jet} (right, for fixed $p_{\mathrm{T}} = 30\,\mathrm{GeV}$, top, and 100 GeV, bottom). The sign of the systematic source indicates the sign of the PYTHIA 6.4 tune Z2* and HERWIG++ 2.3 tune EE3C difference. The shaded band shows gluon flavor response uncertainty symmetrically around zero.

constant absolute data/simulation scale factor is effectively determined in the (p_{T}, η, flavor) space. For the dijet sample the flavor uncertainty is constant versus η by design, but increases with p_{T} away from the effective flavor reference point. For other samples the flavor uncertainty depends both on p_{T} and η. The respective flavor uncertainties are provided for the Z+jet (*FlavorZJet*), γ+jet (*FlavorPhotonJet*), and dijet (*FlavorQCD*) mixtures as well as for the pure flavors (*FlavorPureGluon, FlavorPureQuark, FlavorPureCharm, FlavorPureBottom*). The flavor uncertainties are reliably determined only at $p_{\mathrm{T}} > 30\,\mathrm{GeV}$, where the flavor assignment for the leading jets has a small ambiguity. However, the flavor differences are reduced at $p_{\mathrm{T}} < 30\,\mathrm{GeV}$ in PF so the uncertainty at $p_{\mathrm{T}} = 30\,\mathrm{GeV}$ is used as a conservative upper limit on flavor uncertainties at lower p_{T} as well.

2017 JINST 12 P02014

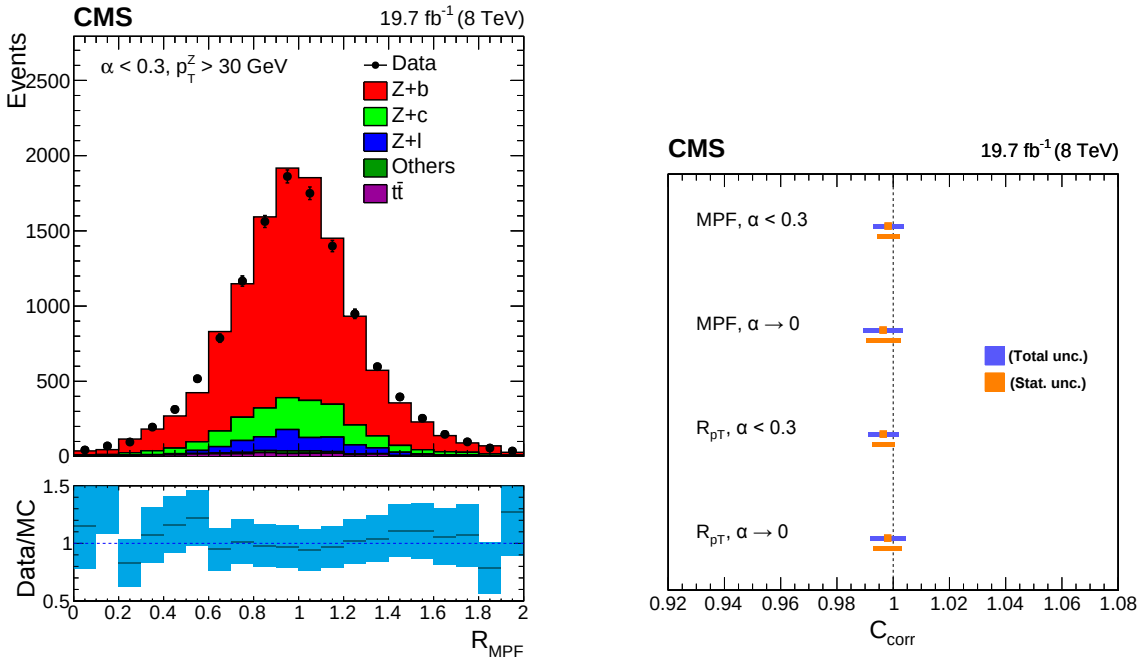

Figure 33. Distribution of the Z+b-jet response using the MPF method with a fixed requirement $\alpha < 0.3$ (left). Data-to-simulation ratio of the Z+b-jet response relative to the inclusive Z+jet sample with the MPF and the p_{T}-balance methods (right).

7.4 Z+b-jet balance

To check the flavor corrections and their uncertainties in data, we use a Z+b-jet p_{T}-balancing technique [50] that is a straightforward extension of the Z+jet balancing methods described in section 6.3. In addition to the Z+jet event selection criteria described in section 3.2, the leading jet is required to be b-tagged with the combined secondary vertex tagger at the medium working point [31], and the b-jet response is determined with both the MPF and the p_{T}-balance methods, as in the nominal Z+jet analysis described in section 6.3. The purity of the Z+b sample is about 70–80% and the MPF response distribution is well modeled by simulation, as shown in figure 33. To reduce systematic uncertainties, the main result is reported as a ratio of response in the Z+b-jet sample to that in inclusive Z+jet sample. This check is particularly important for the top quark mass measurements, which uses light-quark jets from W boson decays to constrain the energy scale for b jets from the top quark decay $\mathrm{t} \to \mathrm{Wb}$, assuming the same momentum scale for light-quark jets and b jets with similar kinematics [6].

The most precise result is obtained using the MPF method with a fixed requirement $\alpha < 0.3$ ('MPF, $\alpha < 0.3$' in figure 33). This gives a residual b-jet correction of $C_{\mathrm{corr}} = 0.998 \pm 0.004\,(\mathrm{stat}) \pm 0.004\,(\mathrm{syst})$ relative to PYTHIA 6.4 tune Z2*, which is consistent with unity and comparable in precision to the current b-jet flavor uncertainty of about 0.5%, shown in figure 32. The results from the response extrapolated to $\alpha \to 0$ (bottom symbols in figure 33 right) and from the p_{T}-balance method ($R_{p_{\mathrm{T}}}$) are consistent with the central MPF result. The systematic uncertainties, which include b-tagging efficiency and mistag rate, lepton scales, ISR- and FSR-related effects, and jet fragmentation, are dominated by the uncertainty in the fraction of p_{T} carried by the neutrinos

2017 JINST 12 P02014

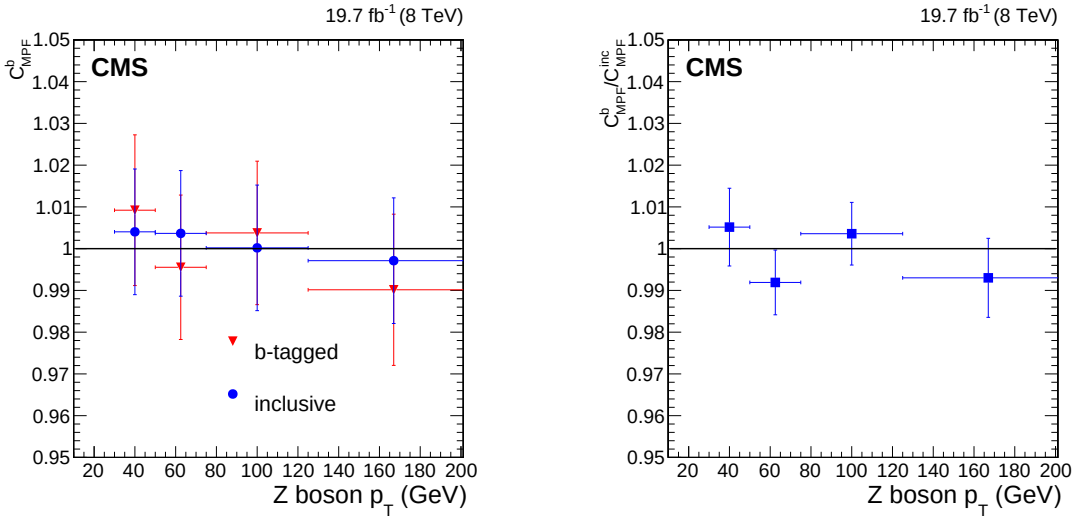

Figure 34. Residual correction factors (calculated as the ratio of the MC and data MPF response) as a function of Z boson p_T, for Z+b-jet and Z+jet events with $\alpha < 0.3$ (left), and their ratio (right).

produced in semileptonic decays of heavy-quark hadrons, which contributes 0.32% compared to 0.21% from all the other sources combined.

The corresponding result, as derived from HERWIG++ 2.3 tune EE3C, is

$$C_{\text{corr}} = 1.005 \pm 0.006\,(\text{stat}) \pm 0.004\,(\text{syst}), \tag{7.4}$$

and has a systematic uncertainty comparable with the one obtained for PYTHIA 6.4. The results of C_{corr} for PYTHIA 6.4 and HERWIG++ 2.3 differ by 0.5%, which is consistent with the expected flavor differences shown in figure 31.

To check for a possible p_T-dependence, the residual b-jet correction is shown as a function of p_T in figure 34, where the uncertainties are statistical and systematic. This figure shows the MPF results with the fixed $\alpha < 0.3$ requirement for the Z+b-jet and inclusive Z+jet events separately (left) and for their ratio (right), where most systematic uncertainties cancel out. As a result, while the uncertainties in figure 34 (left) are dominated by the systematic contributions, the uncertainties in figure 34 (right) are mostly statistical. The separate results are not corrected for the p_T-dependence of the absolute JES, which cancels in the ratio. The ratio is compatible with the assumption of no p_T-dependence, although it is limited by statistical uncertainties at the expected level of the systematic flavor uncertainties.

8 Jet p_T resolution

The jet p_T resolution is relatively poor compared to the resolution of many other physics objects (electrons, muons, photons), and the biases caused by jet resolution smearing can be important for steeply falling spectra and for resonance decays. In this section we present a determination of particle-level JER from MC simulation and the results from data-based methods for extracting a data/MC scale factor. The particle-level JER is defined as the width (estimated with a Gaussian

2017 JINST 12 P02014

fit) of the distribution of $p_{\mathrm{T,\,reco}}/p_{\mathrm{T,\,ptcl}}$, where $p_{\mathrm{T,\,reco}}$ and $p_{\mathrm{T,\,ptcl}}$ are the transverse momenta of the reconstructed and corresponding particle-level jets. JEC are applied before deriving JER.

8.1 Methods

Our measurement of JER is an extension of the methods used for measuring JES, but instead of looking at the mean of the response distribution, we are interested in its width. In addition, we need to correct for effects that do not produce an overall shift in the mean, but can widen the distribution.

For γ+jet (and Z+jet) events we can expand the p_{T} balance as follows:

$$\mathcal{B} = \frac{p_{\mathrm{T,\,jet}}}{p_{\mathrm{T},\gamma}} = \frac{p_{\mathrm{T,\,jet}}}{p_{\mathrm{T,\,jet\,ptcl}}} \frac{p_{\mathrm{T,\,jet\,ptcl}}}{p_{\mathrm{T},\gamma\,\mathrm{ptcl}}} \frac{p_{\mathrm{T},\gamma\,\mathrm{ptcl}}}{p_{\mathrm{T},\gamma}}, \tag{8.1}$$

where $p_{\mathrm{T,\,jet}}$ and $p_{\mathrm{T},\gamma}$ are the reconstructed jet and photon transverse momenta, and $p_{\mathrm{T,\,jet\,ptcl}}$ and $p_{\mathrm{T},\gamma\,\mathrm{ptcl}}$ the corresponding transverse momenta at particle level. For a sum of independent and identically distributed (IID) random variables, the quadratic summation of widths applies. For the product of eq. (8.1) we can take logarithms and apply $\log(1+X) \approx X$ for $X \ll 1$, which means that the normally distributed variables are also log-normally distributed with the same width σ. In the following, the symbols $\oplus$ and $\ominus$ indicate quadratic sum and subtraction respectively. For the widths σ we then have

$$\sigma\left(\frac{p_{\mathrm{T,\,jet}}}{p_{\mathrm{T},\gamma}}\right) = \sigma\left(\frac{p_{\mathrm{T,\,jet}}}{p_{\mathrm{T,\,jet\,ptcl}}}\right) \oplus \sigma\left(\frac{p_{\mathrm{T,\,jet\,ptcl}}}{p_{\mathrm{T},\gamma\,\mathrm{ptcl}}}\right) \oplus \sigma\left(\frac{p_{\mathrm{T},\gamma\,\mathrm{ptcl}}}{p_{\mathrm{T},\gamma}}\right), \quad \text{i.e.} \tag{8.2}$$

$$\sigma_{\mathcal{B}} = \frac{\sigma_{p_{\mathrm{T}}}}{p_{\mathrm{T}}} \oplus \sigma_{\mathrm{UE+OOC+ISR+FSR}} \oplus \sigma_{\gamma}. \tag{8.3}$$

In equation (8.3), all widths, apart from $\sigma_{p_{\mathrm{T}}}$, are relative quantities. The first part on the right-hand side is identified with the particle-level JER, $\sigma_{\mathrm{JER}} = \sigma_{p_{\mathrm{T}}}/p_{\mathrm{T}}$. The second term is the combined effect of UE, OOC, ISR+FSR, and presence of neutrinos. The final term is due to the photon p_{T} resolution and FSR, σ_{γ}. After extrapolating the secondary jet activity to zero, or equivalently correcting the measured resolution with the effective $k_{\mathrm{rad}} = \sigma_{\mathcal{B}}(\alpha \to 0)/\sigma_{\mathcal{B}}$, the effects of ISR and FSR become negligible. In this case the second term reduces to the effects from UE and OOC alone, and is referred to as the particle level imbalance (PLI), σ_{PLI}:

$$\sigma_{\mathcal{B}} k_{\mathrm{rad}} = \sigma_{\mathrm{JER}} \oplus \sigma_{\mathrm{PLI}} \oplus \sigma_{\gamma}. \tag{8.4}$$

Equation (8.4) can be rearranged as follows:

$$\sigma_{\mathrm{JER}} = \sigma_{\mathcal{B}} k_{\mathrm{rad}} \ominus \sigma_{\mathrm{PLI}} \ominus \sigma_{\gamma}. \tag{8.5}$$

k_{rad} is determined from data by fitting the resolution as a function of secondary jet activity $\alpha = p_{\mathrm{T,\,2nd\,jet}}/p_{\mathrm{T},\gamma}$, while σ_{PLI} and σ_{γ} are taken from MC simulation, after extrapolating to $\alpha \to 0$ for consistency. Since $k_{\mathrm{rad}}\sigma_{\gamma}$ is negligible compared to other effects, it is implicitly absorbed in the σ_{PLI} factor.

The quadratic addition and subtraction of widths is strictly correct only for RMS, or for resolutions that are approximately Gaussian. In practical cases, the dominant terms ($\sigma_{p_{\mathrm{T}}}$, $\sigma_{\mathcal{B}} k_{\mathrm{rad}}$) can be determined consistently from the RMS or a fit to the Gaussian core of the distribution,

2017 JINST 12 P02014

while the smaller contributions (σ_{PLI}, σ_γ) should typically use RMS. This is because the small contributions (with sufficiently steeply falling power-law tails) get folded into the Gaussian core of the distribution, as predicted, e.g., by the Central Limit Theorem (CLT), which states that the sum of multiple IID random variables tends to a Gaussian distribution, provided their power-law tails fall off sufficiently steeply (x^{-m}, with $m > 3$). For a variable that can be thought of as a multiplicative product of many independent random variables, the CLT applies in the logarithmic domain.

For dijet events the factorization is similar, except that JER now appears once for each jet, and PLI is derived from the asymmetry between two particle jets and includes the UE and OOC contributions twice. The dijet asymmetry [13] is defined as

$$\mathcal{A} = \frac{p_{\text{T, 1st jet}} - p_{\text{T, 2nd jet}}}{p_{\text{T, 1st jet}} + p_{\text{T, 2nd jet}}}, \tag{8.6}$$

and its resolution $\sigma_{\mathcal{A}}$ is given by

$$\sigma_{\mathcal{A}} k_{\text{rad}} = \frac{\sigma_{\text{JER,probe}}}{2} \oplus \frac{\sigma_{\text{JER,tag}}}{2} \oplus \sigma_{\text{PLI,dijet}}, \tag{8.7}$$

where $\sigma_{\text{PLI,dijet}}$ is the resolution of the asymmetry variable, built with the momenta of particle-level jets, and extrapolated to zero additional jet activity $\sigma_{\text{PLI,dijet}} = \sigma_{\mathcal{A}}^{\text{ptcl}} k_{\text{rad}}^{\text{ptcl}}$. It is related to the single jets PLI resolutions through $2\sigma_{\text{PLI,dijet}} = \sigma_{\text{PLI,tag}} \oplus \sigma_{\text{PLI,probe}}$.

For the special case where both jets are in the same region and share the same JER ($\sigma_{\text{JER,probe}} = \sigma_{\text{JER,tag}} = \sigma_{\text{JER}}$), we obtain:

$$\sigma_{\text{JER}} = \sqrt{2}(\sigma_{\mathcal{A}} k_{\text{rad}} \ominus \sigma_{\text{PLI,dijet}}). \tag{8.8}$$

For the case of one central and one forward jet, we can solve for the forward JER by subtracting the central JER determined from eq. (8.8):

$$\sigma_{\text{JER,forward}} = 2\sigma_{\mathcal{A}} k_{\text{rad}} \ominus 2\sigma_{\text{PLI,central–forward}} \ominus \sigma_{\text{JER,central}}. \tag{8.9}$$

In this case the $\sigma_{\text{PLI,central–forward}}$ is $\sigma_{\text{PLI,dijet}}$, determined consistently for the same combination of central and forward jets.

8.2 Simulated particle-level resolution

The jet p_{T} resolution is reasonably Gaussian, although some nongaussian low-response tails are present, e.g., due to rare detector effects such as inactive areas of the ECAL and to high-p_{T} particles punching through the HCAL. At low p_{T} symmetric tails appear due to combinations where two generator jets produce a single reconstructed jet, or vice versa. Such effects are typically well-modeled by a double-sided Crystal Ball function [51], as seen in figure 35. Low tails in response measurements are also commonly produced by neutrinos from semileptonic decays of heavy-flavor hadrons. This does not apply to particle-level resolutions, because CMS particle jets exclude neutrinos, but this does impact the dijet balance method used to measure JER in data.

We define the particle-level JER in simulation as the σ of a Gaussian fit to the $p_{\text{T, reco}}/p_{\text{T, ptcl}}$ distribution in the range $[m - 2\sigma, m + 2\sigma]$, where $p_{\text{T, reco}}$ and $p_{\text{T, ptcl}}$ are the reconstructed jet p_{T} and generated particle-level jet p_{T}, respectively, and m and σ are the mean and width of the Gaussian fit, determined with an iterative procedure. To maximize matching efficiency while still ensuring a

2017 JINST 12 P02014

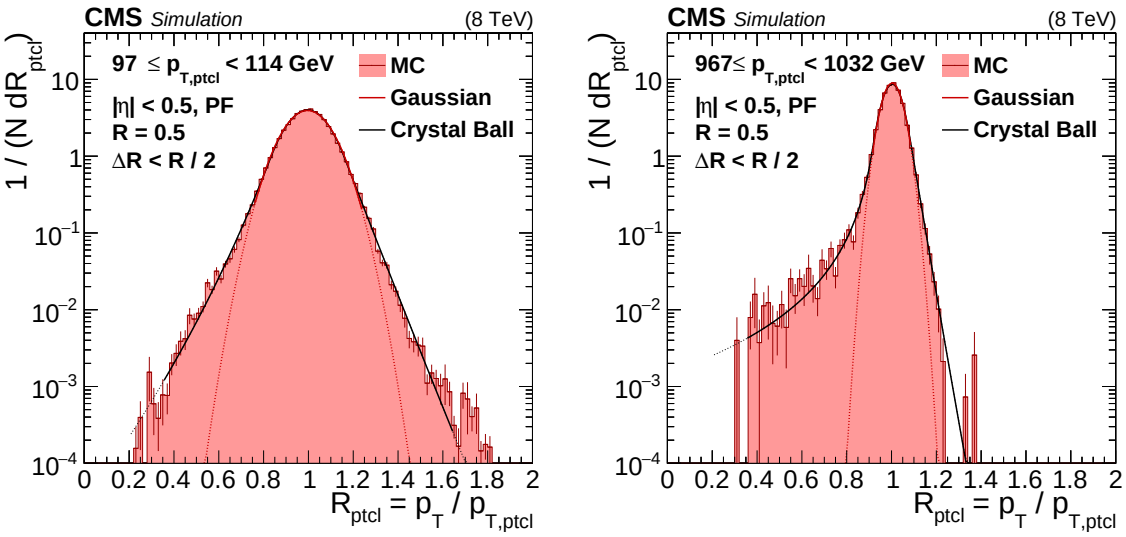

Figure 35. Jet p_T resolution distributions in the barrel for two bins of jet p_T. ΔR indicates the distance parameter value used for matching reconstructed jets to the corresponding particle-level jets. The nongaussian tails due to inactive areas of the ECAL and HCAL punchthrough become more visible for narrow high-p_T jets with small core resolution. The Gaussian core resolution is fit to within $\pm 2\sigma$ (solid line) and its extrapolation is indicated with a dotted line. The tails are well modeled by a double-sided Crystal Ball function.

unique match, the reconstructed and the generated jets are required to be within $\Delta R < R/2$ of each other, with R being the jet distance parameter.

The nongaussian tails increase the RMS of the distribution, and the differences affect the data-based dijet asymmetry, where two JER distributions are folded together with other (non) Gaussian distributions. The dijet asymmetry is effective in symmetrizing the tails, and according to the CLT the folded distribution will asymptotically approach a Gaussian distribution. The treatment of these effects will be discussed in more detail in the next section.

The particle-level JER in simulation with a pileup profile matched to 2012 (8 TeV) data is presented in figure 36 in bins of true number of PU interactions μ. The particle-level JER in simulation is parameterized with the "NSC" fit for calorimeter resolutions, where N is for noise (and pileup), S is for stochastic fluctuations that scale as $1/\sqrt{E}$, and C is a constant term with no p_T scaling (e.g., intercalibration):

$$\frac{\sigma_{p_T}}{p_T} = \sqrt{\frac{\mathrm{sgn}(N)N^2}{p_T^2} + \frac{S^2}{p_T} + C^2}. \tag{8.10}$$

As shown already in [13], for PF jets the possibility of having a negative N^2 term improves the description of the jet resolutions at low PU. As visible in figure 36, in the absence of pileup larger jets have better resolution due to several effects. These include better jet angular resolution (relevant for $p_T < 30$ GeV) and a smaller constant term from intercalibration, due to the jet energy being spread over more particles. These small gains are quickly negated in the presence of pileup, to which larger jets are more sensitive.

The noise term is very sensitive to the PU in jets, with each additional PU interaction contributing about 1 GeV of smearing in quadrature for $R = 0.5$ jets. The PU offset increases approximately

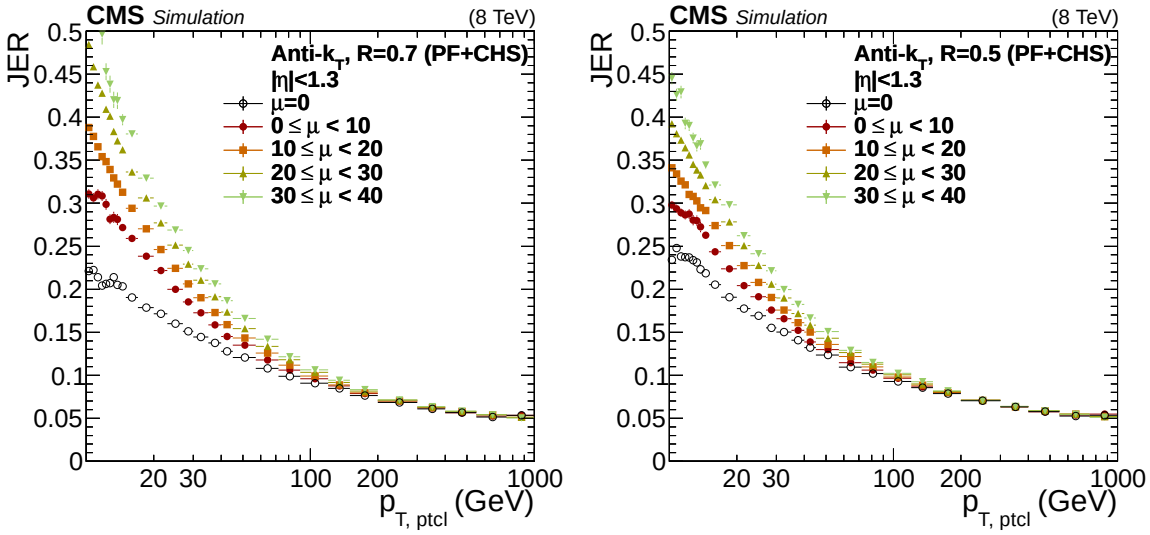

Figure 36. JER versus p_T in the barrel for varying levels of pileup μ. The results are shown separately for PF+CHS jets with size $R = 0.7$ (left), and for PF+CHS jets with size $R = 0.5$ (right).

linearly with number of collisions and jet area, μA, so that the noise from pileup is proportional to $\sqrt{\mu A}$. In contrast, the stochastic and constant terms are stable with respect to pileup, as shown in figure 37.

The JER also depends to some extent on the jet flavor. Gluon jets are wider than quark jets, and therefore less sensitive to local η–ϕ intercalibration of the detector. This is manifested as a smaller constant term and better JER at high p_T, as seen in figure 38 (left), where the constant term is 0.0338 ± 0.0002 for gluons, and 0.0406 ± 0.0002 for quarks. The intrinsic JER of c and b jets is similar to uds jets when excluding neutrinos at particle level. However, when neutrinos are included, as in figure 38 (right), the neutrinos produced in semileptonic decays of heavy-quark hadrons produce long response tails for the data-based measurements and cause substantial smearing of JER.

8.3 Dijet asymmetry

The jet p_T resolution in data is measured with the dijet asymmetry method [13] versus $p_{T,ave}$:

$$\mathcal{A} = \frac{p_{T,\,1st\,jet} - p_{T,\,2nd\,jet}}{p_{T,\,1st\,jet} + p_{T,\,2nd\,jet}} = \frac{p_{T,\,1st\,jet} - p_{T,\,2nd\,jet}}{2p_{T,\,ave}}, \tag{8.11}$$

where the width of the asymmetry distribution $\sigma_{\mathcal{A}}$ is related to the single jet resolutions as explained in equations (8.6)–(8.9).

The measured asymmetry distributions are Gaussian-like at low p_T, but some tails are evident at high p_T, as seen in figure 39 (left). These tails are reasonably well modeled by simulation. The particle-level JER in simulation is defined as a Gaussian fit to the core of the distribution within 2σ so we limit the impact of these tails and of outlier events by using a truncated RMS with 98.5% of the events in the core of the distribution for data and simulation. The truncation value is chosen to ensure that the core of the distribution is reasonably well described by a Gaussian. The resolutions are then extrapolated to zero secondary jet activity for data, reconstructed MC simulation, and generated MC simulation, as shown in figure 39 (right).

2017 JINST 12 P02014

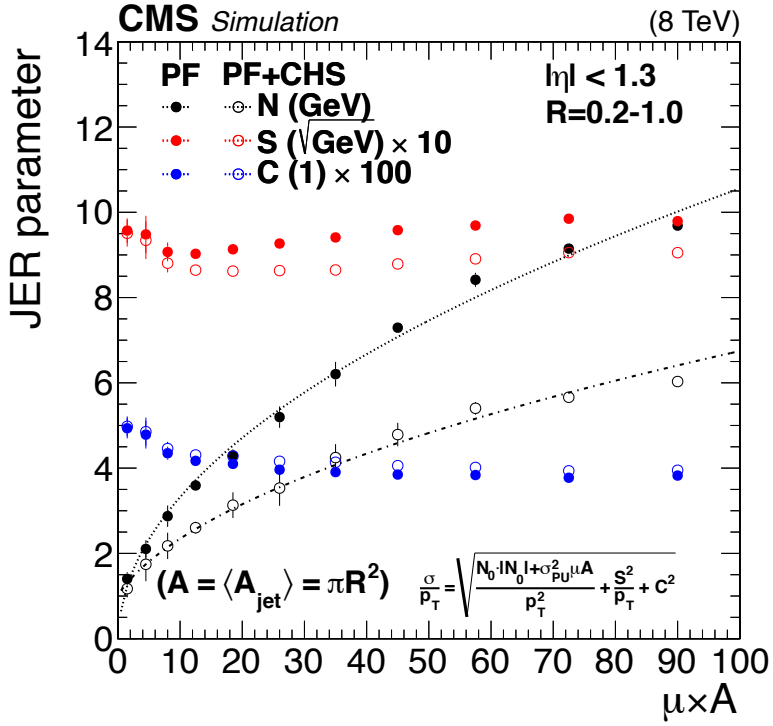

Figure 37. JER parameters (N, S, C; see text) fitted in bins of μ for various values of the distance parameter R (R = 0.2–1), as a function of their average value of pileup times jet area (μA). The results are compared between PF (solid symbols) and PF+CHS (open symbols). The dotted and dash-dotted curves represent the fit for PF and PF+CHS jets, respectively.

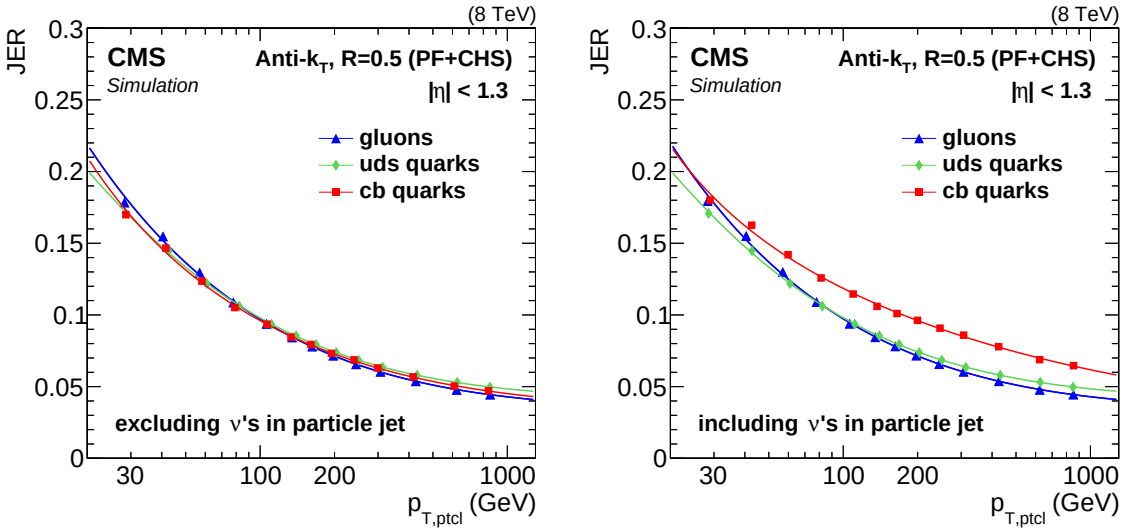

Figure 38. True JER in simulation for different jet flavors in the γ+jet sample, for jets with $|\eta| < 0.5$. The distributions are shown for particle-level jets with no neutrinos (left), and with neutrinos exceptionally included (right) to demonstrate the large fluctuations this induces for c and b jets.

2017 JINST 12 P02014

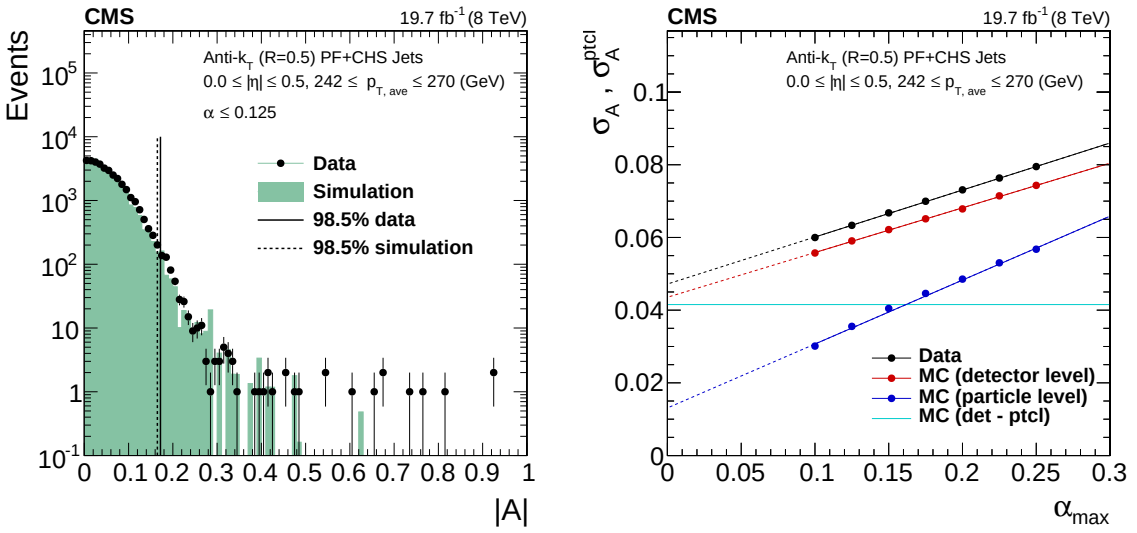

Figure 39. Left: asymmetry distribution, eq. (8.11), for data and simulation for jets with $p_T \approx 250\,\text{GeV}$ and $|\eta| < 0.5$. Right: asymmetry measured for various thresholds $\alpha_{\max}$, extrapolated to zero additional jet activity, for jets with $p_T \approx 250\,\text{GeV}$ and $|\eta| < 0.5$ in data and MC simulation at the detector- and particle-level. The light horizontal line indicates the average particle-level resolution obtained as the difference in quadrature of MC simulation reconstructed asymmetry and particle-level imbalance, extrapolated to zero additional jet activity.

The extrapolated asymmetry is finally corrected for the residual PLI effects, which are significantly smaller than the asymmetry, as shown in figure 40. This final stage does not significantly affect the data/MC ratio, as is also shown in figure 40, because the same PLI correction is applied to both data and MC simulation. The main effect of the correction is a slight increase in the data/MC ratio. The data/MC ratio is well-modeled by a constant fit in all the rapidity regions. These constant data/MC scale factors are summarized in figure 41. The fit is also repeated assuming different scale factors for the N, S (k_{NS}) and C (k_C) terms, which gives reasonable results although the statistical uncertainties are too big to distinguish the two cases. The difference between the measured scale factors k_{NS} and k_C and the central value obtained by the constant fit is considered as a systematic uncertainty.

The systematic uncertainties in the data-based method come from three main sources: correction for ISR and FSR, particle-level imbalance, and nongaussian tails. The data/MC ratio is also affected by the uncertainties in PU reweighting and JEC. The parameterization uncertainty comes mainly from the potential difference between the data/MC scale factors for the noise and stochastic terms k_{NS} and the one for the constant terms k_C. The systematic uncertainties for the data/MC ratio are evaluated as follows:

- **ISR+FSR correction**: the fit shown in figure 39 (right) uses a linear extrapolation $\sigma = \sigma_0(1 + k\alpha)$, which comes with an associated shape uncertainty beyond the first measured point. As a reminder, for dijet events, $\alpha = p_{\text{T, 3rd jet}}/p_{\text{T,ave}}$. Equation (8.11) suggests that another good functional form would be $\sigma = \sigma_0 \oplus k'\alpha$, which is used as an alternative model to estimate the systematic uncertainty in the ISR+FSR correction.

2017 JINST 12 P02014

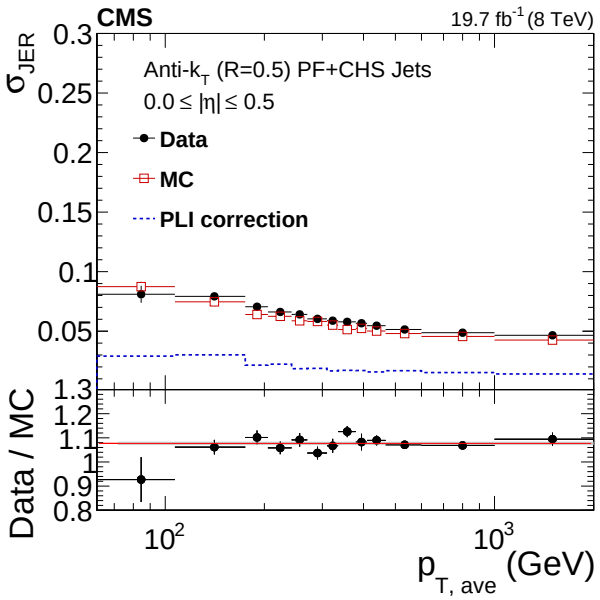

Figure 40. Extrapolated JER as a function of jet p_T obtained with the asymmetry method on dijet events for data (solid circles), reconstructed MC simulation (open squares), and particle-level simulation with PLI (dashed line). The bottom plot shows the ratio of data over MC.

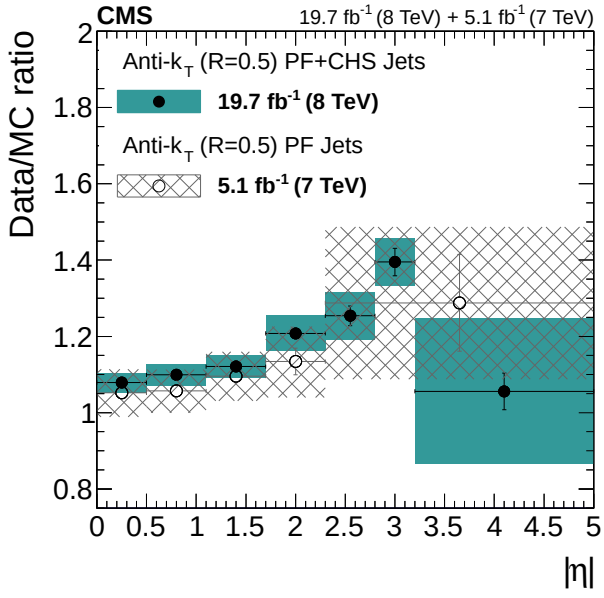

Figure 41. Jet energy resolution data/MC scale factor versus $|\eta|$ for dijet data collected at 8 TeV (closed circles, solid area) compared to results at 7 TeV (open circles, dashed area).

- **FSR+ISR radiation**: the α spectrum is not perfectly modeled in simulation, as shown in figure 42 (left). This affects the extrapolation correction. The systematics are evaluated by reweighting the α spectrum in simulation to match the data, and repeating the analysis.

- **Particle-level imbalance**: the PLI uncertainty is estimated by comparing the PLI obtained from two different MC simulations, PYTHIA 6.4 tune Z2* and HERWIG++ 2.3 tune EE3C, as shown in figure 42 (right). Based on these results we vary the PLI by ±25% to estimate the impact of PLI uncertainty on JER.

- **Non-Gaussian tails**: the uncertainty from nongaussian tails is estimated by changing the nominal 98.5% truncation for RMS to 97%.

- **PU reweighting**: the PU reweighting uncertainty is estimated by changing the minimum bias pp cross section from the nominal 69.4 to 73.5 mb when generating the target PU profile for simulation.

- **Jet energy scale**: the uncertainty arising from the knowledge of JES is evaluated by scaling up and down, according to the JEC uncertainty, all jet momenta in the simulation.

- **Parameterization uncertainty**: the parameterization uncertainty is estimated by considering different scale factors for the noise term N as well as the stochastic and constant terms S and C. Because the available range of data is not sensitive to the noise term, the noise term scale factor is varied by 10%.

The total uncertainty varies between 2–4% in the tracker covered region $|\eta| < 2.3$, and increases up to 6% in the endcaps and 20% in the HF, where the uncertainty is driven by the large differences between the results based on PYTHIA 6.4 and on HERWIG++.

8.4 The γ+jet balance

Complementary measurements of the jet p_T resolution in data are done with the γ+jet balancing versus $p_{T,\gamma}$:

$$\mathcal{B} = \frac{p_{T,\text{jet}}}{p_{T,\gamma}}. \tag{8.12}$$

The width of the balance distribution can be written as a convolution of the jet p_T resolution with additional smearing effects, as in eq. (8.7) for the case of dijets:

$$\sigma_{\mathcal{B}} = \sigma \oplus \sigma_{\text{ISR+FSR}} \oplus \sigma_{\text{PLI}}. \tag{8.13}$$

The JER is extracted from data and MC simulation that are binned in exclusive bins of α.

In the procedure, σ_{PLI} is fixed to the value obtained from a fit to the particle-level imbalance. The results from the photon+jet analysis are shown in figure 43, compared to the 7 TeV dijet data from 2011 (left) and to the 8 TeV dijet results from 2012 (right).

The following systematic uncertainties have been considered for γ+jet balancing:

- **QCD dijet background**: the uncertainty from QCD dijet contamination in the γ+jet sample is estimated by measuring JER with and without the dijet simulated sample added to the γ+jet sample.

2017 JINST 12 P02014

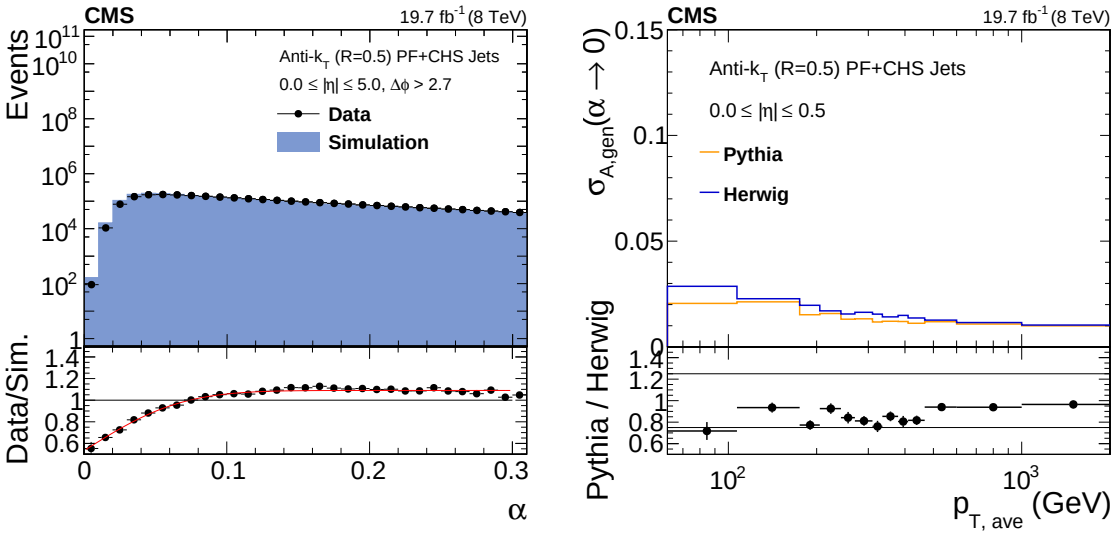

Figure 42. Left: the α distribution in data (circles) and simulation (histogram), with the function used for simulation reweighting overlaid on the ratio of data over simulation in the bottom plot. Right: comparison of particle-level imbalances $\sigma_{A,\mathrm{gen}}(\alpha \to 0)$ in PYTHIA 6.4 tune Z2* and HERWIG++ 2.3 tune EE3C as a function of jet $p_{\mathrm{T,ave}}$. The bottom plot shows the ratio of PYTHIA over HERWIG.

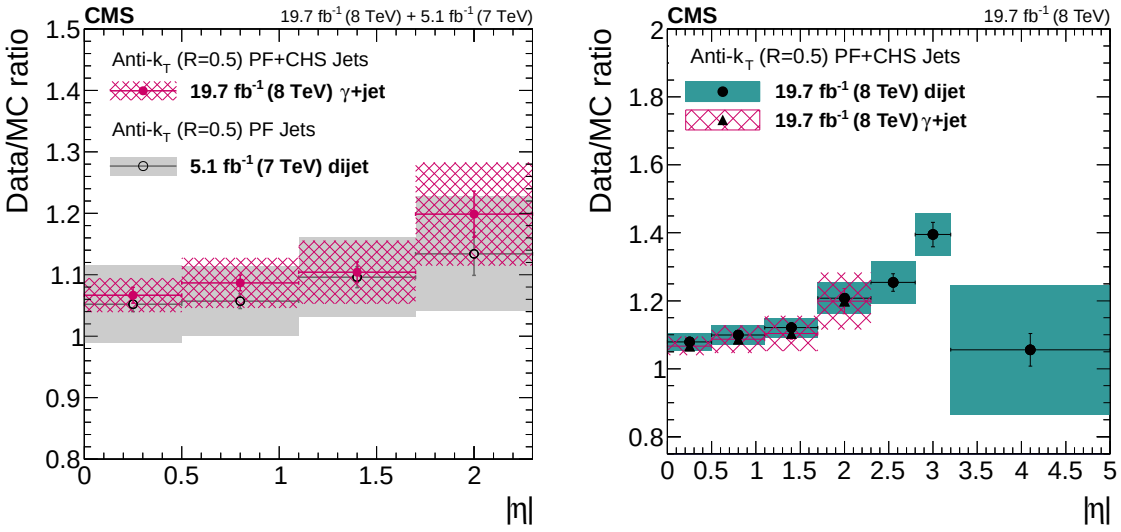

Figure 43. Data/MC scale factors for the jet p_{T} resolution as a function of $|\eta|$, determined from 8-TeV γ+jet data (hatched boxes) compared to those obtained from dijet data (solid boxes) at 7 TeV (left) and at 8 TeV (right).

- **Flavor uncertainty**: the poor resolution for c and b jets when including neutrinos at particle level, as shown in figure 38, can bias the JER measurement if the flavor fractions in data and simulation differ. To estimate this uncertainty, the quark and gluon fractions are varied by ±10%.
- **Out-of-cone showering**: out-of-cone showering is an important contribution to the PLI correction. To evaluate the systematic variation, the analysis was repeated for jet reconstruction with distance parameter $R = 0.7$ and the difference to the nominal $R = 0.5$ is taken as a systematic uncertainty.
- **Jet energy scale**: the uncertainty arising from the knowledge of JES is evaluated by scaling all jet momenta in simulation up and down by the JEC uncertainty.
- **PU reweighting**: the PU reweighting uncertainty is estimated by varying the minimum bias pp cross section by ±5% from the nominal 69.4 mb when generating the target PU profile for MC simulation.

The total uncertainty varies between 3–8% in the measured region at $|\eta| < 2.3$, increasing toward higher rapidity.

9 Systematic uncertainties

The JEC uncertainties for each correction have been detailed in their corresponding sections. They are also summarized in figure 44. For the purposes of physics analyses, the uncertainties are provided as *systematic sources* that include correlations across p_T and η. Each source represents a 1σ systematic shift that is fully correlated in p_T and η. The decorrelation in η (and p_T) is obtained by providing a single uncertainty from multiple sources that span only limited regions of phase space and can also overlap. Their sum in quadrature will always correspond to the original uncertainty, and the quadratic sum of all the sources equals the total JEC uncertainty. This approach is very similar to the set of eigenvectors provided, e.g., by the CTEQ collaboration [52].

The correlation factor ρ_{ij} between any two points $x_i = (p_{T,i}, \eta_i)$ and $x_j = (p_{T,j}, \eta_j)$ of the phase space can be calculated using the systematic sources s_k:

$$S_i = \sqrt{\sum_k s_{ki}^2}, \quad S_j = \sqrt{\sum_k s_{kj}^2},$$
$$\rho_{ij} = \frac{\sum_k s_{ki} s_{kj}}{S_i S_j}, \tag{9.1}$$

where s_{ki} is the relative uncertainty related to the systematic source k and S_i the relative total systematic uncertainties, for the point x_i. Figure 45 shows the level of correlation between various bins in p_T and η.

We recommend that in fits to the theoretical predictions (T_i) in data (D_i), the JEC systematic sources s_k are propagated as multiplicative factors to the theoretical predictions and their nuisance parameters ϵ_k are added in quadrature to the global χ^2:

$$\chi^2 = \sum_i \frac{[D_i - T_i(1 + \sum_k \epsilon_k s_{ki})]^2}{\hat{\sigma}_{D_i}^2} + \sum_k \epsilon_k^2, \tag{9.2}$$

2017 JINST 12 P02014

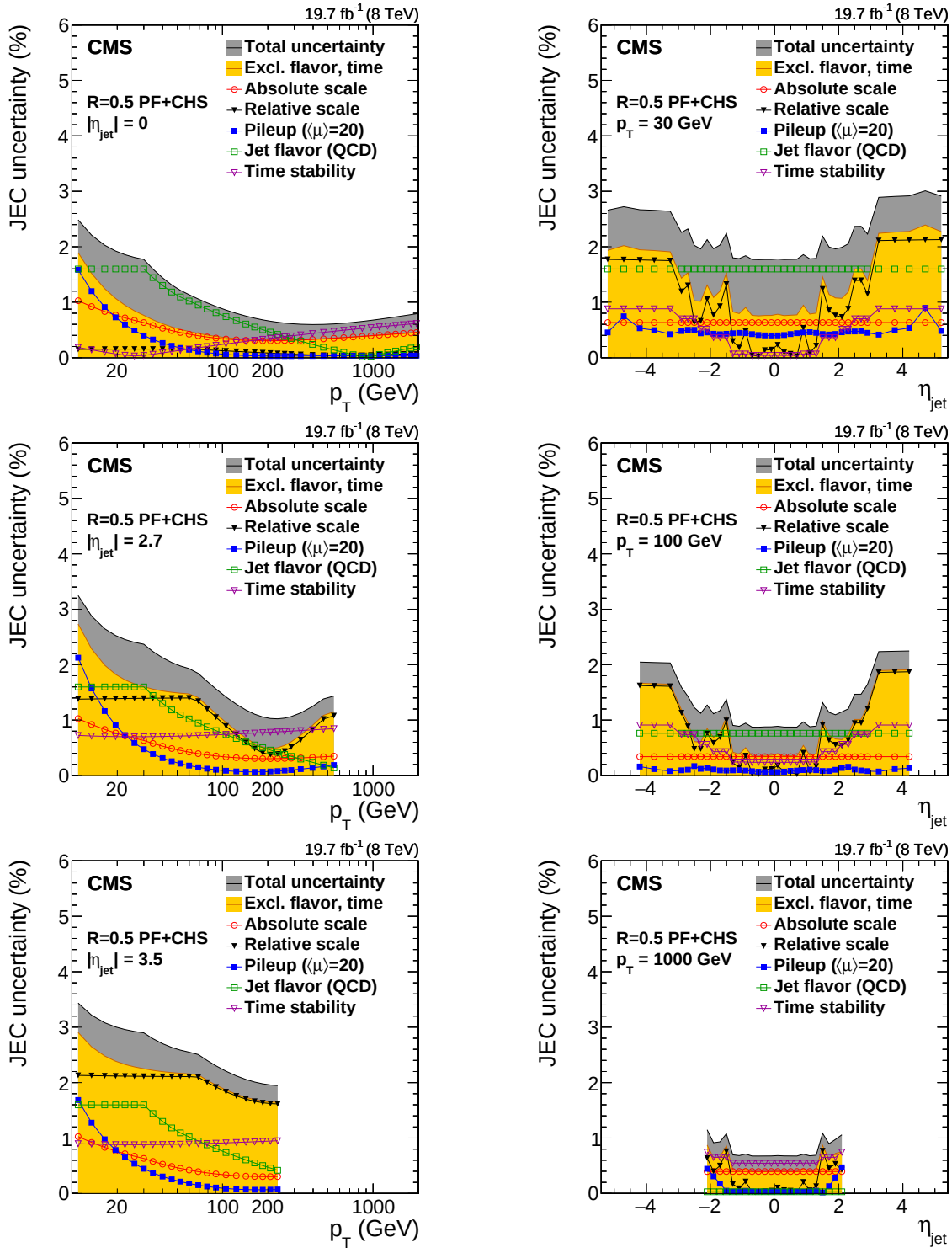

Figure 44. Summary of JES systematic uncertainties as a function of jet p_T (for 3 different $|\eta_{jet}|$ values, left) and of η_{jet} (for 3 different p_T values, right). The markers show the single effect of different sources, the gray dark band the cumulative total uncertainty. The total uncertainty, when excluding the effects of time dependence and flavor, is also shown in yellow light. The plots are limited to a jet energy $E = p_T \cosh \eta = 4000$ GeV so as to show only the correction factors for reasonable p_T in the considered data-taking period.

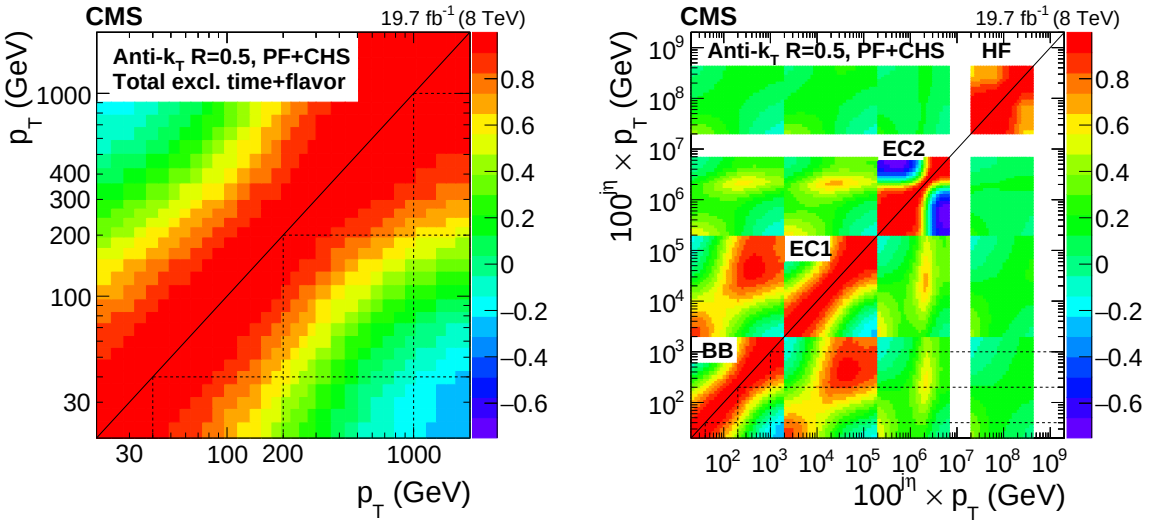

Figure 45. Correlation of total JES systematic uncertainties excluding time-dependent and flavor uncertainties (*TotalNoTimeNoFlavor*) for PF+CHS versus p_T at $|\eta| < 1.3$ (left). The color represents the degree of correlation (between −1 and 1). Correlation of JES systematic uncertainties (*TotalNoTimeNoFlavor*) for PF+CHS versus p_T (multiplied by $100^{j\eta}$) and jη bin (right). The integer jη is introduced for illustration purposes, with jη = 0 for the barrel region (BB), jη = 1 for the endcap inside tracker coverage (EC1), jη = 2 for the endcap outside tracker coverage (EC2), and jη = 3 for the forward region (HF).

where $\hat{\sigma}_{D_i}$ is the statistical uncertainty ($\hat{\sigma}_{D_i}$ denotes an estimated value for σ_{D_i}). The *a priori* expectation for the χ^2 minimum is that the ϵ_k will be Gaussian distributed with mean 0 and RMS 1. Alternatively, the global χ^2 can be calculated using the correlations from eq. (9.1):

$$\chi^2 = \sum_{i,j} (D_i - T_i) M_{ij}^{-1} (D_j - T_j), \quad \text{where} \tag{9.3}$$

$$M_{ij} = \sum_k s_{ki} s_{kj} + \hat{\sigma}_{D_i} \hat{\sigma}_{D_j} \delta_{ij}, \tag{9.4}$$

and δ_{ij} is the Kronecker delta function. The resulting χ^2 should be identical, but the former method also provides the nuisance parameters and the best fit theoretical predictions for sanity checks.

The implementation of correlations across η uses a rough subdivision based on detector structure to limit the final number of sources. The main regions are the barrel (BB: $|\eta| < 1.3$), endcap with tracking coverage (EC1: $1.3 < |\eta| < 2.5$), endcap outside tracking coverage (EC2: $2.5 < |\eta| < 3.0$), and hadron forward (HF: $3.0 < |\eta| < 5.2$). This division is applied to the systematic uncertainties sensitive to the detector response (*RelativePt*, *PileUpPt*), resolution (*RelativeJER*) modeling, and coming from statistical uncertainties (*RelativeStat*). Other systematic uncertainties are treated as fully correlated across the η bins.

The systematic sources are listed in table 1 together with their applicable η ranges. They are also briefly described in the following, summarizing the discussion in the respective sections. The uncertainty sources are also provided in special combinations, specific to different analysis use cases, described in table 2.

2017 JINST 12 P02014

Table 1. List of JES uncertainty sources, grouped by categories, with numbering, a short description, and range of validity in $|\eta|$.

Source	#	Description	Range
Pileup			
PileUpDataMC	01	Data vs. MC simulation offset with random cone (RC) method	$\|\eta\| < 5.2$
PileUpPtRef	02	True offset vs. RC $\otimes$ absolute p_T	$\|\eta\| < 5.2$
PileUpPtBB	03	True offset vs. RC $\otimes$ relative η	$\|\eta\| < 1.3$
PileUpPtEC1	04	True offset vs. RC $\otimes$ relative η	$1.3 < \|\eta\| < 2.5$
PileUpPtEC2	05	True offset vs. RC $\otimes$ relative η	$2.5 < \|\eta\| < 3.0$
PileUpPtHF	06	True offset vs. RC $\otimes$ relative η	$3.0 < \|\eta\| < 5.2$
(alternative source)			
PileUpMuZero	02-06b	True offset vs. RC $\otimes$ residual JES for $\langle\mu\rangle = 0$	$\|\eta\| < 5.2$
(benchmark source)			
PileUpEnvelope	02-06c	True offset vs. RC $\times$ 30%	$\|\eta\| < 5.2$
Relative JES (vs. η)			
RelativeJEREC1	07	Jet p_T resolution	$1.3 < \|\eta\| < 2.5$
RelativeJEREC2	08	Jet p_T resolution	$2.5 < \|\eta\| < 3.0$
RelativeJERHF	09	Jet p_T resolution	$3.0 < \|\eta\| < 5.2$
RelativeFSR	10	ISR+FSR correction	$\|\eta\| < 5.2$
RelativeStatFSR	11	ISR+FSR statistical uncertainty	$\|\eta\| < 5.2$
RelativeStatEC2	12	Statistical uncertainty	$2.5 < \|\eta\| < 3.0$
RelativeStatHF	13	Statistical uncertainty	$3.0 < \|\eta\| < 5.2$
RelativePtBB	14	Log-lin. vs. flat fit $\times$ 50%	$\|\eta\| < 1.3$
RelativePtEC1	15	Log-lin. vs. flat fit $\times$ 50%	$1.3 < \|\eta\| < 2.5$
RelativePtEC2	16	Log-lin. vs. flat fit $\times$ 50%	$2.5 < \|\eta\| < 3.0$
RelativePtHF	17	Log-lin. vs. flat fit $\times$ 50%	$3.0 < \|\eta\| < 5.2$
TimeEta	18	Relative η time dependence	$\|\eta\| < 5.2$
Absolute JES (vs. p_T)			
AbsoluteScale	19	Lepton scale, $\pm$0.11%	$\|\eta\| < 5.2$
AbsoluteMPFBias	20	MPF bias, $\pm$0.28% (from ν's $\oplus$ ISR acceptance, 0.2% $\oplus$ 0.2%)	$\|\eta\| < 5.2$
AbsoluteStat	21	Statistical uncertainty vs. p_T	$\|\eta\| < 5.2$
SinglePionECAL	22	Single-pion response in ECAL, $\pm$4.2%	$\|\eta\| < 5.2$
SinglePionHCAL	23	Single-pion response in HCAL, $\pm$1.5%	$\|\eta\| < 5.2$
Fragmentation	24	Jet fragmentation in PYTHIA 6.4 vs. HERWIG++ 2.3	$\|\eta\| < 5.2$
TimePt	25	Absolute p_T time dependence (indirectly with charged-pion E_{HCAL}/p)	$\|\eta\| < 5.2$
Jet flavor			
(only one of these)			
FlavorQCD	26a	QCD dijet mixture (default)	$\|\eta\| < 5.2$
FlavorZJet	26b	Z+jet mixture	$\|\eta\| < 5.2$
FlavorPhoton	26c	γ+jet mixture	$\|\eta\| < 5.2$
(or mixture of these)			
FlavorGluon	26d1	Pure gluon (g) (incl. g $\to$ q$\bar{\text{q}}$ and unmatched)	$\|\eta\| < 5.2$
FlavorQuark	26d2	Pure light quark (uds)	$\|\eta\| < 5.2$
FlavorCharm	26d3	Pure charm (c)	$\|\eta\| < 5.2$
FlavorBottom	26d4	Pure bottom (b) (Pure flavors refer to the *Physics* definition)	$\|\eta\| < 5.2$

Table 2. List of JES uncertainty source combinations with a short description and list of uncertainty components. The numbering of the sources (3rd column) corresponds to that used in table 1 (2nd column).

Enumerator	Description	List of sources
Total	Default uncertainty applicable for most CMS analyses	01–25, 26a
TotalNoFlavor	Default uncertainty without *FlavorQCD*, as basis for other mixtures	01–25
TotalNoTime	Uncertainty for unprescaled analyses with full 8 TeV data set	01–17, 19–24, 26a
TotalNoFlavorNoTime	Same as above without *FlavorQCD*, as basis for other mixtures	01–17, 19–24
SubTotalPileUp	Combination of pileup offset uncertainties	01–06
SubTotalRelative	Combination of relative η correction uncertainties	07–17
SubTotalAbsolute	Combination of absolute scale uncertainties	19–24
SubTotalScale	Scale uncertainties independent of p_T, plus statistical uncertainty	19–21
SubTotalPt	Combination of absolute scale p_T dependence uncertainties	22–24
SubTotalMC	Default uncertainty without *PileUpPt* sources	01,07–25,26a

The JES uncertainties are classified in four broad categories: pileup offset, relative calibration of JES versus η, absolute energy scale versus p_T, and jet-flavor response. In addition, the residual JES time-dependence is considered as an extra source of systematic uncertainty for samples other than the full unprescaled 8 TeV data set.

The **pileup offset** (section 4) is mostly important at low p_T. The pileup correction is taken from the true offset in simulation, and then scaled by the ratio of random cone offsets for data and simulation. The main systematic uncertainty is evaluated as 30% of the p_T-dependent difference between the true offset and the random cone offset in simulation. This difference is propagated through the fit procedure using Z/γ+jet (absolute p_T) and dijet (relative η) balancing to estimate the remaining residual pileup uncertainty after residual JES (section 6.4). A special alternative systematic (*PileUpMuZero*) is added to estimate the bias introduced by the data-based calibration for no-pileup ($\langle\mu\rangle = 0$) conditions. A residual uncertainty on the scale factor (*PileUpDataMC*) is estimated by varying ρ within one standard deviation.

The **relative η-dependent correction** (section 6.1) calibrates forward regions relative to $|\eta| < 1.3$ using dijet events. The main systematic uncertainties come from JER (*RelativeJER*) and the ISR+FSR (*RelativeFSR*) bias corrections. The JER uncertainty is evaluated by varying the JER for each detector region independently within the JER uncertainties estimated in section 8, when applying smearing to the simulation. The differences obtained from comparisons based on PYTHIA 6.4 and HERWIG++ 2.3 simulations are used to assign an ISR+FSR uncertainty. The η-dependent correction is parameterized with a log-linear function versus p_T at $|\eta| < 3.0$, and as a constant in HF ($3 \leq |\eta| < 5.2$). Half the difference between a log-linear fit and a constant fit is taken as a p_T-dependent parameterization uncertainty (*RelativePt*). For $|\eta| > 2.5$, the statistical uncertainty (*RelativeStat*) is also a significant contribution.

2017 JINST 12 P02014

The **absolute scale** (section 6.5) uncertainties for constant scale (*AbsoluteScale*) and p_T-dependent scale (*AbsoluteStat*) are extracted from a global fit to Z/γ+jet and multijet data. The former is essentially related to the lepton momentum scale for muons in Z($\rightarrow \mu\mu$)+jet, while the latter to the single-pion response in HCAL. Additional constant scale uncertainty is added for the biases of the MPF and p_T-balance methods (*AbsoluteMPFbias*) coming from neutrinos and ISR outside of detector acceptance. Shape uncertainties for the p_T dependence are considered from the following sources relative to the global fit reference of $p_T = 208\,\text{GeV}$ at $|\eta| < 1.3$: single-pion responses in ECAL and HCAL (*SinglePionECAL*, *SinglePionHCAL*) and jet response differences due to the different fragmentation models implemented in PYTHIA 6.4 and HERWIG++ 2.3 (*Fragmentation*).

The **flavor response differences** (section 7.3) are estimated using simulation, and cross-checked with Z+b-jet, and quark- and gluon-tagged photon+jet and Z+jet events. The flavor uncertainties are assigned based on PYTHIA 6.4 and HERWIG++ 2.3 differences, which are propagated through the data-based calibration chain with dijet, photon+jet, and Z+jet events. As a result, the flavor uncertainties are minimized for these flavor mixtures. The flavor differences in PYTHIA 6.4 and HERWIG++ 2.3 are largest for gluon jets, while the two MC simulations agree well on both light- and heavy-quark jets.

As explained in section 6.2, the JES in the endcaps shows some residual **time dependence**, even after correcting for radiation damage to the ECAL and HCAL. Prescaled triggers sample different run periods with different weights, leading to slight scale differences between different data sets. This time-dependence uncertainty is estimated as the RMS variation of the η-dependent corrections determined with dijet events for different run periods.

9.1 Uncertainties in 7 TeV analyses

For comparisons to published 7 TeV analyses, using the 2011 data set corresponding to an integrated luminosity of $5\,\text{fb}^{-1}$, we briefly summarize the main differences in the JEC and JES uncertainty sources relative to the ones reported in the previous publication [13]:

- **Pileup offset:** the 7 TeV uncertainties did not consider the absorption of the pileup offset jet p_T dependence into the residual η and p_T-dependent corrections, and the five *PileUpPt* sources (#02–#06 in table 1) were reported as a single large *PileUpPt* uncertainty without η decorrelation. The pileup offset correction was derived from the study of the offset, obtained with the RC method, as a function of the number of primary vertices N_{PV} for data only. This lead to a larger *PileUpDataMC* (#01) uncertainty, necessitating additional *PileUpOOT*, *PileUpJetRate* and *PileUpBias* uncertainties. The *PileUpOOT* covered the variation due to out-of-time pileup, now accounted for by deriving the offset versus μ before mapping to N_{PV}. The *PileUpJetRate* accounted for the offset p_T dependence, now corrected using p_T-dependent true offset from simulation. The 7 TeV offset correction was calibrated for jets in the p_T range of 20–30 GeV using simulation, with *PileUpBias* accounting for the uncertainty in the bias correction for data. In the current scheme, *PileUpBias* is absorbed into the *PileUpPt* sources.

- **Relative scale:** the 7 TeV JEC used a constant correction for each η bin, and the uncertainties did not provide the four *RelativePt* sources (#14–#17) to account for the small residual p_T dependence versus η. This led to some overestimates in the uncertainty correlation versus η. The

2017 JINST 12 P02014

recommended way to address *a posteriori* the underestimated decorrelation in the 7 TeV uncertainties is to clone the 7 TeV *SinglePion* source (roughly corresponding to current uncertainties #22–#23) into five separate sources, spanning η ranges $|\eta| < 0.5$, $0.5 < |\eta| < 1.0$, $1.0 < |\eta| < 1.5$, $|\eta| < 1.5$ and $|\eta| > 1.5$, with weight 1 for the last source and $1/\sqrt{2}$ for the four others. This ensures 50% decorrelation for the *SinglePion* source within the barrel bins, and 100% decorrelation between the barrel and endcap, while preserving the total uncertainty. The *RelativeFSR* (#10) and *RelativeStatFSR* (#11) sources were reported as a single *RelativeFSR* uncertainty.

- **Absolute scale:** the 7 TeV absolute correction was a single constant factor and did not include any p_T dependence except for the uncertainties. The three flat absolute scale factor uncertainties (#19–#21) were reported as a single source (*Absolute*), as were the p_T-dependent uncertainties from single-pion response in the ECAL (#22) and HCAL (#23). The 7 TeV *SinglePion* uncertainty, which corresponds to the latter two uncertainties, was a factor two larger and is uncorrelated with the 8 TeV *SinglePionHCAL* (#23) source, which is now based on the value obtained from the global p_T-dependent fit. The *AbsoluteScale* (#19) and *AbsoluteStat* (#21) are also based on the global fit, and therefore uncorrelated with the 7 TeV source *Absolute*.

- **Time dependence:** there was neither evidence of residual JEC p_T dependence at 7 TeV, nor of time dependence in the absolute correction. Therefore, the *TimePt* source (#25) was not provided.

In total, the 7 TeV uncertainties included sixteen uncertainty sources, ten fewer than the current recommendations (#1–#26): one less for pileup (four new sources and three obsolete), five less for relative scale, three less for absolute scale and one less for time dependence. The current uncertainties provide a more detailed description of correlations versus both η and p_T.

10 The PF jet composition

The different detector contributions to the JES can be understood in more detail by looking at the fractions of jet energy reconstructed as the various types of PF candidates. Although this information is not yet used to directly constrain JES, it gives valuable information in monitoring the stability of JES.

The PF jet composition is determined from the dijet sample, selected as described in section 3.2, using the tag-and-probe method. In this method the tag jet, which is in the barrel and matched to the trigger in data, provides measurement of the jet p_T, while the back-to-back probe jet is used for an unbiased determination for PF candidate energy fractions. This indirect method avoids the selection bias that would enhance energy fractions correlated with upward fluctuations in jet p_T. This is particularly important because data and simulation are known to have different resolutions, and we want to avoid introducing JER biases in the composition measurement.

The measured PF energy fractions are shown in figure 46 as a function of p_T and η. The agreement between data and simulation is at the level of 1–2% in the barrel, consistent with the measured residual JEC. In particular, the fraction of charged hadrons associated with pileup agrees well between data and simulation. The differences increase at high p_T, where the tracking efficiency within the densely populated jet core drops significantly, and PF becomes more sensitive to the calorimeter scale. The differences also increase at higher rapidities, where the observed residual JEC are larger.

2017 JINST 12 P02014

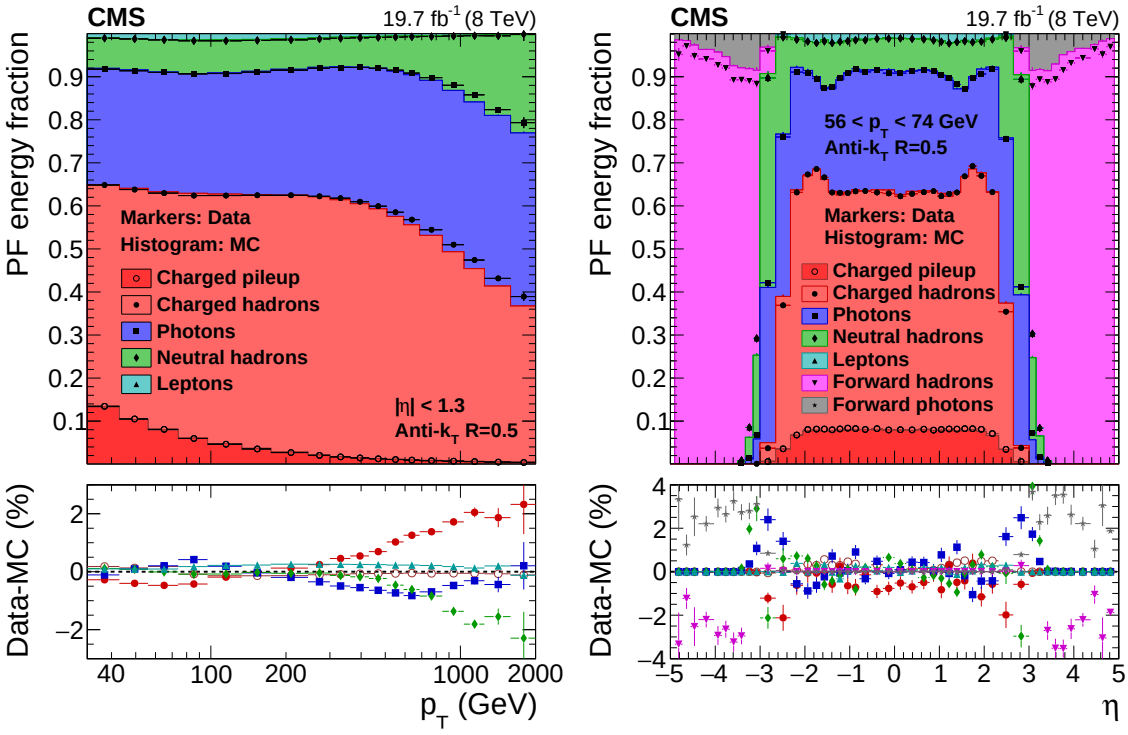

Figure 46. PF jet composition in data and simulation versus p_T at $|\eta| < 1.3$ (left), and versus η at $56 < p_T < 74$ GeV (right).

Interpretation of the results

To interpret the implications for JEC of composition differences in data and simulation, we can start from the definition of the jet response, in the absence of pileup, and in bins of particle-level jet $p_{T,\,ptcl}$ and reconstructed η (p_T is the reconstructed jet transverse momentum):

$$R(\langle p_T\rangle,\eta) \equiv \frac{\langle p_T\rangle}{\langle p_{T,\,ptcl}\rangle}[p_{T,\,ptcl},\eta] \cong \left\langle \frac{p_T}{p_{T,\,ptcl}} \right\rangle [p_{T,\,ptcl},\eta]. \tag{10.1}$$

The last equivalence holds if the $p_{T,\,ptcl}$ bins are narrow enough. Leaving aside corrections for overlapping particles caused, e.g., by calorimeter zero-suppression or neutral hadron shadowing in the PF algorithm, we can write

$$R(\langle p_T\rangle,\eta) = \frac{\langle \sum_i R_f(\langle p_T^i\rangle,\eta^i) p_{T,\,ptcl}^i\rangle}{p_{T,\,ptcl}}, \quad p_{T,\,ptcl} = \sum_i p_{T,\,ptcl}^i, \tag{10.2}$$

where the sum runs over all stable ($c\tau > 1$ cm) particles i of different particle species f, excluding neutrinos. Figure 47 illustrates the average particle jet composition in QCD dijet sample versus p_T at $|\eta| < 1.3$, which is about 60% charged hadrons (red hues), 15% neutral hadrons (green hues) and 25% photons (blue hues). About 65% of the jet energy is carried by pions (π^+, π^-, $\pi^0 \to \gamma\gamma$). The nucleons (p, $\overline{\text{p}}$, n, $\overline{\text{n}}$) and kaons (K^+, K^-, K_L^0, K_S^0) carry about 15% each, with the remaining 5% in fragmentation photons (γ), lambda (Λ^0), and sigma (Σ^0) baryons, leptons (e, μ) and other particles. The composition does not significantly depend on η.

2017 JINST 12 P02014

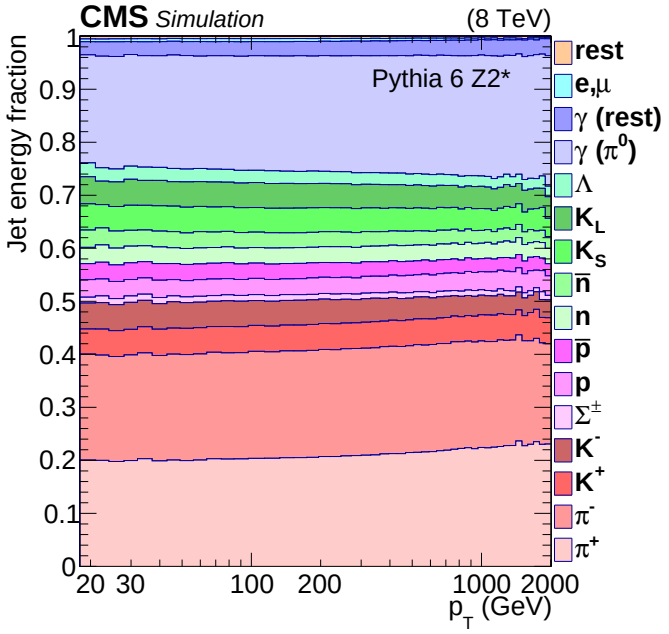

Figure 47. Jet composition at particle level in the PYTHIA 6.4 tune Z2* for QCD dijet sample, shown versus p_T at $|\eta| < 1.3$. The component labeled 'γ (rest)' denotes all photons not coming from π^0s, and the component labeled 'rest' refers to all particles not listed specifically.

The PF algorithm [10, 11] uses tracking to measure charged particles p_T down to $p_T \approx 0.3$ GeV, which effectively results in response $R_{ch}(p_T) \approx 1$ for all charged particles (charged hadrons, electron, muons) within the tracking coverage at $|\eta| < 2.4$, when neglecting tracking inefficiencies and the low p_T acceptance. The finely segmented ECAL has a linear response to photons down to its acceptance of about 0.1 GeV, which also results in response $R_\gamma \approx 1$.

Neutral hadrons (predominantly n, K^0_L, Λ^0), hadrons outside the tracking coverage, and hadrons with failed tracking (e.g., K^0_S decaying in the outer layers of tracking, or unreconstructed nuclear interactions within the tracker) are reconstructed with a nonlinear calorimeter response $R_{calo}(p_T) \approx 1 - a p_T^{m-1}$ [53] separately in the ECAL (as PF photons) and the HCAL (as PF neutral hadrons). For particles with $|\eta| > 2.5$, overlapping ECAL and HCAL energy deposits are linked to build neutral hadrons. The combination of the HCAL reconstruction threshold of $p_T > 0.8$ GeV, the low response of $R_{calo} \approx 0.3$ for soft hadrons, and many neutral hadrons showering early in ECAL, result in an effective neutral hadron response $R_{nh} \ll 1$ at low p_T despite the PF neutral hadron calibration for HCAL deposits. However, the neutral hadron response approaches unity asymptotically at high p_T.

Rearranging eq. (10.2) in terms of the main particle categories seen by the detector gives

$$R_{jet} = f_{ch} R_{ch} + f_\gamma R_\gamma + f_{nh} R_{nh}, \tag{10.3}$$

where f_i are the average fractions of energy carried by each particle category at particle level, such that $\sum_i f_i = 1$. The effective categories are charged hadrons+electrons+muons (ch), photons (γ), and neutral hadrons (nh). These effective categories have some ambiguity in the classification of, e.g., $K^0_S \to \pi^+ + \pi^-$ and $K^0_S \to \pi^0 + \pi^0$ decays within the tracker volume. Typical generated fractions are $f_{ch} \approx 60\%$, $f_\gamma \approx 25\%$, and $f_{nh} \approx 15\%$. These values differ slightly from typical measured

fractions $f_{\text{ch, meas}} \approx 65\%$, $f_{\gamma,\text{meas}} \approx 30\%$, and $f_{\text{nh,meas}} \approx 5\%$ due to different detector responses ($R_{\text{ch}} \approx R_{\gamma} \approx 1$, $R_{\text{nh}} \approx 0.6$, thus $R_{\text{jet}} \approx 0.95$) and ambiguities in particle identification, specially between neutral hadrons and photons.

The impact of typical detector mismodeling effects can be estimated with the help of eq. (10.3). A change of -1% in the charged hadron fraction through tracking inefficiencies would result in a corresponding but smaller increase of the neutral hadron fraction, for a total relative jet response variation of -0.4%. A variation of -1% of the ECAL scale in data would change the relative jet response by -0.3%, while a variation of the single-pion response of -3% would also change it by -0.3%.

Adding these *a priori* uncertainty estimates in quadrature gives 0.6%, while summing them up gives -1.0%. Incidentally, these are about the order of magnitude of the minimum energy scale uncertainty and the data/MC correction applied at the moment in the reference region $|\eta| < 1.3$. The PF energy fractions between data and simulation in figure 46 are in almost perfect agreement to the level of about 10^{-3} at $p_{\text{T}} \approx 200\,\text{GeV}$, which is consistent with the jet response difference of -1%, assuming the inefficiencies for charged hadrons, photons, and neutral hadrons all go in the same direction.

The corrections and uncertainties increase outside the tracking coverage at $|\eta| > 2.5$, where effectively $f_{\text{ch}} = 0$ and $f_{\text{nh}} = 75\%$, resulting in about five times higher sensitivity to single-pion response and threshold effects in R_{nh}.

11 Conclusions

The understanding of jet energy scale and resolution achieved by the CMS experiment exploiting the pp data taken at 8 TeV, corresponding to an integrated luminosity of $19.7\,\text{fb}^{-1}$, has been documented. The CMS strategy involves the sequential correction of the jets for the pileup offset, simulated response, and residual η and p_{T} dependencies in data with respect to simulation, with optional corrections depending on the jet flavor.

The pileup offset corrections are determined from QCD dijet simulations processed with and without pileup overlay, with additional corrections for residual differences between data and detector simulation, extracted using the random-cone method in zero-bias events. The simulated jet response corrections are determined from a Monte Carlo event sample, as a function of jet p_{T} and η, for various jet algorithms and distance parameter sizes. The η-dependent corrections for residual differences between data and MC simulation are determined with dijet events, relative to a jet in the central region $|\eta| < 1.3$. The p_{T}-dependent corrections for residual differences within $|\eta| < 1.3$ at $30 < p_{\text{T}} < 800\,\text{GeV}$ are measured combining photon+jet, $\text{Z}(\rightarrow \mu\mu)$+jet, and $\text{Z}(\rightarrow \text{ee})$+jet events. The p_{T} dependence at $p_{\text{T}} > 800\,\text{GeV}$ is directly constrained with multijet events. The optional jet-flavor corrections are derived from MC simulation and checked for b jets.

The simulated jet p_{T} resolution is determined, as a function of jet p_{T} and η, for different levels of pileup. The dependence of the resolution on the jet flavor is also studied. The η-dependent corrections for residual differences between data and MC simulation in the jet resolution are determined with both dijet and γ+jet events.

In all methods using MC simulation, the uncertainties arising from the modeling of jet radiation and hadronization are constrained from the study of the differences between PYTHIA 6.4 and HERWIG++ 2.3 generators. Detailed studies are performed to correct for biases in the data-based methods due to differences with respect to the MC simulation, in initial- and final-state radiation

2017 JINST 12 P02014

as well as in jet p_T resolution. The systematic uncertainties in the jet energy corrections, and their correlations, are provided as a function of η and p_T.

The final uncertainties on the jet energy scale are below 3% across the phase space considered by most analyses ($p_T > 30$ GeV and $|\eta| < 5.0$). In the barrel region we reach an uncertainty below 1% for $p_T > 30$ GeV, when excluding the jet-flavor uncertainties, provided separately for different jet-flavor mixtures. At its lowest, the core uncertainty (excluding optional time-dependent and flavor systematics) is 0.32% for jets with p_T between 165 and 330 GeV, and $|\eta| < 0.8$. These results set a new benchmark for jet energy scale determination at hadron colliders.

Acknowledgments

We congratulate our colleagues in the CERN accelerator departments for the excellent performance of the LHC and thank the technical and administrative staffs at CERN and at other CMS institutes for their contributions to the success of the CMS effort. In addition, we gratefully acknowledge the computing centers and personnel of the Worldwide LHC Computing Grid for delivering so effectively the computing infrastructure essential to our analyses. Finally, we acknowledge the enduring support for the construction and operation of the LHC and the CMS detector provided by the following funding agencies: the Austrian Federal Ministry of Science, Research and Economy and the Austrian Science Fund; the Belgian Fonds de la Recherche Scientifique, and Fonds voor Wetenschappelijk Onderzoek; the Brazilian Funding Agencies (CNPq, CAPES, FAPERJ, and FAPESP); the Bulgarian Ministry of Education and Science; CERN; the Chinese Academy of Sciences, Ministry of Science and Technology, and National Natural Science Foundation of China; the Colombian Funding Agency (COLCIENCIAS); the Croatian Ministry of Science, Education and Sport, and the Croatian Science Foundation; the Research Promotion Foundation, Cyprus; the Secretariat for Higher Education, Science, Technology and Innovation, Ecuador; the Ministry of Education and Research, Estonian Research Council via IUT23-4 and IUT23-6 and European Regional Development Fund, Estonia; the Academy of Finland, Finnish Ministry of Education and Culture, and Helsinki Institute of Physics; the Institut National de Physique Nucléaire et de Physique des Particules / CNRS, and Commissariat à l'Énergie Atomique et aux Énergies Alternatives / CEA, France; the Bundesministerium für Bildung und Forschung, Deutsche Forschungsgemeinschaft, and Helmholtz-Gemeinschaft Deutscher Forschungszentren, Germany; the General Secretariat for Research and Technology, Greece; the National Scientific Research Foundation, and National Innovation Office, Hungary; the Department of Atomic Energy and the Department of Science and Technology, India; the Institute for Studies in Theoretical Physics and Mathematics, Iran; the Science Foundation, Ireland; the Istituto Nazionale di Fisica Nucleare, Italy; the Ministry of Science, ICT and Future Planning, and National Research Foundation (NRF), Republic of Korea; the Lithuanian Academy of Sciences; the Ministry of Education, and University of Malaya (Malaysia); the Mexican Funding Agencies (BUAP, CINVESTAV, CONACYT, LNS, SEP, and UASLP-FAI); the Ministry of Business, Innovation and Employment, New Zealand; the Pakistan Atomic Energy Commission; the Ministry of Science and Higher Education and the National Science Centre, Poland; the Fundação para a Ciência e a Tecnologia, Portugal; JINR, Dubna; the Ministry of Education and Science of the Russian Federation, the Federal Agency of Atomic Energy of the Russian Federation, Russian Academy of Sciences, and the Russian Foundation for Basic Research; the Ministry of Education,

2017 JINST 12 P02014

Science and Technological Development of Serbia; the Secretaría de Estado de Investigación, Desarrollo e Innovación and Programa Consolider-Ingenio 2010, Spain; the Swiss Funding Agencies (ETH Board, ETH Zurich, PSI, SNF, UniZH, Canton Zurich, and SER); the Ministry of Science and Technology, Taipei; the Thailand Center of Excellence in Physics, the Institute for the Promotion of Teaching Science and Technology of Thailand, Special Task Force for Activating Research and the National Science and Technology Development Agency of Thailand; the Scientific and Technical Research Council of Turkey, and Turkish Atomic Energy Authority; the National Academy of Sciences of Ukraine, and State Fund for Fundamental Researches, Ukraine; the Science and Technology Facilities Council, U.K.; the U.S. Department of Energy, and the U.S. National Science Foundation.

Individuals have received support from the Marie-Curie program and the European Research Council and EPLANET (European Union); the Leventis Foundation; the A. P. Sloan Foundation; the Alexander von Humboldt Foundation; the Belgian Federal Science Policy Office; the Fonds pour la Formation à la Recherche dans l'Industrie et dans l'Agriculture (FRIA-Belgium); the Agentschap voor Innovatie door Wetenschap en Technologie (IWT-Belgium); the Ministry of Education, Youth and Sports (MEYS) of the Czech Republic; the Council of Science and Industrial Research, India; the HOMING PLUS program of the Foundation for Polish Science, cofinanced from European Union, Regional Development Fund, the Mobility Plus program of the Ministry of Science and Higher Education, the OPUS program contract 2014/13/B/ST2/02543 and contract Sonata-bis DEC-2012/07/E/ST2/01406 of the National Science Center (Poland); the Thalis and Aristeia programs cofinanced by EU-ESF and the Greek NSRF; the National Priorities Research Program by Qatar National Research Fund; the Programa Clarín-COFUND del Principado de Asturias; the Rachadapisek Sompot Fund for Postdoctoral Fellowship, Chulalongkorn University and the Chulalongkorn Academic into Its 2nd Century Project Advancement Project (Thailand); and the Welch Foundation, contract C-1845.

References

[1] CMS collaboration, *Measurements of differential jet cross sections in proton-proton collisions at* $\sqrt{s} = 7$ *TeV with the CMS detector*, *Phys. Rev.* **D 87** (2013) 112002 [*Erratum ibid.* **D 87** (2013) 119902] [arXiv:1212.6660].

[2] CMS collaboration, *Measurement of the inclusive jet cross section in pp collisions at* $\sqrt{s} = 7$ *TeV*, *Phys. Rev. Lett.* **107** (2011) 132001 [arXiv:1106.0208].

[3] CMS collaboration, *Measurement of the differential dijet production cross section in proton-proton collisions at* $\sqrt{s} = 7$ *TeV*, *Phys. Lett.* **B 700** (2011) 187 [arXiv:1104.1693].

[4] CMS collaboration, *Measurement of the ratio of inclusive jet cross sections using the anti-*k_T *algorithm with radius parameters* $R = 0.5$ *and* 0.7 *in pp collisions at* $\sqrt{s} = 7$ *TeV*, *Phys. Rev.* **D 90** (2014) 072006 [arXiv:1406.0324].

[5] CMS collaboration, *Distributions of topological observables in inclusive three- and four-jet events in pp collisions at* $\sqrt{s} = 7$ *TeV*, *Eur. Phys. J.* **C 75** (2015) 302 [arXiv:1502.04785].

[6] CMS collaboration, *Measurement of the top-quark mass in all-jets* $t\bar{t}$ *events in pp collisions at* $\sqrt{s} = 7$ *TeV*, *Eur. Phys. J.* **C 74** (2014) 2758 [arXiv:1307.4617].

2017 JINST 12 P02014

[7] CMS collaboration, *Determination of the top-quark pole mass and strong coupling constant from the $t\bar{t}$ production cross section in pp collisions at $\sqrt{s}$ = 7 TeV*, *Phys. Lett.* **B 728** (2014) 496 [*Erratum ibid.* **B 738** (2014) 526] [arXiv:1307.1907].

[8] CMS collaboration, *Measurement of the top-quark mass in $t\bar{t}$ events with lepton+jets final states in pp collisions at $\sqrt{s}$ = 7 TeV*, *JHEP* **12** (2012) 105 [arXiv:1209.2319].

[9] CMS collaboration, *Measurement of the top quark mass using proton-proton data at $\sqrt{s}$ = 7 and 8 TeV*, *Phys. Rev.* **D 93** (2016) 072004 [arXiv:1509.04044].

[10] CMS collaboration, *Particle-flow event reconstruction in CMS and performance for jets, taus and MET*, CMS-PAS-PFT-09-001, CERN, Geneva Switzerland, (2009).

[11] CMS collaboration, *Commissioning of the particle-flow event reconstruction with the first LHC collisions recorded in the CMS detector*, CMS-PAS-PFT-10-001, CERN, Geneva Switzerland, (2010).

[12] M. Cacciari, G.P. Salam and G. Soyez, *The anti-k_t jet clustering algorithm*, *JHEP* **04** (2008) 063 [arXiv:0802.1189].

[13] CMS collaboration, *Determination of jet energy calibration and transverse momentum resolution in CMS*, 2011 *JINST* **6** P11002 [arXiv:1107.4277].

[14] ATLAS collaboration, *Jet energy measurement with the ATLAS detector in proton-proton collisions at $\sqrt{s}$ = 7 TeV*, *Eur. Phys. J.* **C 73** (2013) 2304 [arXiv:1112.6426].

[15] CDF collaboration, A. Bhatti et al., *Determination of the jet energy scale at the collider detector at Fermilab*, *Nucl. Instrum. Meth.* **A 566** (2006) 375 [hep-ex/0510047].

[16] D0 collaboration, V.M. Abazov et al., *Jet energy scale determination in the D0 experiment*, *Nucl. Instrum. Meth.* **A 763** (2014) 442 [arXiv:1312.6873].

[17] ATLAS collaboration, *Jet energy measurement and its systematic uncertainty in proton-proton collisions at $\sqrt{s}$ = 7 TeV with the ATLAS detector*, *Eur. Phys. J.* **C 75** (2015) 17 [arXiv:1406.0076].

[18] GEANT4 collaboration, S. Agostinelli et al., *GEANT4: a simulation toolkit*, *Nucl. Instrum. Meth.* **A 506** (2003) 250.

[19] T. Sjöstrand, S. Mrenna and P.Z. Skands, *PYTHIA* 6.4 *physics and manual*, *JHEP* **05** (2006) 026 [hep-ph/0603175].

[20] CMS collaboration, *Event generator tunes obtained from underlying event and multiparton scattering measurements*, *Eur. Phys. J.* **C 76** (2016) 155 [arXiv:1512.00815].

[21] M. Bähr et al., *HERWIG++ physics and manual*, *Eur. Phys. J.* **C 58** (2008) 639 [arXiv:0803.0883].

[22] S. Gieseke, C. Rohr and A. Siodmok, *Colour reconnections in HERWIG++*, *Eur. Phys. J.* **C 72** (2012) 2225 [arXiv:1206.0041].

[23] A. Giammanco, *The fast simulation of the CMS experiment*, *J. Phys. Conf. Ser.* **513** (2014) 022012.

[24] CMS collaboration, *The CMS experiment at the CERN LHC*, 2008 *JINST* **3** S08004.

[25] J. Alwall, M. Herquet, F. Maltoni, O. Mattelaer and T. Stelzer, *MadGraph 5: going beyond*, *JHEP* **06** (2011) 128 [arXiv:1106.0522].

[26] S. Frixione, P. Nason and C. Oleari, *Matching NLO QCD computations with parton shower simulations: the POWHEG method*, *JHEP* **11** (2007) 070 [arXiv:0709.2092].

[27] CMS collaboration, *Description and performance of track and primary-vertex reconstruction with the CMS tracker*, 2014 *JINST* **9** P10009 [arXiv:1405.6569].

2017 JINST 12 P02014

[28] CMS collaboration, *Jet performance in pp collisions at* 7 *TeV*, CMS-PAS-JME-10-003, CERN, Geneva Switzerland, (2010).

[29] CMS collaboration, *Performance of CMS muon reconstruction in pp collision events at* $\sqrt{s} = 7$ *TeV*, 2012 *JINST* **7** P10002 [arXiv:1206.4071].

[30] CMS collaboration, *Performance of electron reconstruction and selection with the CMS detector in proton-proton collisions at* $\sqrt{s} = 8$ *TeV*, 2015 *JINST* **10** P06005 [arXiv:1502.02701].

[31] CMS collaboration, *Identification of b-quark jets with the CMS experiment*, 2013 *JINST* **8** P04013 [arXiv:1211.4462].

[32] CMS collaboration, *Performance of photon reconstruction and identification with the CMS detector in proton-proton collisions at* $\sqrt{s} = 8$ *TeV*, 2015 *JINST* **10** P08010 [arXiv:1502.02702].

[33] M. Cacciari, G.P. Salam and G. Soyez, *FastJet user manual*, *Eur. Phys. J.* **C 72** (2012) 1896 [arXiv:1111.6097].

[34] M. Cacciari and G.P. Salam, *Dispelling the* N^3 *myth for the* k_t *jet-finder*, *Phys. Lett.* **B 641** (2006) 57 [hep-ph/0512210].

[35] S. Catani, Y.L. Dokshitzer and B.R. Webber, *The* $k_\perp$*-clustering algorithm for jets in deep inelastic scattering and hadron collisions*, *Phys. Lett.* **B 285** (1992) 291.

[36] S. Catani, Y.L. Dokshitzer, M.H. Seymour and B.R. Webber, *Longitudinally invariant* $k_\perp$ *clustering algorithms for hadron hadron collisions*, *Nucl. Phys.* **B 406** (1993) 187.

[37] S.D. Ellis and D.E. Soper, *Successive combination jet algorithm for hadron collisions*, *Phys. Rev.* **D 48** (1993) 3160 [hep-ph/9305266].

[38] M. Cacciari and G.P. Salam, *Pileup subtraction using jet areas*, *Phys. Lett.* **B 659** (2008) 119 [arXiv:0707.1378].

[39] CMS collaboration, *Measurement of the inelastic proton-proton cross section at* $\sqrt{s} = 7$ *TeV*, *Phys. Lett.* **B 722** (2013) 5 [arXiv:1210.6718].

[40] CMS collaboration, *CMS luminosity based on pixel cluster counting — Summer* 2013 *update*, CMS-PAS-LUM-13-001, CERN, Geneva Switzerland, (2013).

[41] CMS collaboration, *CMS technical design report, volume II: physics performance*, *J. Phys.* **G 34** (2007) 995.

[42] CMS collaboration, *Transverse-momentum and pseudorapidity distributions of charged hadrons in pp collisions at* $\sqrt{s} = 7$ *TeV*, *Phys. Rev. Lett.* **105** (2010) 022002 [arXiv:1005.3299].

[43] D. Bertolini, P. Harris, M. Low and N. Tran, *Pileup per particle identification*, *JHEP* **10** (2014) 059 [arXiv:1407.6013].

[44] CMS collaboration, *Pileup jet identification*, CMS-PAS-JME-13-005, CERN, Geneva Switzerland, (2013).

[45] CMS collaboration, *Measurement of the underlying event activity in pp collisions at* $\sqrt{s} = 0.9$ *and* 7 *TeV with the novel jet-area/median approach*, *JHEP* **08** (2012) 130 [arXiv:1207.2392].

[46] CMS collaboration, *Jet energy scale performance in* 2011, CMS-DP-2012-006, CERN, Geneva Switzerland, (2012).

[47] CMS collaboration, *Single-particle response in the CMS calorimeters*, CMS-PAS-JME-10-008, CERN, Geneva Switzerland, (2010).

2017 JINST 12 P02014

[48] CMS collaboration, *Energy calibration and resolution of the CMS electromagnetic calorimeter in pp collisions at* $\sqrt{s} = 7$ *TeV*, 2013 *JINST* **8** P09009 [arXiv:1306.2016].

[49] CMS collaboration, *Performance of quark/gluon discrimination in* 8 *TeV pp data*, CMS-PAS-JME-13-002, CERN, Geneva Switzerland, (2013).

[50] CMS collaboration, *Calculation of residual energy correction for b jets using* $Z + b$ *events in* 8 *TeV pp collisions*, CMS-PAS-JME-13-001, CERN, Geneva Switzerland, (2013).

[51] M.J. Oreglia, *A study of the reactions* $\psi' \to \gamma\gamma\psi$, see appendix D, SLAC report SLAC-R-236, Ph.D. thesis, Stanford University, U.S.A., (1980).

[52] H.L. Lai et al., *Global QCD analysis and the CTEQ parton distributions*, *Phys. Rev.* **D 51** (1995) 4763 [hep-ph/9410404].

[53] D.E. Groom, *A simplistic view of hadron calorimetry*, *AIP Conf. Proc.* **896** (2007) 137.

2017 JINST 12 P02014

The CMS collaboration

Yerevan Physics Institute, Yerevan, Armenia

V. Khachatryan, A.M. Sirunyan, A. Tumasyan

Institut für Hochenergiephysik der OeAW, Wien, Austria

W. Adam, E. Asilar, T. Bergauer, J. Brandstetter, E. Brondolin, M. Dragicevic, J. Erö, M. Flechl, M. Friedl, R. Frühwirth[1], V.M. Ghete, C. Hartl, N. Hörmann, J. Hrubec, M. Jeitler[1], V. Knünz, A. König, M. Krammer[1], I. Krätschmer, D. Liko, T. Matsushita, I. Mikulec, D. Rabady[2], B. Rahbaran, H. Rohringer, J. Schieck[1], R. Schöfbeck, J. Strauss, W. Treberer-Treberspurg, W. Waltenberger, C.-E. Wulz[1]

National Centre for Particle and High Energy Physics, Minsk, Belarus

V. Mossolov, N. Shumeiko, J. Suarez Gonzalez

Universiteit Antwerpen, Antwerpen, Belgium

S. Alderweireldt, T. Cornelis, E.A. De Wolf, X. Janssen, A. Knutsson, J. Lauwers, S. Luyckx, M. Van De Klundert, H. Van Haevermaet, P. Van Mechelen, N. Van Remortel, A. Van Spilbeeck

Vrije Universiteit Brussel, Brussel, Belgium

S. Abu Zeid, F. Blekman, J. D'Hondt, N. Daci, I. De Bruyn, K. Deroover, N. Heracleous, J. Keaveney, S. Lowette, L. Moreels, A. Olbrechts, Q. Python, D. Strom, S. Tavernier, W. Van Doninck, P. Van Mulders, G.P. Van Onsem, I. Van Parijs

Université Libre de Bruxelles, Bruxelles, Belgium

P. Barria, H. Brun, C. Caillol, B. Clerbaux, G. De Lentdecker, G. Fasanella, L. Favart, A. Grebenyuk, G. Karapostoli, T. Lenzi, A. Léonard, T. Maerschalk, A. Marinov, L. Perniè, A. Randle-conde, T. Reis, T. Seva, C. Vander Velde, P. Vanlaer, R. Yonamine, F. Zenoni, F. Zhang[3]

Ghent University, Ghent, Belgium

K. Beernaert, L. Benucci, A. Cimmino, S. Crucy, D. Dobur, A. Fagot, G. Garcia, M. Gul, J. Mccartin, A.A. Ocampo Rios, D. Poyraz, D. Ryckbosch, S. Salva, M. Sigamani, N. Strobbe, M. Tytgat, W. Van Driessche, E. Yazgan, N. Zaganidis

Université Catholique de Louvain, Louvain-la-Neuve, Belgium

S. Basegmez, C. Beluffi[4], O. Bondu, S. Brochet, G. Bruno, A. Caudron, L. Ceard, G.G. Da Silveira, C. Delaere, D. Favart, L. Forthomme, A. Giammanco[5], J. Hollar, A. Jafari, P. Jez, M. Komm, V. Lemaitre, A. Mertens, C. Nuttens, L. Perrini, A. Pin, K. Piotrzkowski, A. Popov[6], L. Quertenmont, M. Selvaggi, M. Vidal Marono

Université de Mons, Mons, Belgium

N. Beliy, G.H. Hammad

Centro Brasileiro de Pesquisas Fisicas, Rio de Janeiro, Brazil

W.L. Aldá Júnior, F.L. Alves, G.A. Alves, L. Brito, M. Correa Martins Junior, M. Hamer, C. Hensel, C. Mora Herrera, A. Moraes, M.E. Pol, P. Rebello Teles

2017 JINST 12 P02014

Universidade do Estado do Rio de Janeiro, Rio de Janeiro, Brazil
E. Belchior Batista Das Chagas, W. Carvalho, J. Chinellato[7], A. Custódio, E.M. Da Costa, D. De Jesus Damiao, C. De Oliveira Martins, S. Fonseca De Souza, L.M. Huertas Guativa, H. Malbouisson, D. Matos Figueiredo, L. Mundim, H. Nogima, W.L. Prado Da Silva, A. Santoro, A. Sznajder, E.J. Tonelli Manganote[7], A. Vilela Pereira

Universidade Estadual Paulista [a], Universidade Federal do ABC [b], São Paulo, Brazil
S. Ahuja[a], C.A. Bernardes[b], A. De Souza Santos[b], S. Dogra[a], T.R. Fernandez Perez Tomei[a], E.M. Gregores[b], P.G. Mercadante[b], C.S. Moon[a,8], S.F. Novaes[a], Sandra S. Padula[a], D. Romero Abad, J.C. Ruiz Vargas

Institute for Nuclear Research and Nuclear Energy, Sofia, Bulgaria
A. Aleksandrov, R. Hadjiiska, P. Iaydjiev, M. Rodozov, S. Stoykova, G. Sultanov, M. Vutova

University of Sofia, Sofia, Bulgaria
A. Dimitrov, I. Glushkov, L. Litov, B. Pavlov, P. Petkov

Institute of High Energy Physics, Beijing, China
M. Ahmad, J.G. Bian, G.M. Chen, H.S. Chen, M. Chen, T. Cheng, R. Du, C.H. Jiang, R. Plestina[9], F. Romeo, S.M. Shaheen, J. Tao, C. Wang, Z. Wang, H. Zhang

State Key Laboratory of Nuclear Physics and Technology, Peking University, Beijing, China
C. Asawatangtrakuldee, Y. Ban, Q. Li, S. Liu, Y. Mao, S.J. Qian, D. Wang, Z. Xu

Universidad de Los Andes, Bogota, Colombia
C. Avila, A. Cabrera, L.F. Chaparro Sierra, C. Florez, J.P. Gomez, B. Gomez Moreno, J.C. Sanabria

University of Split, Faculty of Electrical Engineering, Mechanical Engineering and Naval Architecture, Split, Croatia
N. Godinovic, D. Lelas, I. Puljak, P.M. Ribeiro Cipriano

University of Split, Faculty of Science, Split, Croatia
Z. Antunovic, M. Kovac

Institute Rudjer Boskovic, Zagreb, Croatia
V. Brigljevic, K. Kadija, J. Luetic, S. Micanovic, L. Sudic

University of Cyprus, Nicosia, Cyprus
A. Attikis, G. Mavromanolakis, J. Mousa, C. Nicolaou, F. Ptochos, P.A. Razis, H. Rykaczewski

Charles University, Prague, Czech Republic
M. Bodlak, M. Finger[10], M. Finger Jr.[10]

Academy of Scientific Research and Technology of the Arab Republic of Egypt, Egyptian Network of High Energy Physics, Cairo, Egypt
Y. Assran[11], S. Elgammal[12], A. Ellithi Kamel[13], M.A. Mahmoud[14], Y. Mohammed[14]

National Institute of Chemical Physics and Biophysics, Tallinn, Estonia
B. Calpas, M. Kadastik, M. Murumaa, M. Raidal, A. Tiko, C. Veelken

2017 JINST 12 P02014

Department of Physics, University of Helsinki, Helsinki, Finland
P. Eerola, J. Pekkanen, M. Voutilainen

Helsinki Institute of Physics, Helsinki, Finland
J. Härkönen, V. Karimäki, R. Kinnunen, T. Lampén, K. Lassila-Perini, S. Lehti, T. Lindén, P. Luukka, T. Mäenpää, T. Peltola, E. Tuominen, J. Tuominiemi, E. Tuovinen, L. Wendland

Lappeenranta University of Technology, Lappeenranta, Finland
J. Talvitie, T. Tuuva

IRFU, CEA, Université Paris-Saclay, Gif-sur-Yvette, France
M. Besancon, F. Couderc, M. Dejardin, D. Denegri, B. Fabbro, J.L. Faure, C. Favaro, F. Ferri, S. Ganjour, A. Givernaud, P. Gras, G. Hamel de Monchenault, P. Jarry, E. Locci, M. Machet, J. Malcles, J. Rander, A. Rosowsky, M. Titov, A. Zghiche

Laboratoire Leprince-Ringuet, Ecole Polytechnique, IN2P3-CNRS, Palaiseau, France
I. Antropov, S. Baffioni, F. Beaudette, P. Busson, L. Cadamuro, E. Chapon, C. Charlot, T. Dahms, O. Davignon, N. Filipovic, A. Florent, R. Granier de Cassagnac, S. Lisniak, L. Mastrolorenzo, P. Miné, I.N. Naranjo, M. Nguyen, C. Ochando, G. Ortona, P. Paganini, P. Pigard, S. Regnard, R. Salerno, J.B. Sauvan, Y. Sirois, T. Strebler, Y. Yilmaz, A. Zabi

Institut Pluridisciplinaire Hubert Curien, Université de Strasbourg, Université de Haute Alsace Mulhouse, CNRS/IN2P3, Strasbourg, France
J.-L. Agram[15], J. Andrea, A. Aubin, D. Bloch, J.-M. Brom, M. Buttignol, E.C. Chabert, N. Chanon, C. Collard, E. Conte[15], X. Coubez, J.-C. Fontaine[15], D. Gelé, U. Goerlach, C. Goetzmann, A.-C. Le Bihan, J.A. Merlin[2], K. Skovpen, P. Van Hove

Centre de Calcul de l'Institut National de Physique Nucleaire et de Physique des Particules, CNRS/IN2P3, Villeurbanne, France
S. Gadrat

Université de Lyon, Université Claude Bernard Lyon 1, CNRS-IN2P3, Institut de Physique Nucléaire de Lyon, Villeurbanne, France
S. Beauceron, C. Bernet, G. Boudoul, E. Bouvier, C.A. Carrillo Montoya, R. Chierici, D. Contardo, B. Courbon, P. Depasse, H. El Mamouni, J. Fan, J. Fay, S. Gascon, M. Gouzevitch, B. Ille, F. Lagarde, I.B. Laktineh, M. Lethuillier, L. Mirabito, A.L. Pequegnot, S. Perries, J.D. Ruiz Alvarez, D. Sabes, L. Sgandurra, V. Sordini, M. Vander Donckt, P. Verdier, S. Viret

Georgian Technical University, Tbilisi, Georgia
T. Toriashvili[16]

Tbilisi State University, Tbilisi, Georgia
Z. Tsamalaidze[10]

RWTH Aachen University, I. Physikalisches Institut, Aachen, Germany
C. Autermann, S. Beranek, M. Edelhoff, L. Feld, A. Heister, M.K. Kiesel, K. Klein, M. Lipinski, A. Ostapchuk, M. Preuten, F. Raupach, S. Schael, J.F. Schulte, T. Verlage, H. Weber, B. Wittmer, V. Zhukov[6]

2017 JINST 12 P02014

RWTH Aachen University, III. Physikalisches Institut A, Aachen, Germany

M. Ata, M. Brodski, E. Dietz-Laursonn, D. Duchardt, M. Endres, M. Erdmann, S. Erdweg, T. Esch, R. Fischer, A. Güth, T. Hebbeker, C. Heidemann, K. Hoepfner, D. Klingebiel, S. Knutzen, P. Kreuzer, M. Merschmeyer, A. Meyer, P. Millet, M. Olschewski, K. Padeken, P. Papacz, T. Pook, M. Radziej, H. Reithler, M. Rieger, F. Scheuch, L. Sonnenschein, D. Teyssier, S. Thüer

RWTH Aachen University, III. Physikalisches Institut B, Aachen, Germany

V. Cherepanov, Y. Erdogan, G. Flügge, H. Geenen, M. Geisler, F. Hoehle, B. Kargoll, T. Kress, Y. Kuessel, A. Künsken, J. Lingemann[2], A. Nehrkorn, A. Nowack, I.M. Nugent, C. Pistone, O. Pooth, A. Stahl

Deutsches Elektronen-Synchrotron, Hamburg, Germany

M. Aldaya Martin, I. Asin, N. Bartosik, O. Behnke, U. Behrens, A.J. Bell, K. Borras[17], A. Burgmeier, A. Cakir, L. Calligaris, A. Campbell, S. Choudhury, F. Costanza, C. Diez Pardos, G. Dolinska, S. Dooling, T. Dorland, G. Eckerlin, D. Eckstein, T. Eichhorn, G. Flucke, E. Gallo[18], J. Garay Garcia, A. Geiser, A. Gizhko, P. Gunnellini, J. Hauk, M. Hempel[19], H. Jung, A. Kalogeropoulos, O. Karacheban[19], M. Kasemann, P. Katsas, J. Kieseler, C. Kleinwort, I. Korol, W. Lange, J. Leonard, K. Lipka, A. Lobanov, W. Lohmann[19], R. Mankel, I. Marfin[19], I.-A. Melzer-Pellmann, A.B. Meyer, G. Mittag, J. Mnich, A. Mussgiller, S. Naumann-Emme, A. Nayak, E. Ntomari, H. Perrey, D. Pitzl, R. Placakyte, A. Raspereza, B. Roland, M.Ö. Sahin, P. Saxena, T. Schoerner-Sadenius, M. Schröder, C. Seitz, S. Spannagel, K.D. Trippkewitz, R. Walsh, C. Wissing

University of Hamburg, Hamburg, Germany

V. Blobel, M. Centis Vignali, A.R. Draeger, J. Erfle, E. Garutti, K. Goebel, D. Gonzalez, M. Görner, J. Haller, M. Hoffmann, R.S. Höing, A. Junkes, R. Klanner, R. Kogler, T. Lapsien, T. Lenz, I. Marchesini, D. Marconi, M. Meyer, D. Nowatschin, J. Ott, F. Pantaleo[2], T. Peiffer, A. Perieanu, N. Pietsch, J. Poehlsen, D. Rathjens, C. Sander, H. Schettler, P. Schleper, E. Schlieckau, A. Schmidt, J. Schwandt, M. Seidel, V. Sola, H. Stadie, G. Steinbrück, H. Tholen, D. Troendle, E. Usai, L. Vanelderen, A. Vanhoefer, B. Vormwald

Institut für Experimentelle Kernphysik, Karlsruhe, Germany

M. Akbiyik, C. Barth, C. Baus, J. Berger, C. Böser, E. Butz, T. Chwalek, F. Colombo, W. De Boer, A. Descroix, A. Dierlamm, S. Fink, F. Frensch, M. Giffels, A. Gilbert, D. Haitz, F. Hartmann[2], S.M. Heindl, U. Husemann, I. Katkov[6], A. Kornmayer[2], P. Lobelle Pardo, B. Maier, H. Mildner, M.U. Mozer, T. Müller, Th. Müller, M. Plagge, G. Quast, K. Rabbertz, S. Röcker, F. Roscher, H.J. Simonis, F.M. Stober, R. Ulrich, J. Wagner-Kuhr, S. Wayand, M. Weber, T. Weiler, C. Wöhrmann, R. Wolf

Institute of Nuclear and Particle Physics (INPP), NCSR Demokritos, Aghia Paraskevi, Greece

G. Anagnostou, G. Daskalakis, T. Geralis, V.A. Giakoumopoulou, A. Kyriakis, D. Loukas, A. Psallidas, I. Topsis-Giotis

National and Kapodistrian University of Athens, Athens, Greece

A. Agapitos, S. Kesisoglou, A. Panagiotou, N. Saoulidou, E. Tziaferi

2017 JINST 12 P02014

University of Ioánnina, Ioánnina, Greece

I. Evangelou, G. Flouris, C. Foudas, P. Kokkas, N. Loukas, N. Manthos, I. Papadopoulos, E. Paradas, J. Strologas

Wigner Research Centre for Physics, Budapest, Hungary

G. Bencze, C. Hajdu, A. Hazi, P. Hidas, D. Horvath[20], F. Sikler, V. Veszpremi, G. Vesztergombi[21], A.J. Zsigmond

Institute of Nuclear Research ATOMKI, Debrecen, Hungary

N. Beni, S. Czellar, J. Karancsi[22], J. Molnar, Z. Szillasi

University of Debrecen, Debrecen, Hungary

M. Bartók[23], A. Makovec, P. Raics, Z.L. Trocsanyi, B. Ujvari

National Institute of Science Education and Research, Bhubaneswar, India

P. Mal, K. Mandal, D.K. Sahoo, N. Sahoo, S.K. Swain

Panjab University, Chandigarh, India

S. Bansal, S.B. Beri, V. Bhatnagar, R. Chawla, R. Gupta, U.Bhawandeep, A.K. Kalsi, A. Kaur, M. Kaur, R. Kumar, A. Mehta, M. Mittal, J.B. Singh, G. Walia

University of Delhi, Delhi, India

Ashok Kumar, A. Bhardwaj, B.C. Choudhary, R.B. Garg, A. Kumar, S. Malhotra, M. Naimuddin, N. Nishu, K. Ranjan, R. Sharma, V. Sharma

Saha Institute of Nuclear Physics, Kolkata, India

S. Bhattacharya, K. Chatterjee, S. Dey, S. Dutta, Sa. Jain, N. Majumdar, A. Modak, K. Mondal, S. Mukherjee, S. Mukhopadhyay, A. Roy, D. Roy, S. Roy Chowdhury, S. Sarkar, M. Sharan

Bhabha Atomic Research Centre, Mumbai, India

A. Abdulsalam, R. Chudasama, D. Dutta, V. Jha, V. Kumar, A.K. Mohanty[2], L.M. Pant, P. Shukla, A. Topkar

Tata Institute of Fundamental Research, Mumbai, India

T. Aziz, S. Banerjee, S. Bhowmik[24], R.M. Chatterjee, R.K. Dewanjee, S. Dugad, S. Ganguly, S. Ghosh, M. Guchait, A. Gurtu[25], G. Kole, S. Kumar, B. Mahakud, M. Maity[24], G. Majumder, K. Mazumdar, S. Mitra, G.B. Mohanty, B. Parida, T. Sarkar[24], N. Sur, B. Sutar, N. Wickramage[26]

Indian Institute of Science Education and Research (IISER), Pune, India

S. Chauhan, S. Dube, S. Sharma

Institute for Research in Fundamental Sciences (IPM), Tehran, Iran

H. Bakhshiansohi, H. Behnamian, S.M. Etesami[27], A. Fahim[28], R. Goldouzian, M. Khakzad, M. Mohammadi Najafabadi, M. Naseri, S. Paktinat Mehdiabadi, F. Rezaei Hosseinabadi, B. Safarzadeh[29], M. Zeinali

University College Dublin, Dublin, Ireland

M. Felcini, M. Grunewald

2017 JINST 12 P02014

INFN Sezione di Bari [a], Università di Bari [b], Politecnico di Bari [c], Bari, Italy

M. Abbrescia[a,b], C. Calabria[a,b], C. Caputo[a,b], A. Colaleo[a], D. Creanza[a,c], L. Cristella[a,b], N. De Filippis[a,c], M. De Palma[a,b], L. Fiore[a], G. Iaselli[a,c], G. Maggi[a,c], M. Maggi[a], G. Miniello[a,b], S. My[a,c], S. Nuzzo[a,b], A. Pompili[a,b], G. Pugliese[a,c], R. Radogna[a,b], A. Ranieri[a], G. Selvaggi[a,b], L. Silvestris[a,2], R. Venditti[a,b], P. Verwilligen[a]

INFN Sezione di Bologna [a], Università di Bologna [b], Bologna, Italy

G. Abbiendi[a], C. Battilana[2], A.C. Benvenuti[a], D. Bonacorsi[a,b], S. Braibant-Giacomelli[a,b], L. Brigliadori[a,b], R. Campanini[a,b], P. Capiluppi[a,b], A. Castro[a,b], F.R. Cavallo[a], S.S. Chhibra[a,b], G. Codispoti[a,b], M. Cuffiani[a,b], G.M. Dallavalle[a], F. Fabbri[a], A. Fanfani[a,b], D. Fasanella[a,b], P. Giacomelli[a], C. Grandi[a], L. Guiducci[a,b], S. Marcellini[a], G. Masetti[a], A. Montanari[a], F.L. Navarria[a,b], A. Perrotta[a], A.M. Rossi[a,b], T. Rovelli[a,b], G.P. Siroli[a,b], N. Tosi[a,b], R. Travaglini[a,b]

INFN Sezione di Catania [a], Università di Catania [b], Catania, Italy

G. Cappello[a], M. Chiorboli[a,b], S. Costa[a,b], F. Giordano[a,b], R. Potenza[a,b], A. Tricomi[a,b], C. Tuve[a,b]

INFN Sezione di Firenze [a], Università di Firenze [b], Firenze, Italy

G. Barbagli[a], V. Ciulli[a,b], C. Civinini[a], R. D'Alessandro[a,b], E. Focardi[a,b], S. Gonzi[a,b], V. Gori[a,b], P. Lenzi[a,b], M. Meschini[a], S. Paoletti[a], G. Sguazzoni[a], A. Tropiano[a,b], L. Viliani[a,b]

INFN Laboratori Nazionali di Frascati, Frascati, Italy

L. Benussi, S. Bianco, F. Fabbri, D. Piccolo, F. Primavera

INFN Sezione di Genova [a], Università di Genova [b], Genova, Italy

V. Calvelli[a,b], F. Ferro[a], M. Lo Vetere[a,b], M.R. Monge[a,b], E. Robutti[a], S. Tosi[a,b]

INFN Sezione di Milano-Bicocca [a], Università di Milano-Bicocca [b], Milano, Italy

L. Brianza, M.E. Dinardo[a,b], S. Fiorendi[a,b], S. Gennai[a], R. Gerosa[a,b], A. Ghezzi[a,b], P. Govoni[a,b], S. Malvezzi[a], R.A. Manzoni[a,b], B. Marzocchi[a,b,2], D. Menasce[a], L. Moroni[a], M. Paganoni[a,b], D. Pedrini[a], S. Ragazzi[a,b], N. Redaelli[a], T. Tabarelli de Fatis[a,b]

INFN Sezione di Napoli [a], Università di Napoli 'Federico II' [b], Napoli, Italy, Università della Basilicata [c], Potenza, Italy, Università G. Marconi [d], Roma, Italy

S. Buontempo[a], N. Cavallo[a,c], S. Di Guida[a,d,2], M. Esposito[a,b], F. Fabozzi[a,c], A.O.M. Iorio[a,b], G. Lanza[a], L. Lista[a], S. Meola[a,d,2], M. Merola[a], P. Paolucci[a,2], C. Sciacca[a,b], F. Thyssen

INFN Sezione di Padova [a], Università di Padova [b], Padova, Italy, Università di Trento [c], Trento, Italy

P. Azzi[a,2], N. Bacchetta[a], M. Bellato[a], L. Benato[a,b], D. Bisello[a,b], A. Boletti[a,b], A. Branca[a,b], R. Carlin[a,b], P. Checchia[a], M. Dall'Osso[a,b,2], T. Dorigo[a], U. Dosselli[a], F. Fanzago[a], F. Gasparini[a,b], U. Gasparini[a,b], F. Gonella[a], A. Gozzelino[a], K. Kanishchev[a,c], S. Lacaprara[a], G. Maron[a,30], J. Pazzini[a,b], N. Pozzobon[a,b], P. Ronchese[a,b], M. Tosi[a,b], S. Vanini[a,b], S. Ventura[a], M. Zanetti, A. Zucchetta[a,b,2], G. Zumerle[a,b]

2017 JINST 12 P02014

INFN Sezione di Pavia [a], Università di Pavia [b], Pavia, Italy

A. Braghieri[a], A. Magnani[a], P. Montagna[a,b], S.P. Ratti[a,b], V. Re[a], C. Riccardi[a,b], P. Salvini[a], I. Vai[a], P. Vitulo[a,b]

INFN Sezione di Perugia [a], Università di Perugia [b], Perugia, Italy

L. Alunni Solestizi[a,b], M. Biasini[a,b], G.M. Bilei[a], D. Ciangottini[a,b,2], L. Fanò[a,b], P. Lariccia[a,b], G. Mantovani[a,b], M. Menichelli[a], A. Saha[a], A. Santocchia[a,b], A. Spiezia[a,b]

INFN Sezione di Pisa [a], Università di Pisa [b], Scuola Normale Superiore di Pisa [c], Pisa, Italy

K. Androsov[a,31], P. Azzurri[a], G. Bagliesi[a], J. Bernardini[a], T. Boccali[a], G. Broccolo[a,c], R. Castaldi[a], M.A. Ciocci[a,31], R. Dell'Orso[a], S. Donato[a,c,2], G. Fedi, L. Foà[a,c†], A. Giassi[a], M.T. Grippo[a,31], F. Ligabue[a,c], T. Lomtadze[a], L. Martini[a,b], A. Messineo[a,b], F. Palla[a], A. Rizzi[a,b], A. Savoy-Navarro[a,32], A.T. Serban[a], P. Spagnolo[a], P. Squillacioti[a,31], R. Tenchini[a], G. Tonelli[a,b], A. Venturi[a], P.G. Verdini[a]

INFN Sezione di Roma [a], Università di Roma [b], Roma, Italy

L. Barone[a,b], F. Cavallari[a], G. D'imperio[a,b,2], D. Del Re[a,b], M. Diemoz[a], S. Gelli[a,b], C. Jorda[a], E. Longo[a,b], F. Margaroli[a,b], P. Meridiani[a], G. Organtini[a,b], R. Paramatti[a], F. Preiato[a,b], S. Rahatlou[a,b], C. Rovelli[a], F. Santanastasio[a,b], P. Traczyk[a,b,2]

INFN Sezione di Torino [a], Università di Torino [b], Torino, Italy, Università del Piemonte Orientale [c], Novara, Italy

N. Amapane[a,b], R. Arcidiacono[a,c,2], S. Argiro[a,b], M. Arneodo[a,c], R. Bellan[a,b], C. Biino[a], N. Cartiglia[a], M. Costa[a,b], R. Covarelli[a,b], A. Degano[a,b], N. Demaria[a], L. Finco[a,b,2], B. Kiani[a,b], C. Mariotti[a], S. Maselli[a], E. Migliore[a,b], V. Monaco[a,b], E. Monteil[a,b], M. Musich[a], M.M. Obertino[a,b], L. Pacher[a,b], N. Pastrone[a], M. Pelliccioni[a], G.L. Pinna Angioni[a,b], F. Ravera[a,b], A. Romero[a,b], M. Ruspa[a,c], R. Sacchi[a,b], A. Solano[a,b], A. Staiano[a], U. Tamponi[a]

INFN Sezione di Trieste [a], Università di Trieste [b], Trieste, Italy

S. Belforte[a], V. Candelise[a,b,2], M. Casarsa[a], F. Cossutti[a], G. Della Ricca[a,b], B. Gobbo[a], C. La Licata[a,b], M. Marone[a,b], A. Schizzi[a,b], A. Zanetti[a]

Kangwon National University, Chunchon, Korea

A. Kropivnitskaya, S.K. Nam

Kyungpook National University, Daegu, Korea

D.H. Kim, G.N. Kim, M.S. Kim, D.J. Kong, S. Lee, Y.D. Oh, A. Sakharov, D.C. Son

Chonbuk National University, Jeonju, Korea

J.A. Brochero Cifuentes, H. Kim, T.J. Kim[33]

Chonnam National University, Institute for Universe and Elementary Particles, Kwangju, Korea

S. Song

Korea University, Seoul, Korea

S. Choi, Y. Go, D. Gyun, B. Hong, M. Jo, H. Kim, Y. Kim, B. Lee, K. Lee, K.S. Lee, S. Lee, S.K. Park, Y. Roh

2017 JINST 12 P02014

Seoul National University, Seoul, Korea
H.D. Yoo

University of Seoul, Seoul, Korea
M. Choi, H. Kim, J.H. Kim, J.S.H. Lee, I.C. Park, G. Ryu, M.S. Ryu

Sungkyunkwan University, Suwon, Korea
Y. Choi, J. Goh, D. Kim, E. Kwon, J. Lee, I. Yu

Vilnius University, Vilnius, Lithuania
A. Juodagalvis, J. Vaitkus

National Centre for Particle Physics, Universiti Malaya, Kuala Lumpur, Malaysia
I. Ahmed, Z.A. Ibrahim, J.R. Komaragiri, M.A.B. Md Ali[34], F. Mohamad Idris[35], W.A.T. Wan Abdullah, M.N. Yusli

Centro de Investigacion y de Estudios Avanzados del IPN, Mexico City, Mexico
E. Casimiro Linares, H. Castilla-Valdez, E. De La Cruz-Burelo, I. Heredia-De La Cruz[36], A. Hernandez-Almada, R. Lopez-Fernandez, A. Sanchez-Hernandez

Universidad Iberoamericana, Mexico City, Mexico
S. Carrillo Moreno, F. Vazquez Valencia

Benemerita Universidad Autonoma de Puebla, Puebla, Mexico
I. Pedraza, H.A. Salazar Ibarguen

Universidad Autónoma de San Luis Potosí, San Luis Potosí, Mexico
A. Morelos Pineda

University of Auckland, Auckland, New Zealand
D. Krofcheck

University of Canterbury, Christchurch, New Zealand
P.H. Butler

National Centre for Physics, Quaid-I-Azam University, Islamabad, Pakistan
A. Ahmad, M. Ahmad, Q. Hassan, H.R. Hoorani, W.A. Khan, T. Khurshid, M. Shoaib

National Centre for Nuclear Research, Swierk, Poland
H. Bialkowska, M. Bluj, B. Boimska, T. Frueboes, M. Górski, M. Kazana, K. Nawrocki, K. Romanowska-Rybinska, M. Szleper, P. Zalewski

Institute of Experimental Physics, Faculty of Physics, University of Warsaw, Warsaw, Poland
G. Brona, K. Bunkowski, A. Byszuk[37], K. Doroba, A. Kalinowski, M. Konecki, J. Krolikowski, M. Misiura, M. Olszewski, M. Walczak

Laboratório de Instrumentação e Física Experimental de Partículas, Lisboa, Portugal
P. Bargassa, C. Beirão Da Cruz E Silva, A. Di Francesco, P. Faccioli, P.G. Ferreira Parracho, M. Gallinaro, N. Leonardo, L. Lloret Iglesias, F. Nguyen, J. Rodrigues Antunes, J. Seixas, O. Toldaiev, D. Vadruccio, J. Varela, P. Vischia

2017 JINST 12 P02014

Joint Institute for Nuclear Research, Dubna, Russia

S. Afanasiev, P. Bunin, M. Gavrilenko, I. Golutvin, I. Gorbunov, A. Kamenev, V. Karjavin, V. Konoplyanikov, A. Lanev, A. Malakhov, V. Matveev[38], P. Moisenz, V. Palichik, V. Perelygin, S. Shmatov, S. Shulha, N. Skatchkov, V. Smirnov, A. Zarubin

Petersburg Nuclear Physics Institute, Gatchina (St. Petersburg), Russia

V. Golovtsov, Y. Ivanov, V. Kim[39], E. Kuznetsova, P. Levchenko, V. Murzin, V. Oreshkin, I. Smirnov, V. Sulimov, L. Uvarov, S. Vavilov, A. Vorobyev

Institute for Nuclear Research, Moscow, Russia

Yu. Andreev, A. Dermenev, S. Gninenko, N. Golubev, A. Karneyeu, M. Kirsanov, N. Krasnikov, A. Pashenkov, D. Tlisov, A. Toropin

Institute for Theoretical and Experimental Physics, Moscow, Russia

V. Epshteyn, V. Gavrilov, N. Lychkovskaya, V. Popov, I. Pozdnyakov, G. Safronov, A. Spiridonov, E. Vlasov, A. Zhokin

National Research Nuclear University 'Moscow Engineering Physics Institute' (MEPhI), Moscow, Russia

A. Bylinkin

P.N. Lebedev Physical Institute, Moscow, Russia

V. Andreev, M. Azarkin[40], I. Dremin[40], M. Kirakosyan, A. Leonidov[40], G. Mesyats, S.V. Rusakov

Skobeltsyn Institute of Nuclear Physics, Lomonosov Moscow State University, Moscow, Russia

A. Baskakov, A. Belyaev, E. Boos, M. Dubinin[41], L. Dudko, A. Ershov, A. Gribushin, A. Kaminskiy[42], V. Klyukhin, O. Kodolova, I. Lokhtin, I. Myagkov, S. Obraztsov, S. Petrushanko, V. Savrin

State Research Center of Russian Federation, Institute for High Energy Physics, Protvino, Russia

I. Azhgirey, I. Bayshev, S. Bitioukov, V. Kachanov, A. Kalinin, D. Konstantinov, V. Krychkine, V. Petrov, R. Ryutin, A. Sobol, L. Tourtchanovitch, S. Troshin, N. Tyurin, A. Uzunian, A. Volkov

University of Belgrade, Faculty of Physics and Vinca Institute of Nuclear Sciences, Belgrade, Serbia

P. Adzic[43], J. Milosevic, V. Rekovic

Centro de Investigaciones Energéticas Medioambientales y Tecnológicas (CIEMAT), Madrid, Spain

J. Alcaraz Maestre, E. Calvo, M. Cerrada, M. Chamizo Llatas, N. Colino, B. De La Cruz, A. Delgado Peris, D. Domínguez Vázquez, A. Escalante Del Valle, C. Fernandez Bedoya, J.P. Fernández Ramos, J. Flix, M.C. Fouz, P. Garcia-Abia, O. Gonzalez Lopez, S. Goy Lopez, J.M. Hernandez, M.I. Josa, E. Navarro De Martino, A. Pérez-Calero Yzquierdo, J. Puerta Pelayo, A. Quintario Olmeda, I. Redondo, L. Romero, J. Santaolalla, M.S. Soares

Universidad Autónoma de Madrid, Madrid, Spain

C. Albajar, J.F. de Trocóniz, M. Missiroli, D. Moran

2017 JINST 12 P02014

Universidad de Oviedo, Oviedo, Spain

J. Cuevas, J. Fernandez Menendez, S. Folgueras, I. Gonzalez Caballero, E. Palencia Cortezon, J.M. Vizan Garcia

Instituto de Física de Cantabria (IFCA), CSIC-Universidad de Cantabria, Santander, Spain

I.J. Cabrillo, A. Calderon, J.R. Castiñeiras De Saa, P. De Castro Manzano, J. Duarte Campderros, M. Fernandez, J. Garcia-Ferrero, G. Gomez, A. Lopez Virto, J. Marco, R. Marco, C. Martinez Rivero, F. Matorras, F.J. Munoz Sanchez, J. Piedra Gomez, T. Rodrigo, A.Y. Rodríguez-Marrero, A. Ruiz-Jimeno, L. Scodellaro, N. Trevisani, I. Vila, R. Vilar Cortabitarte

CERN, European Organization for Nuclear Research, Geneva, Switzerland

D. Abbaneo, E. Auffray, G. Auzinger, M. Bachtis, P. Baillon, A.H. Ball, D. Barney, A. Benaglia, J. Bendavid, L. Benhabib, J.F. Benitez, G.M. Berruti, P. Bloch, A. Bocci, A. Bonato, C. Botta, H. Breuker, T. Camporesi, R. Castello, G. Cerminara, M. D'Alfonso, D. d'Enterria, A. Dabrowski, V. Daponte, A. David, M. De Gruttola, F. De Guio, A. De Roeck, S. De Visscher, E. Di Marco, M. Dobson, M. Dordevic, B. Dorney, T. du Pree, M. Dünser, N. Dupont, A. Elliott-Peisert, G. Franzoni, W. Funk, D. Gigi, K. Gill, D. Giordano, M. Girone, F. Glege, R. Guida, S. Gundacker, M. Guthoff, J. Hammer, P. Harris, J. Hegeman, V. Innocente, P. Janot, H. Kirschenmann, M.J. Kortelainen, K. Kousouris, K. Krajczar, P. Lecoq, C. Lourenço, M.T. Lucchini, N. Magini, L. Malgeri, M. Mannelli, A. Martelli, L. Masetti, F. Meijers, S. Mersi, E. Meschi, F. Moortgat, S. Morovic, M. Mulders, M.V. Nemallapudi, H. Neugebauer, S. Orfanelli[44], L. Orsini, L. Pape, E. Perez, M. Peruzzi, A. Petrilli, G. Petrucciani, A. Pfeiffer, D. Piparo, A. Racz, G. Rolandi[45], M. Rovere, M. Ruan, H. Sakulin, C. Schäfer, C. Schwick, A. Sharma, P. Silva, M. Simon, P. Sphicas[46], J. Steggemann, B. Stieger, M. Stoye, Y. Takahashi, D. Treille, A. Triossi, A. Tsirou, G.I. Veres[21], N. Wardle, H.K. Wöhri, A. Zagozdzinska[37], W.D. Zeuner

Paul Scherrer Institut, Villigen, Switzerland

W. Bertl, K. Deiters, W. Erdmann, R. Horisberger, Q. Ingram, H.C. Kaestli, D. Kotlinski, U. Langenegger, D. Renker, T. Rohe

Institute for Particle Physics, ETH Zurich, Zurich, Switzerland

F. Bachmair, L. Bäni, L. Bianchini, B. Casal, G. Dissertori, M. Dittmar, M. Donegà, P. Eller, C. Grab, C. Heidegger, D. Hits, J. Hoss, G. Kasieczka, W. Lustermann, B. Mangano, M. Marionneau, P. Martinez Ruiz del Arbol, M. Masciovecchio, D. Meister, F. Micheli, P. Musella, F. Nessi-Tedaldi, F. Pandolfi, J. Pata, F. Pauss, L. Perrozzi, M. Quittnat, M. Rossini, A. Starodumov[47], M. Takahashi, V.R. Tavolaro, K. Theofilatos, R. Wallny

Universität Zürich, Zurich, Switzerland

T.K. Aarrestad, C. Amsler[48], L. Caminada, M.F. Canelli, V. Chiochia, A. De Cosa, C. Galloni, A. Hinzmann, T. Hreus, B. Kilminster, C. Lange, J. Ngadiuba, D. Pinna, P. Robmann, F.J. Ronga, D. Salerno, Y. Yang

National Central University, Chung-Li, Taiwan

M. Cardaci, K.H. Chen, T.H. Doan, Sh. Jain, R. Khurana, M. Konyushikhin, C.M. Kuo, W. Lin, Y.J. Lu, S.S. Yu

2017 JINST 12 P02014

National Taiwan University (NTU), Taipei, Taiwan
Arun Kumar, R. Bartek, P. Chang, Y.H. Chang, Y.W. Chang, Y. Chao, K.F. Chen, P.H. Chen, C. Dietz, F. Fiori, U. Grundler, W.-S. Hou, Y. Hsiung, Y.F. Liu, R.-S. Lu, M. Miñano Moya, E. Petrakou, J.f. Tsai, Y.M. Tzeng

Chulalongkorn University, Faculty of Science, Department of Physics, Bangkok, Thailand
B. Asavapibhop, K. Kovitanggoon, G. Singh, N. Srimanobhas, N. Suwonjandee

Cukurova University, Adana, Turkey
A. Adiguzel, S. Cerci[49], Z.S. Demiroglu, C. Dozen, I. Dumanoglu, S. Girgis, G. Gokbulut, Y. Guler, E. Gurpinar, I. Hos, E.E. Kangal[50], A. Kayis Topaksu, G. Onengut[51], K. Ozdemir[52], S. Ozturk[53], B. Tali[49], H. Topakli[53], M. Vergili, C. Zorbilmez

Middle East Technical University, Physics Department, Ankara, Turkey
I.V. Akin, B. Bilin, S. Bilmis, B. Isildak[54], G. Karapinar[55], M. Yalvac, M. Zeyrek

Bogazici University, Istanbul, Turkey
E.A. Albayrak[56], E. Gülmez, M. Kaya[57], O. Kaya[58], T. Yetkin[59]

Istanbul Technical University, Istanbul, Turkey
K. Cankocak, S. Sen[60], F.I. Vardarlı

Institute for Scintillation Materials of National Academy of Science of Ukraine, Kharkov, Ukraine
B. Grynyov

National Scientific Center, Kharkov Institute of Physics and Technology, Kharkov, Ukraine
L. Levchuk, P. Sorokin

University of Bristol, Bristol, United Kingdom
R. Aggleton, F. Ball, L. Beck, J.J. Brooke, E. Clement, D. Cussans, H. Flacher, J. Goldstein, M. Grimes, G.P. Heath, H.F. Heath, J. Jacob, L. Kreczko, C. Lucas, Z. Meng, D.M. Newbold[61], S. Paramesvaran, A. Poll, T. Sakuma, S. Seif El Nasr-storey, S. Senkin, D. Smith, V.J. Smith

Rutherford Appleton Laboratory, Didcot, United Kingdom
K.W. Bell, A. Belyaev[62], C. Brew, R.M. Brown, D. Cieri, D.J.A. Cockerill, J.A. Coughlan, K. Harder, S. Harper, E. Olaiya, D. Petyt, C.H. Shepherd-Themistocleous, A. Thea, I.R. Tomalin, T. Williams, W.J. Womersley, S.D. Worm

Imperial College, London, United Kingdom
M. Baber, R. Bainbridge, O. Buchmuller, A. Bundock, D. Burton, S. Casasso, M. Citron, D. Colling, L. Corpe, N. Cripps, P. Dauncey, G. Davies, A. De Wit, M. Della Negra, P. Dunne, A. Elwood, W. Ferguson, J. Fulcher, D. Futyan, G. Hall, G. Iles, M. Kenzie, R. Lane, R. Lucas[61], L. Lyons, A.-M. Magnan, S. Malik, J. Nash, A. Nikitenko[47], J. Pela, M. Pesaresi, K. Petridis, D.M. Raymond, A. Richards, A. Rose, C. Seez, A. Tapper, K. Uchida, M. Vazquez Acosta[63], T. Virdee, S.C. Zenz

Brunel University, Uxbridge, United Kingdom
J.E. Cole, P.R. Hobson, A. Khan, P. Kyberd, D. Leggat, D. Leslie, I.D. Reid, P. Symonds, L. Teodorescu, M. Turner

2017 JINST 12 P02014

Baylor University, Waco, U.S.A.

A. Borzou, K. Call, J. Dittmann, K. Hatakeyama, A. Kasmi, H. Liu, N. Pastika

The University of Alabama, Tuscaloosa, U.S.A.

O. Charaf, S.I. Cooper, C. Henderson, P. Rumerio

Boston University, Boston, U.S.A.

A. Avetisyan, T. Bose, C. Fantasia, D. Gastler, P. Lawson, D. Rankin, C. Richardson, J. Rohlf, J. St. John, L. Sulak, D. Zou

Brown University, Providence, U.S.A.

J. Alimena, E. Berry, S. Bhattacharya, D. Cutts, N. Dhingra, A. Ferapontov, A. Garabedian, J. Hakala, U. Heintz, E. Laird, G. Landsberg, Z. Mao, M. Narain, S. Piperov, S. Sagir, T. Sinthuprasith, R. Syarif

University of California, Davis, Davis, U.S.A.

R. Breedon, G. Breto, M. Calderon De La Barca Sanchez, S. Chauhan, M. Chertok, J. Conway, R. Conway, P.T. Cox, R. Erbacher, M. Gardner, W. Ko, R. Lander, M. Mulhearn, D. Pellett, J. Pilot, F. Ricci-Tam, S. Shalhout, J. Smith, M. Squires, D. Stolp, M. Tripathi, S. Wilbur, R. Yohay

University of California, Los Angeles, U.S.A.

R. Cousins, P. Everaerts, C. Farrell, J. Hauser, M. Ignatenko, D. Saltzberg, E. Takasugi, V. Valuev, M. Weber

University of California, Riverside, Riverside, U.S.A.

K. Burt, R. Clare, J. Ellison, J.W. Gary, G. Hanson, J. Heilman, M. Ivova PANEVA, P. Jandir, E. Kennedy, F. Lacroix, O.R. Long, A. Luthra, M. Malberti, M. Olmedo Negrete, A. Shrinivas, H. Wei, S. Wimpenny, B. R. Yates

University of California, San Diego, La Jolla, U.S.A.

J.G. Branson, G.B. Cerati, S. Cittolin, R.T. D'Agnolo, A. Holzner, R. Kelley, D. Klein, J. Letts, I. Macneill, D. Olivito, S. Padhi, M. Pieri, M. Sani, V. Sharma, S. Simon, M. Tadel, A. Vartak, S. Wasserbaech[64], C. Welke, F. Würthwein, A. Yagil, G. Zevi Della Porta

University of California, Santa Barbara, Santa Barbara, U.S.A.

D. Barge, J. Bradmiller-Feld, C. Campagnari, A. Dishaw, V. Dutta, K. Flowers, M. Franco Sevilla, P. Geffert, C. George, F. Golf, L. Gouskos, J. Gran, J. Incandela, C. Justus, N. Mccoll, S.D. Mullin, J. Richman, D. Stuart, I. Suarez, W. To, C. West, J. Yoo

California Institute of Technology, Pasadena, U.S.A.

D. Anderson, A. Apresyan, A. Bornheim, J. Bunn, Y. Chen, J. Duarte, A. Mott, H.B. Newman, C. Pena, M. Pierini, M. Spiropulu, J.R. Vlimant, S. Xie, R.Y. Zhu

Carnegie Mellon University, Pittsburgh, U.S.A.

M.B. Andrews, V. Azzolini, A. Calamba, B. Carlson, T. Ferguson, M. Paulini, J. Russ, M. Sun, H. Vogel, I. Vorobiev

2017 JINST 12 P02014

University of Colorado Boulder, Boulder, U.S.A.

J.P. Cumalat, W.T. Ford, A. Gaz, F. Jensen, A. Johnson, M. Krohn, T. Mulholland, U. Nauenberg, K. Stenson, S.R. Wagner

Cornell University, Ithaca, U.S.A.

J. Alexander, A. Chatterjee, J. Chaves, J. Chu, S. Dittmer, N. Eggert, N. Mirman, G. Nicolas Kaufman, J.R. Patterson, A. Rinkevicius, A. Ryd, L. Skinnari, L. Soffi, W. Sun, S.M. Tan, W.D. Teo, J. Thom, J. Thompson, J. Tucker, Y. Weng, P. Wittich

Fermi National Accelerator Laboratory, Batavia, U.S.A.

S. Abdullin, M. Albrow, J. Anderson, G. Apollinari, S. Banerjee, L.A.T. Bauerdick, A. Beretvas, J. Berryhill, P.C. Bhat, G. Bolla, K. Burkett, J.N. Butler, H.W.K. Cheung, F. Chlebana, S. Cihangir, V.D. Elvira, I. Fisk, J. Freeman, E. Gottschalk, L. Gray, D. Green, S. Grünendahl, O. Gutsche, J. Hanlon, D. Hare, R.M. Harris, S. Hasegawa, J. Hirschauer, Z. Hu, S. Jindariani, M. Johnson, U. Joshi, A.W. Jung, B. Klima, B. Kreis, S. Kwan[†], S. Lammel, J. Linacre, D. Lincoln, R. Lipton, T. Liu, R. Lopes De Sá, J. Lykken, K. Maeshima, J.M. Marraffino, V.I. Martinez Outschoorn, S. Maruyama, D. Mason, P. McBride, P. Merkel, K. Mishra, S. Mrenna, S. Nahn, C. Newman-Holmes, V. O'Dell, K. Pedro, O. Prokofyev, G. Rakness, E. Sexton-Kennedy, A. Soha, W.J. Spalding, L. Spiegel, L. Taylor, S. Tkaczyk, N.V. Tran, L. Uplegger, E.W. Vaandering, C. Vernieri, M. Verzocchi, R. Vidal, H.A. Weber, A. Whitbeck, F. Yang

University of Florida, Gainesville, U.S.A.

D. Acosta, P. Avery, P. Bortignon, D. Bourilkov, A. Carnes, M. Carver, D. Curry, S. Das, G.P. Di Giovanni, R.D. Field, I.K. Furic, J. Hugon, J. Konigsberg, A. Korytov, J.F. Low, P. Ma, K. Matchev, H. Mei, P. Milenovic[65], G. Mitselmakher, D. Rank, R. Rossin, L. Shchutska, M. Snowball, D. Sperka, N. Terentyev, L. Thomas, J. Wang, S. Wang, J. Yelton

Florida International University, Miami, U.S.A.

S. Hewamanage, S. Linn, P. Markowitz, G. Martinez, J.L. Rodriguez

Florida State University, Tallahassee, U.S.A.

A. Ackert, J.R. Adams, T. Adams, A. Askew, J. Bochenek, B. Diamond, J. Haas, S. Hagopian, V. Hagopian, K.F. Johnson, A. Khatiwada, H. Prosper, M. Weinberg

Florida Institute of Technology, Melbourne, U.S.A.

M.M. Baarmand, V. Bhopatkar, S. Colafranceschi[66], M. Hohlmann, H. Kalakhety, D. Noonan, T. Roy, F. Yumiceva

University of Illinois at Chicago (UIC), Chicago, U.S.A.

M.R. Adams, L. Apanasevich, D. Berry, R.R. Betts, I. Bucinskaite, R. Cavanaugh, O. Evdokimov, L. Gauthier, C.E. Gerber, D.J. Hofman, P. Kurt, C. O'Brien, I.D. Sandoval Gonzalez, C. Silkworth, P. Turner, N. Varelas, Z. Wu, M. Zakaria

The University of Iowa, Iowa City, U.S.A.

B. Bilki[67], W. Clarida, K. Dilsiz, S. Durgut, R.P. Gandrajula, M. Haytmyradov, V. Khristenko, J.-P. Merlo, H. Mermerkaya[68], A. Mestvirishvili, A. Moeller, J. Nachtman, H. Ogul, Y. Onel, F. Ozok[56], A. Penzo, C. Snyder, P. Tan, E. Tiras, J. Wetzel, K. Yi

2017 JINST 12 P02014

Johns Hopkins University, Baltimore, U.S.A.

I. Anderson, B.A. Barnett, B. Blumenfeld, N. Eminizer, D. Fehling, L. Feng, A.V. Gritsan, P. Maksimovic, C. Martin, M. Osherson, J. Roskes, A. Sady, U. Sarica, M. Swartz, M. Xiao, Y. Xin, C. You

The University of Kansas, Lawrence, U.S.A.

P. Baringer, A. Bean, G. Benelli, C. Bruner, R.P. Kenny III, D. Majumder, M. Malek, M. Murray, S. Sanders, R. Stringer, Q. Wang

Kansas State University, Manhattan, U.S.A.

A. Ivanov, K. Kaadze, S. Khalil, M. Makouski, Y. Maravin, A. Mohammadi, L.K. Saini, N. Skhirtladze, S. Toda

Lawrence Livermore National Laboratory, Livermore, U.S.A.

D. Lange, F. Rebassoo, D. Wright

University of Maryland, College Park, U.S.A.

C. Anelli, A. Baden, O. Baron, A. Belloni, B. Calvert, S.C. Eno, C. Ferraioli, J.A. Gomez, N.J. Hadley, S. Jabeen, R.G. Kellogg, T. Kolberg, J. Kunkle, Y. Lu, A.C. Mignerey, Y.H. Shin, A. Skuja, M.B. Tonjes, S.C. Tonwar

Massachusetts Institute of Technology, Cambridge, U.S.A.

A. Apyan, R. Barbieri, A. Baty, K. Bierwagen, S. Brandt, W. Busza, I.A. Cali, Z. Demiragli, L. Di Matteo, G. Gomez Ceballos, M. Goncharov, D. Gulhan, Y. Iiyama, G.M. Innocenti, M. Klute, D. Kovalskyi, Y.S. Lai, Y.-J. Lee, A. Levin, P.D. Luckey, A.C. Marini, C. Mcginn, C. Mironov, X. Niu, C. Paus, D. Ralph, C. Roland, G. Roland, J. Salfeld-Nebgen, G.S.F. Stephans, K. Sumorok, M. Varma, D. Velicanu, J. Veverka, J. Wang, T.W. Wang, B. Wyslouch, M. Yang, V. Zhukova

University of Minnesota, Minneapolis, U.S.A.

B. Dahmes, A. Evans, A. Finkel, A. Gude, P. Hansen, S. Kalafut, S.C. Kao, K. Klapoetke, Y. Kubota, Z. Lesko, J. Mans, S. Nourbakhsh, N. Ruckstuhl, R. Rusack, N. Tambe, J. Turkewitz

University of Mississippi, Oxford, U.S.A.

J.G. Acosta, S. Oliveros

University of Nebraska-Lincoln, Lincoln, U.S.A.

E. Avdeeva, K. Bloom, S. Bose, D.R. Claes, A. Dominguez, C. Fangmeier, R. Gonzalez Suarez, R. Kamalieddin, J. Keller, D. Knowlton, I. Kravchenko, J. Lazo-Flores, F. Meier, J. Monroy, F. Ratnikov, J.E. Siado, G.R. Snow

State University of New York at Buffalo, Buffalo, U.S.A.

M. Alyari, J. Dolen, J. George, A. Godshalk, C. Harrington, I. Iashvili, J. Kaisen, A. Kharchilava, A. Kumar, S. Rappoccio, B. Roozbahani

Northeastern University, Boston, U.S.A.

G. Alverson, E. Barberis, D. Baumgartel, M. Chasco, A. Hortiangtham, A. Massironi, D.M. Morse, D. Nash, T. Orimoto, R. Teixeira De Lima, D. Trocino, R.-J. Wang, D. Wood, J. Zhang

2017 JINST 12 P02014

Northwestern University, Evanston, U.S.A.

K.A. Hahn, A. Kubik, N. Mucia, N. Odell, B. Pollack, A. Pozdnyakov, M. Schmitt, S. Stoynev, K. Sung, M. Trovato, M. Velasco

University of Notre Dame, Notre Dame, U.S.A.

A. Brinkerhoff, N. Dev, M. Hildreth, C. Jessop, D.J. Karmgard, N. Kellams, K. Lannon, S. Lynch, N. Marinelli, F. Meng, C. Mueller, Y. Musienko[38], T. Pearson, M. Planer, A. Reinsvold, R. Ruchti, G. Smith, S. Taroni, N. Valls, M. Wayne, M. Wolf, A. Woodard

The Ohio State University, Columbus, U.S.A.

L. Antonelli, J. Brinson, B. Bylsma, L.S. Durkin, S. Flowers, A. Hart, C. Hill, R. Hughes, W. Ji, K. Kotov, T.Y. Ling, B. Liu, W. Luo, D. Puigh, M. Rodenburg, B.L. Winer, H.W. Wulsin

Princeton University, Princeton, U.S.A.

O. Driga, P. Elmer, J. Hardenbrook, P. Hebda, S.A. Koay, P. Lujan, D. Marlow, T. Medvedeva, M. Mooney, J. Olsen, C. Palmer, P. Piroué, X. Quan, H. Saka, D. Stickland, C. Tully, J.S. Werner, A. Zuranski

University of Puerto Rico, Mayaguez, U.S.A.

S. Malik

Purdue University, West Lafayette, U.S.A.

V.E. Barnes, D. Benedetti, D. Bortoletto, L. Gutay, M.K. Jha, M. Jones, K. Jung, D.H. Miller, N. Neumeister, B.C. Radburn-Smith, X. Shi, I. Shipsey, D. Silvers, J. Sun, A. Svyatkovskiy, F. Wang, W. Xie, L. Xu

Purdue University Calumet, Hammond, U.S.A.

N. Parashar, J. Stupak

Rice University, Houston, U.S.A.

A. Adair, B. Akgun, Z. Chen, K.M. Ecklund, F.J.M. Geurts, M. Guilbaud, W. Li, B. Michlin, M. Northup, B.P. Padley, R. Redjimi, J. Roberts, J. Rorie, Z. Tu, J. Zabel

University of Rochester, Rochester, U.S.A.

B. Betchart, A. Bodek, P. de Barbaro, R. Demina, Y. Eshaq, T. Ferbel, M. Galanti, A. Garcia-Bellido, J. Han, A. Harel, O. Hindrichs, A. Khukhunaishvili, G. Petrillo, M. Verzetti

Rutgers, The State University of New Jersey, Piscataway, U.S.A.

S. Arora, A. Barker, J.P. Chou, C. Contreras-Campana, E. Contreras-Campana, D. Duggan, D. Ferencek, Y. Gershtein, R. Gray, E. Halkiadakis, D. Hidas, E. Hughes, S. Kaplan, R. Kunnawalkam Elayavalli, A. Lath, K. Nash, S. Panwalkar, M. Park, S. Salur, S. Schnetzer, D. Sheffield, S. Somalwar, R. Stone, S. Thomas, P. Thomassen, M. Walker

University of Tennessee, Knoxville, U.S.A.

M. Foerster, G. Riley, K. Rose, S. Spanier, A. York

2017 JINST 12 P02014

Texas A&M University, College Station, U.S.A.

O. Bouhali[69], A. Castaneda Hernandez[69], M. Dalchenko, M. De Mattia, A. Delgado, S. Dildick, R. Eusebi, J. Gilmore, T. Kamon[70], V. Krutelyov, R. Mueller, I. Osipenkov, Y. Pakhotin, R. Patel, A. Perloff, A. Rose, A. Safonov, A. Tatarinov, K.A. Ulmer[2]

Texas Tech University, Lubbock, U.S.A.

N. Akchurin, C. Cowden, J. Damgov, C. Dragoiu, P.R. Dudero, J. Faulkner, S. Kunori, K. Lamichhane, S.W. Lee, T. Libeiro, S. Undleeb, I. Volobouev

Vanderbilt University, Nashville, U.S.A.

E. Appelt, A.G. Delannoy, S. Greene, A. Gurrola, R. Janjam, W. Johns, C. Maguire, Y. Mao, A. Melo, H. Ni, P. Sheldon, B. Snook, S. Tuo, J. Velkovska, Q. Xu

University of Virginia, Charlottesville, U.S.A.

M.W. Arenton, B. Cox, B. Francis, J. Goodell, R. Hirosky, A. Ledovskoy, H. Li, C. Lin, C. Neu, X. Sun, Y. Wang, E. Wolfe, J. Wood, F. Xia

Wayne State University, Detroit, U.S.A.

C. Clarke, R. Harr, P.E. Karchin, C. Kottachchi Kankanamge Don, P. Lamichhane, J. Sturdy

University of Wisconsin - Madison, Madison, WI, U.S.A.

D.A. Belknap, D. Carlsmith, M. Cepeda, S. Dasu, L. Dodd, S. Duric, E. Friis, B. Gomber, M. Grothe, R. Hall-Wilton, M. Herndon, A. Hervé, P. Klabbers, A. Lanaro, A. Levine, K. Long, R. Loveless, A. Mohapatra, I. Ojalvo, T. Perry, G.A. Pierro, G. Polese, T. Ruggles, T. Sarangi, A. Savin, A. Sharma, N. Smith, W.H. Smith, D. Taylor, N. Woods

†: Deceased
1: Also at Vienna University of Technology, Vienna, Austria
2: Also at CERN, European Organization for Nuclear Research, Geneva, Switzerland
3: Also at State Key Laboratory of Nuclear Physics and Technology, Peking University, Beijing, China
4: Also at Institut Pluridisciplinaire Hubert Curien, Université de Strasbourg, Université de Haute Alsace Mulhouse, CNRS/IN2P3, Strasbourg, France
5: Also at National Institute of Chemical Physics and Biophysics, Tallinn, Estonia
6: Also at Skobeltsyn Institute of Nuclear Physics, Lomonosov Moscow State University, Moscow, Russia
7: Also at Universidade Estadual de Campinas, Campinas, Brazil
8: Also at Centre National de la Recherche Scientifique (CNRS) - IN2P3, Paris, France
9: Also at Laboratoire Leprince-Ringuet, Ecole Polytechnique, IN2P3-CNRS, Palaiseau, France
10: Also at Joint Institute for Nuclear Research, Dubna, Russia
11: Now at Suez University, Suez, Egypt
12: Now at British University in Egypt, Cairo, Egypt
13: Also at Cairo University, Cairo, Egypt
14: Also at Fayoum University, El-Fayoum, Egypt
15: Also at Université de Haute Alsace, Mulhouse, France
16: Also at Tbilisi State University, Tbilisi, Georgia
17: Also at RWTH Aachen University, III. Physikalisches Institut A, Aachen, Germany
18: Also at University of Hamburg, Hamburg, Germany
19: Also at Brandenburg University of Technology, Cottbus, Germany

2017 JINST 12 P02014

20: Also at Institute of Nuclear Research ATOMKI, Debrecen, Hungary
21: Also at Eötvös Loránd University, Budapest, Hungary
22: Also at University of Debrecen, Debrecen, Hungary
23: Also at Wigner Research Centre for Physics, Budapest, Hungary
24: Also at University of Visva-Bharati, Santiniketan, India
25: Now at King Abdulaziz University, Jeddah, Saudi Arabia
26: Also at University of Ruhuna, Matara, Sri Lanka
27: Also at Isfahan University of Technology, Isfahan, Iran
28: Also at University of Tehran, Department of Engineering Science, Tehran, Iran
29: Also at Plasma Physics Research Center, Science and Research Branch, Islamic Azad University, Tehran, Iran
30: Also at Laboratori Nazionali di Legnaro dell'INFN, Legnaro, Italy
31: Also at Università degli Studi di Siena, Siena, Italy
32: Also at Purdue University, West Lafayette, U.S.A.
33: Now at Hanyang University, Seoul, Korea
34: Also at International Islamic University of Malaysia, Kuala Lumpur, Malaysia
35: Also at Malaysian Nuclear Agency, MOSTI, Kajang, Malaysia
36: Also at Consejo Nacional de Ciencia y Tecnología, Mexico city, Mexico
37: Also at Warsaw University of Technology, Institute of Electronic Systems, Warsaw, Poland
38: Also at Institute for Nuclear Research, Moscow, Russia
39: Also at St. Petersburg State Polytechnical University, St. Petersburg, Russia
40: Also at National Research Nuclear University 'Moscow Engineering Physics Institute' (MEPhI), Moscow, Russia
41: Also at California Institute of Technology, Pasadena, U.S.A.
42: Also at INFN Sezione di Padova; Università di Padova; Università di Trento (Trento), Padova, Italy
43: Also at Faculty of Physics, University of Belgrade, Belgrade, Serbia
44: Also at National Technical University of Athens, Athens, Greece
45: Also at Scuola Normale e Sezione dell'INFN, Pisa, Italy
46: Also at National and Kapodistrian University of Athens, Athens, Greece
47: Also at Institute for Theoretical and Experimental Physics, Moscow, Russia
48: Also at Albert Einstein Center for Fundamental Physics, Bern, Switzerland
49: Also at Adiyaman University, Adiyaman, Turkey
50: Also at Mersin University, Mersin, Turkey
51: Also at Cag University, Mersin, Turkey
52: Also at Piri Reis University, Istanbul, Turkey
53: Also at Gaziosmanpasa University, Tokat, Turkey
54: Also at Ozyegin University, Istanbul, Turkey
55: Also at Izmir Institute of Technology, Izmir, Turkey
56: Also at Mimar Sinan University, Istanbul, Istanbul, Turkey
57: Also at Marmara University, Istanbul, Turkey
58: Also at Kafkas University, Kars, Turkey
59: Also at Yildiz Technical University, Istanbul, Turkey
60: Also at Hacettepe University, Ankara, Turkey
61: Also at Rutherford Appleton Laboratory, Didcot, United Kingdom
62: Also at School of Physics and Astronomy, University of Southampton, Southampton, United Kingdom
63: Also at Instituto de Astrofísica de Canarias, La Laguna, Spain
64: Also at Utah Valley University, Orem, U.S.A.
65: Also at University of Belgrade, Faculty of Physics and Vinca Institute of Nuclear Sciences, Belgrade, Serbia

2017 JINST 12 P02014

66: Also at Facoltà Ingegneria, Università di Roma, Roma, Italy
67: Also at Argonne National Laboratory, Argonne, U.S.A.
68: Also at Erzincan University, Erzincan, Turkey
69: Also at Texas A&M University at Qatar, Doha, Qatar
70: Also at Kyungpook National University, Daegu, Korea

2017 JINST 12 P02014